UNIVERSITA' DEGLI STUDI DI PARMA

Dottorato di ricerca in Fisica

Ciclo XXVIII

Magnetic properties and Spin dynamics in magnetic Molecular Rings

Coordinatore:
Chiar.mo Prof. Cristiano Viappiani

Tutor:
Chiar.mo Prof. Giuseppe Allodi

Dottorando: Sara Bordignon

Dottorato di Ricerca in Fisica

XXVIII CICLO

MAGNETIC PROPERTIES AND SPIN DYNAMICS IN MOLECULAR RINGS

Coordinator: Prof. Cristiano Viappiani

Tutor: Prof. Giuseppe Allodi
Co-tutor: Prof. Stefano Carretta

Dottoranda: Sara Bordignon

Commission of the final examination:

External Member: Prof. M. Affronte
Prof. J. van Slageren

Internal Member: Prof. M.Riccò

AUTHOR'S ADDRESS

Sara Bordignon

Dipartimento di Fisica e Scienze della Terra

Università degli Studi di Parma

Parco Area delle Scienze, via G.P. Usberti 7/A

I-43124 Parma, Italy.

E-mail: *sara.bordignon@fis.unipr.it*

"...One Ring to rule them all, one Ring to find them, One Ring to bring them all and in the darkness bind them.."

Contents

Chapter 1

Introduction

All the work that will be shown has been done within the framework of the FIRB Project: "New challenges in molecular nanomagnetism: from spin dynamics to quantum information processing". The present thesis has been mostly devoted to the experimental investigation of the magnetic properties and spin dynamics of different classes of antiferromagnetic (AF) molecular rings. The aim of this work is to shed more light on the quantum behavior and the potential applications in future technologies of these molecular rings. One of the most important goals is to reach a deep understanding of the relaxation dynamics of molecular nanomagnets (MNMs), because this aspect is of paramount importance in the design of new molecules acting as classical or quantum bits. In the present study we have exploited various techniques of investigations, such as Nuclear Magnetic Resonance (NMR), muon spin relaxation (μSR) and SQUiD magnetometry. Through these techniques, the static and dynamic properties of these systems have been studied. The interpretation of the experimental results has been tackled by the Group of Molecular Nanomagnetism of Proff. P. Santini, S. Carretta and G.Amoretti at the Department of Physics and Earth Science of the University of Parma.
The core of this thesis is divided in five main chapters. The first one is an introduction on MNMs and the second chapter gives an overview of the techniques adopted for the experimental study. The third chapter is devoted to the presentation of the results and to the discussion on the first regular closed ring with an odd number of magnetic ions, Cr_9. Chapter four presents results on the direct

observation of finite size effects in AF chains. Finally, chapter 5 is devoted to the study of the six-membered Dy_6 ring. The last section is dedicated to the general conclusions.

Main results of this Thesis

- Magnetic properties and relaxation dynamics of the first regular Cr_9 AF ring have been investigated. This molecule represents a prototype of practically degenerate-frustrated homometallic ring of half-integer spins. The relaxation of Cr_9 has been investigated by measuring the temperature and magnetic field dependence of the spin-lattice relaxation rate $1/T_1$ of ^1H nuclei. The comparison between the experimental ^1H-NMR results and theory validates a model including spin-phonon magnetoelastic couplings and taking into account the wipeout effect. The relaxation dynamics of this molecule is characterized by a single Arrhenius time only at very low temperatures, whereas above 3 K several relevant relaxation rates emerge. This is the first investigation of the relaxation dynamics of an odd-membered AF ring.

- The Cr_8Cd AF rings are model systems for the study of the microscopic magnetic behaviour of finite AF Heisenberg chains. In this type of system the different magnetic behaviour depends the length and on the parity of the chain (odd or even). In order to study the local spin densities on the Cr sites, the ^{53}Cr-NMR spectra were collected at low temperature. The major difficulty in the ^{53}Cr-NMR measurements is due to the low natural abundance and the low sensitivity of the probe. The experimental results confirm the theoretical predictions for the non-collinear spin arrangement. It was also possible to identify from which pair of Cr the observed signal came from.

- The study of the magnetic properties and relaxation dynamics of the first rare-earth based ring are reported. The behaviour of AC susceptibility data has been interpreted with the simplest conceivable model, assuming two different relaxation processes in the phonon-induced relaxation dynamics of the molecule. A μSR LF-experiments as a function of the temperature have

been carried out on the GPS spectrometer at the continuous muon source of the SμS facility of the Paul Scherrer Institute (PSI). The temperature dependent Longitudinal relaxation rate (λ) was fitted by a distribution of energy barriers. The results of the fit yield an average activation energy barrier around 250 K, compatible with the energy difference between the Kramers doublet ground state and the first excited doublet.

1.1 Molecular Nanomagnets

Molecular nanomagnets are spin clusters whose topology and magnetic interactions can be modulated at the level of the chemical synthesis. They are typically formed by a small number of transition metal ions coupled by the Heisenberg's exchange interactions. Each cluster is magnetically isolated from its neighbors by organic ligands, making each unit not interacting with the others. Therefore, we can investigate the magnetic properties of an isolated molecular nanomagnet by bulk measurements. The scientific interest on low-dimensional magnetic systems has grown significantly during the last decades [1, 2]. In particular, magnetic molecules have become a very attractive model system for the study of fondamental magnetic phenomena, such as the quantum tunneling of magnetization [3], the level crossing and the microscopic magnetic interactions. From the applicative point of view, molecular magnets are considered promising candidates in the field of the high-density information storage, quantum computation and quantum information processing [4, 5, 6, 2, 7], and for low temperature magnetic refrigeration [1].

It is worth to pointing out that the synthesis of these systems is not trivial. The design of ring-shaped structures made of magnetic ions is carried out via several complex chemical routes, through the appropriate selection of the correct organic ligands.

The size of these systems is nanometric and this reflects on their dynamics and magnetic behavior, leading to a characteristic magnetic behavior and spin dynamics. The figure 1.1.1 schematically shows the size effects of the magnetization dynamics and the hysteresis loops, from multidomain magnetic particles to molecular clusters [1].

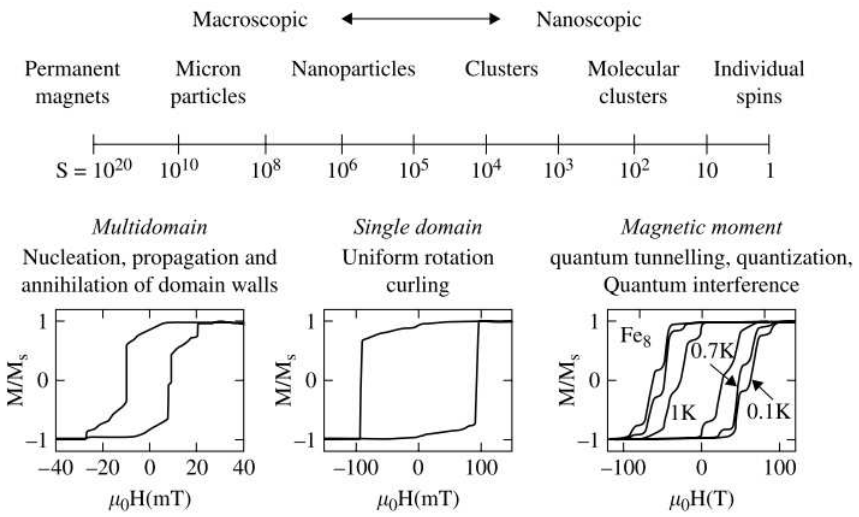

Figure 1.1.1: Hysteresis loops are typical examples of magnetization reversal via nucleation, propagation, and annihilation of domain walls (left), via uniform rotation (middle), and quantum tunnelling (right)[1].

From the physical point of view, it is common to refer to these molecules with simplified formulas, highlighting the constituting metals and omitting the organic ligands, the latter being important from a chemical point of view. The first ever identified molecular magnets have been the Fe_8 and the Mn_{12}. These clusters are characterized by a high-spin ground state and an uniaxial magnetic anisotropy, which creates an energy barrier for the reorientation of the magnetization. Sangregorio *et al.* have shown that the characteristic time of relaxation of Fe_8 becomes temperature independent below T = 0.36 K, proving that the relaxation of the magnetization is due to the quantum tunneling across the anisotropy barrier [8]. The jumps in the hysteresis cycles of Fe_8 (Figure1.1.1, graph on the right) for specific values of the applied magnetic field correspond to the anti-crossing fields, involving states from different sides of the energy barrier. Takashi et al. [9] show that the strong spin decoherence is significantly suppressed by polarizing the spin bath in Fe_8 single-molecule magnets.

In addition to single-molecule magnets there are different families of magnetic molecules, like the triangle-shaped Dy_3[10], the Mn [3x3] grid[11] and the antiferromagnetic rings [12]. In particular, the latters are the main subject of this thesis.

Homometallic Antiferromagnetic (AF) ring-shaped systems constitute an interesting subgroup of molecular nanomagnets, with a finite number of magnetic ions lying on an almost regular ring. Due to the finite-size effects, AF rings possess a discrete energy spectrum [12]. The energies of the lowest-lying excited states of each total spin S_T can be approximately given by the so-called Landé rule: $E(S_T) = \left(\frac{2J}{N}\right) S_T(S_T+1)$, where J is the antiferromagnetic exchange coupling constant and N is the number of magnetic ions composing the ring. The application of an external magnetic field lifts the magnetic degeneracy of each state, resulting in successive ground-state level crossings.
AF rings can be divided in different categories, depending on the number of magnetic ions within the ring: even or odd, being these open or closed. Open rings can be obtained by the subsitution of a magnetic ion with a dimagnetic one and it is possible to identify the system as a finite-size chain. Figure 1.1.2 shows the two different types of geometries. In particular, even-membered AF rings are characterized by a S=0 ground state (where S is the total spin of the molecule) and they can display the quantum tunneling of the Néel vector [13, 14], which is the AF counterpart of the magnetization tunneling. These systems have been also exploited to investigate the nature of the elementary excitations in finite AF systems [14, 15].

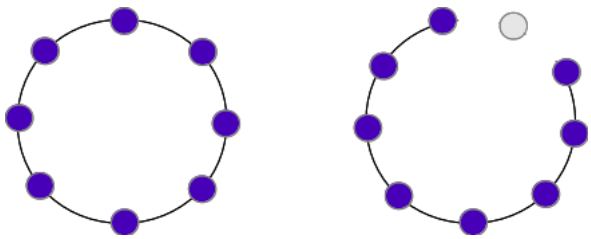

Figure 1.1.2: Even closed ring and Even open ring.

There are two main differences between an even closed and an even open ring:

1. *The excitation energy depends on the position*. In a closed ring, each spin is coupled to the two nearest-neighbors by the antiferromagnetic exchange parameters (J). In order to flip one of these spins an excitation energy equal to 2J is necessary. In the case of an open ring, the excitation energy depends

on the position of the spin: in case of an edges position, the required excitation energy is just J, being the spin coupled to only one spin at one side [16].

2. *The distribution of the spin moment*: In a closed ring we can expect a uniform distribution when a magnetic ground state is induced by applying a suitable field, since the excitation energy does not depend on the position of the spin. In the case of an open ring, the spins at the edge would be polarized more easily than the others, so we have a redistribution of spin moments with a staggered spin structure [17, 16].

The distribution of the magnetic moments also depends wether the chain is odd or even *e.g.* Cr_7Cd and Cr_8Cd [17, 18]. In literature there are already results about this and part of this thesis concerns these aspects (see chapter 4).

1.2 Technological Applications

As mentioned above, the interest in MNMs is double and it concerns both fundamental studies and technological applications. The envisaged technological applications include:

- Combining the advantages of the molecular scale with the properties of bulk magnetic materials, MNMs have been considered promising materials for the high-density information storage [4], due to their slow relaxation of the magnetization [8]. In Dy_6 (see chapter 5) the toroidal magnetic moment is a key property that can be useful in this field. In fact, the insensitivity to homogeneous magnetic fields [19], makes these systems more protected against the action of a external fields, respect to the spin projection eigenstates of a true spin S = 1/2.[20]. Moreover, qubits designed on this basis can be packed much more densely than spin qubits, because the magnetic field produced by a toroidal moment decays much faster than the field of a magnetic dipole.

- Molecular nanomagnets have been proposed as candidates to encode qubits [21, 22, 23, 24, 25, 26], the basic unit for quantum information process-

ing. In particular, the Cr_7Ni rings behave as effective spin-1/2 systems at low temperature and show rather long decoherence times. In addition these rings can be linked together in order to realize supramolecular clusters, whose coupling can be tuned by properly choosing the linker between the rings[27, 28, 21, 29, 26, 30, 31]. These supramolecular systems are envisaged candidtes for the implementations of two-qubit quantum gates.

- Recently a new scheme to perform quantum information processing, based on a hybrid spin-photon qubit encoding, has been proposed [32].

- MNMs can also be considered promising materials formolecular spintronics, thanks to their large axial anisotropy and their tunable magnetic features [33, 34, 35, 36].

- In some systems a large magnetocaloric effect is observed at low temperature, making MNMs promising materials for the magnetic refrigeration. [37, 38, 39, 40]

1.3 Theoretical Framework

Each molecular nanomagnet can be described by a microscopic Spin Hamiltonian (SH):

$$\mathscr{H} = \sum_{ij} J_{ij}\vec{s}_i \cdot \vec{s}_j + \sum_i \sum_{k,q} b_q^k(i) O_q^k(\vec{s}_i) + \sum_{ij} \vec{s}_i \cdot D_{ij} \cdot \vec{s}_j + \sum_{ij} G_{ij}\vec{s}_i \times \vec{s}_j + \mu_B \vec{B} \sum_i g\vec{s}_i \tag{1.3.1}$$

where the terms in sequence are: the isotropic Heisenberg exchange (the leading term); the local zero-field splitting terms, expressed by the with $O_q^k(\vec{s}_i)$ Stevens operator and the $b_q^k(i)$ CF parameters; the dipolar anisotropic exchange interactions; the antisymmetric exchange and the Zeeman term.The SH formalism is based on the assumption that each magnetic ion in the molecule can be represented by an effective spin s_i and it allows to express all the contributions to the energy of the system in terms of spin operators only [41]. In the case of d electrons we have $k = 2, 4$ [42]. All the terms in the SH can be rewritten in terms of Irreducible Tensor Operators, in order to that simplify the calculation of the Hamiltonian matrix elements on the total-spin basis. The parameters characterizing the different

contributions to the SH can be directly obtained from ab-initio calculations[43] or determined through the comparison with the experimental data.

Theoretical analysis of the relaxation dynamics

One of the most important aspects in the physics of magnetic molecules is the understanding and characterization of the relaxation mechanisms of molecular observables. It is important to understand these phenomena not only for fundamental reasons, but also from the point of view of the technological applications. In fact, decoherence and relaxation phenomena are the major obstacle to the development of technologies based on these systems [44, 4]. The decoherence of the time-evolution of the molecular observables, such as the molecule magnetization, is due to the interactions of the electronic spins with the other degrees of freedom, like nuclear spins or phonons, which often behave like an heat bath [45]. In particular, the dynamics of the AF rings are characterized by a relatively fast phonon-induced relaxation. For this reason, one of the best techniques to probe such dynamics is the nuclear magnetic resonance (NMR).
These irreversible relaxation dynamics can be theoretically investigated with the formalism of the rate (master) equations of the density matrix. More details can be found in reference [46]. The secular approximation allows to decouple the time evolution of the diagonal elements of the density matrix, $\rho_s(t) = \rho_{ss}(t)$, from that of the off-diagonal elements $\rho_{st}(t)$, with $s \neq t$. In a frequency-domain picture, this corresponds to a clear separation of the inelastic (IE) and the quasielastic (QE) spectral contributions. Only the latters are detected by NMR or AC-susceptibility. On these bases, the populations of the molecular eigenstates, evolve through the master equations:

$$\dot{p}_s(t) = \sum_t W_{st}\, p_t(t),$$

where W_{st} is the element of the rate matrix, which represents the probability per unit time that a transition between the eigenstates $|t\rangle$ and $|s\rangle$ is induced by the interaction with the heat bath [45]. The precise form of the rate matrix depends on the details of the spin-phonon interaction mechanism. Here, it is assumed

that each ion experiences a spherically symmetric magnetoelastic coupling, due to crystal fields modulations induced by phonons, which are described by a Debye model. The rate matrix can be calculated in the first-order perturbation theory:

$$W_{st} = \gamma^2 \pi^2 \Delta_{st}^3 n_{ph}(\Delta_{st}) \times \sum_{i,j=1}^{N} \sum_{q_1,q_2=x,y,z}^{N} \langle s| O_{q1,q2}(\mathbf{s}_i) |t\rangle \langle s| O_{q1,q2}(\mathbf{s}_j) |t\rangle^* \quad (1.3.2)$$

with $n(x) = \left(e^{\beta\hbar x} - 1\right)^{-1}$, $\Delta_{st} = \frac{(E_s - E_t)}{\hbar}$, the O_2^Q are quadrupolar operators. In this simplified spin-phonon model, γ is the unique free parameter and describes the spin-phonon coupling strength. γ will be estimated from the comparison with NMR or χ_{AC} experimental data [46].

The study of the dynamical correlation functions of the fluctuations of the molecular observables, such as the molecular magnetization (P=Q=M=$\sum_{i=1}^{n} \mathbf{s}_i$), allows to better understand the relaxation dynamics of MNMs. From a theoretical point of view, the Fourier transform of the correlation function can be expressed as a sum of Lorentzians:

$$S_{P,Q}(\omega, T, B) = \sum_{i=1}^{n} A(\lambda_i, T, B) \frac{\lambda_i(T,B)}{\lambda_i^2(T,B) + \omega^2}, \quad (1.3.3)$$

where $\lambda_i(T,B) = 1/\tau_{(QE)}^i$ are the eigenvalues of the rate matrix $\mathbf{W}$ and correspond to the characteristic rates of relaxation and $A(\lambda_i, T, B)$ are the frequency weights of the magnetization autocorrelation function. The sum of the weights is proportional to the product of the magnetic susceptibility and the temperature: $\sum_{i=1,n} A(\lambda_i, T, B) \propto \chi T$.

1.4 The investigated molecules

In the research area of molecular magnetism, the AF rings deserve a prominent place, as also demonstrated by the high number of publications on this subject (*e.g.* [16, 47, 48, 49, 50, 51]).

In Chapter 3 the study of the spin dynamics of the first regular example a Cr_9 molecule, an AF ring with an odd number of magnetic ions, (of $C_{90}H_{162}Cr_9F_9O_{36}$[52]),

is reported. Chapter 4 is devoted to the observation of the finite size effects in the open even chains. Here we analyze the ^{53}Cr-NMR spectra on the even-open ring Cr_8Cd [53] and compare them with the results obtained for the open odd membered ring, the Cr_7Cd . Chapter 5 is dedicated to the discussion of the magnetic properties and the spin dynamics of the first sythesized Rare Earth based ring, the Dy_6[54]. The ground state of the Dy_6 is characterized by a toroidal moment existing in the absence of a total magnetic moment [20]. The measurements presented in this thesis were made on powder samples in the case of Cr_9 and Dy_6, or on an oriented single crystals in the case of Cr_8Cd and Cr_8Zn. The molecular structures of the rings are displayed in figure 1.4.1.

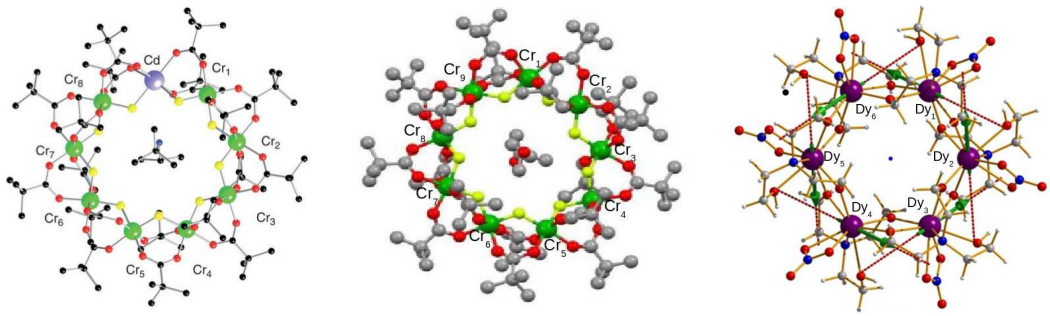

Formula	Abbreviation	Chapter
$C_{90}H_{162}Cr_9F_9O_{36}$	Cr_9	3
$[H_2NtBuisPr][Cr_8CdF_9(O_2CCMe_3)_{18}]$	Cr_8Cd	4
$[Dy(H_{tea})(NO_3)]_6 \cdot 8MeOH$	Dy_6	5

Figure 1.4.1: Starting from left to right: Cr_8Cd, Cr_9 and Dy_6 molecular ring. The figure Dy_6 is taken from the article of L.Ungur [20].

Chapter 2

Experimental Techniques

The experimental study of the magnetic properties of AF rings was performed by means of Nuclear Magnetic Resonance, SQuID magnetometry and Muon Spin Relaxation (μSR). In this chapter an overview of the techniques adopted and the informations they provide on the systems investigated will be presented. Figure 2.0.1shows the different time-window explored by several experimental techniques.

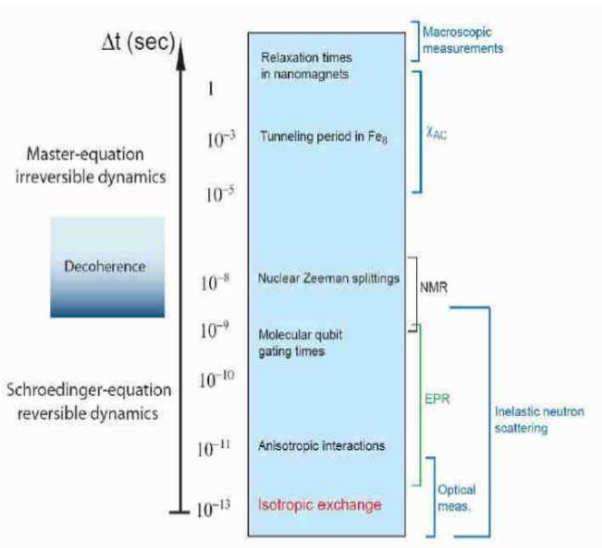

Figure 2.0.1: Time window of the different experimental techniques.

The dynamics of the AF rings are characterized by a relatively fast phonon-

induced relaxation, thus the best technique to probe such dynamics is the nuclear magnetic resonance (NMR). The selectivity of this technique allows the use of different nuclei as a probe, in addition to the standard measurements on the proton. For instance, the NMR spectra of ^{53}Cr have been collected to study the distribution of local local magnetic moments on the Cr_8Cd ring (see chapter 3). The aim of this chapter is to recall the basic aspects of Nuclear Magnetic Resonance, the muon spin resonance (μSR), and the SQuID Magnetometry.

2.1 Nuclear Magnetic Resonance (NMR)

The NMR spectroscopy is a powerful microscopic tool to investigate the electronic spin ensamble in both its static properties (the expectation values of the moments) and its dynamical ones (the spin fluctuations). The former are traced by the distribution of the static magnetic fields at the nucleus, i.e. the resonance spectrum, while the spin dynamics is probed by the relaxation of the nuclear magnetization, in particular, the spin-lattice relaxation. The classical principle underlying NMR is the Larmor precession of nuclear spins at a Larmor frequency $\omega_L = \gamma H_{loc}$, where H_{loc} is the local static field at the nuclues (the external field plus the internal one, due to the electron-nucleus interaction), and the gyromagnetic ratio γ is a constant of the nuclear species. Alternatively (and to most respects, equivalently),H_{loc} may be viewed as inducing an energy splitting $\Delta E = \hbar\omega_L$ between adjacent nuclear Zeeman levels $E_m = m\hbar\omega_L$. Typically, ω_L is in the radiofrequency (rf) range. If an alternate magnetic field oscillating at $\omega \approx \omega_L$ is also applied, it then gives rise to the resonant excitation of the nuclear Zeeman transitions, thanks to the $\Delta m \pm 1$ selection rule or, according to the classical description, to a coherent collective precession of the whole nuclear spin ensamble, Owing to the sensitivity enhancement inherent to a resonant method, the precession of a net nuclear moment is detectable despite its very small magnitude (as compared to the electronic one). The resonant character of the rf excitation is also related to the spectral selectivity of this technique. Spins excited off-resonance (other nuclear species and electronic moments), in fact, do not produce any measurable signal.
Several nuclei with spin $I \neq 0$ may be employed as nuclear probes. Among these, the nuclei of the magnetic ions are in principle the probe of choice, as they are

coupled to the on-site electronic moment by the hyperfine interaction (see below). Very often, however, such an on-site hyperfine coupling (ranging from tens tesla in transition metals to hundreds tesla in rare earths) is exceedingly large, leading to over-relaxed NMR signals and/or, in the case of rare earths, to resonance frequencies in the microwave range, hence outside the our experimental frequency band. Therefore all our measurements have been carried on the ligand protons, with the sole exception of ^{53}Cr NMR in Cr_8Cd which turned out to be a favourable case. ^1H is one the best nuclei in terms of sensitivity (100% naturally abundant and high γ) and it is coupled to the neighbouring ions by a weaker interaction, essentially dipolar in origin, which better fits into our experimental time window and frequency range. The drawback of protons is however their ihnomogeneous coupling, due to the presence of several inequivalent sites in the crystal with different distances from the ions. Such an inhomogeneity typically gives rise to non-exponential decay or recovey laws for the nuclear magnetization, due to distributions in the nuclear relaxation time constants T_1, T_2, which complicates the subsequent data analysis.

Bloch Equations and pulsed NMR

The time evolution of the nuclear spin ensamble is classically described by a set of phenomenological equations for the net nuclear magnetization, first proposed by F. Bloch. The Bloch equations for the free spin evolution (*i.e.* in the absence of a driving rf field) are written as

$$\begin{cases} \frac{dM_z}{dt} = \gamma(\bar{M} \times \bar{H}_0)_z + \frac{M_0 - M_z}{T_1} & (1) \\ \frac{dM_{x,y}}{dt} = \gamma(\bar{M} \times \bar{H}_0)_{x,y} + \frac{M_0 - M_{x,y}}{T_2} & (2) \end{cases} \tag{2.1.1}$$

The first terms on the right hand side corresponds to the coherent classical precession of the nuclear spins in the static field $\bar{H} = H_0\hat{z}$. The the other terms account for the irreversible processes (relaxations) by which the system recover thermodynamic equilibrium ($M_{x,y} = 0, M_z = M_0 = \chi_n H_0$, where χ_n is the nuclear susceptibility) and are introduced it *"ad hoc"*. The T_1 and T_2 phenomenological constants are, respectively, the spin-lattice (or longitudinal) and the spin-spin (or transverse)

relaxation time. The need for two distinct relaxation times is justified both experimentally and by physical arguments, as the two relaxation processes are in principle rather different. The longitudinal relaxation, involving a variation in the populations of the nuclear Zeeman levels, implies in fact energy exchanges with the thermal bath made by the surrounding electrons (the lattice). Such a thermal exchange, on the contrary, is not necessarily involved in the transverse relaxation, consisting in the dephasing of the precessing spins relative to each other (the microscopic theory of nuclear relaxations shows however that the relaxations of the populations also produce a so-called T_1-like term in the spin-spin relaxation: see below).

An applied rf field exciting the magnetic resonance can be accounted for, whithout genarality loss, in the form of a circularly polarized magnetic field $\bar{H}_1(t) = H_1(\cos\omega t\hat{x} + \sin\omega t\hat{y})$. When this rotating rf field is added to $\bar{H}_0$ in eq. 2.1.1, it gives rise to a set of coupled differential equations with time-dependent coefficients. However, such equations are transformed into time-independent ones by expressing $\bar{H}$ and $\bar{M}$ with respect to a reference frame rotating at a frequency ω, namely $\hat{x}' = \cos\omega t\hat{x} + \sin\omega t\hat{y}$, $\hat{y}' = -\sin\omega t\hat{x} + \cos\omega t\hat{y}$, $\hat{z}' = \hat{z}$ with respect to laboratory. With this transform, the time evolution of the nuclear spin ensamble, neglecting relaxations, is equivalent to the precession around a *static* effective field $\bar{H}_{eff} = H_1\hat{x}' + (H_0 - \omega/\gamma)\hat{z}$. The corresponding Bloch equations in the rotating frame, including relaxation phenomena, are then written as

$$\begin{cases} \frac{dM_x}{dt} = (\gamma H_0 - \omega)M_y - \frac{M_x}{T_2} & (1b) \\ \frac{dM_y}{dt} = -(\gamma H_0 - \omega)M_x + \gamma H_1 M_z - \frac{M_x}{T_2} & (2b) \\ \frac{dM_z}{dt} = -\gamma H_1 M_y - \frac{(M_z - M_0)}{T_1} & (3b) \end{cases} \tag{2.1.2}$$

With the modern pulsed NMR technique, the nuclear magnetization vector is altered from its equilibrium value by intense rf pulses ($H_1 \neq 0$), followed by the free evolution of the spin system ($H_1 = 0$). The rf pulses are usually short enough so that relaxions are negligible over their duration. If the rf field is resonant ($\omega = \gamma H_0$), the response to a pulse is the precession around a static effective field (in the rotating frame) $H_1\hat{x}$ by a nutation angle $\theta = \gamma H_1 \tau$, where τ is the pulse duration. Thus, by suitably tuning the pulse intensity H_1 and τ, one can obtain a

so-called 90° pulse ($\theta = \pi/2$) tilting the magnetization in the transverse *xy* plane; a 180° pulse ($\theta = \pi$) which inverts the nuclear magnetization; and so-on.
According to eq. 2.1.2 the evolution of M_{xy} in the rotating frame is an exponential decay

$$M_{xy}(t) = M_{xy}(0)e^{-\frac{t}{T_2}}$$

corresponding to a decaying free-induction (FID) signal detected by the pick-up coil wound around the sample. The time constant T_2 appearing in 2.1.2 T_2, however, comprises both static contributions (arising from a distribution of static fields) and dynamic ones. Nonetheless, the dephasing by static fields is *reversible* and it can be canceled out by a second rf pulse (ideally, a 180° pulse for optimum efficiency) which refocuses the spins. As a result, a spin echo appears after a delay t equal to the time separation between the two pulses. The intrinsic T_2 time, solely due to irreversible phenomena, is then measured by varying t and measuring the echo amplitude as a function of it. According to eq.2.1.2 the longitudinal magnetization tends to equilibrium by an exponential law with a characteristic time T_1,

$$M_z(t) = \left[M_0 + (M_z(0) - M_0)\, e^{-\frac{t}{T_1}}\right]$$

The evolution of $M_z(t)$ is probed by NMR along the following route. First, the longitudinal polarization M_z is prepared out of thermodynamic equilibrium by a suitable pulse sequence which "heats" the spin ensamble. The preparation is then followed by a free evolution of the spin system, during which it exchanges energy with the thermal bath and "cools down". Finally, $M_z(t)$ is detected by a one- or two-pulse sequence, producing a free-pecession or a spin-echo signal whose amplitudes are proportional to the longitudinal polarization prior to the detection sequence. The most common way of preparing the nuclear spins out of equilibrium is saturating the Zeeman transition, whence the method is referred to as saturation recovery. A saturation recovery sequence is shown in Figure 2.1.5 of section 2.1.

Nuclear Hamiltonian

A general form of the nuclear Hamiltonian that accounts for all the interactions acting on the nuclei is:

$$\mathscr{H} = H_Z + H_{n-n} + H_{n-e} + H_{EFG}, \tag{2.1.3}$$

where the first term is the Zeeman interaction, the second term represents the classical nuclear dipolar interaction, the third term describes the hyperfine interaction between the nuclear magnetic moment and the electronic magnetic moments, and the last one is the quadrupolar interaction. This last term will not be considered for the $^{53}Cr - NMR$, since quadrupole interactions are smaller compared to magnetic ones. The hyperfine field at the nucleus due to the electron spins can be derived by means of the classical expression of the magnetic dipolar interaction:

$$\mathscr{H}_{hyperfine} = \frac{\mu_0}{4\pi}\left(\frac{\bar{\mu}_e \cdot \bar{\mu}_n}{r^3} + \frac{3(\bar{\mu}_e \cdot \bar{r})(\bar{\mu}_n \cdot \bar{r})}{r^5}\right),$$

where $\bar{\mu}_n = \gamma_n \hbar \bar{I}$ is the nuclear magnetic moment, $\bar{\mu}_e = \gamma_n \hbar \bar{S}$ is the electronic magnetic moment, and r is the distance between the two magnetic moments. If we consider only the Zeeman and the hyperfine interaction the Hamiltonian 2.1.3 becomes:

$$\mathscr{H} = -\gamma_n \hbar \sum_i^{x,y,z} \bar{I}_i \bar{H}_i + \sum_i^{x,y,z} \sum_{j=1}^{N} A_i^j \bar{I}_i \langle \bar{S}_i \rangle^j$$

The first term is the Zeeman term interaction between the nuclei and the external magnetic field and the second term accounts for the hyperfine interaction. In fact, the hyperfine tensor A_i^j describes the interaction between the nuclear spin and the jth electronic moment along the ith-axis, $< \bar{S}_i >^j$ is the thermal average in the of the i-component of the jth electronic spin (where i = x,y,z). The coupling constant for the direct hyperfine interaction, between a nucleus and an electron described by the wavefunction ψ is given by:

$$A_\psi = \frac{2}{5} g \mu_B \gamma_n \hbar \left\langle \frac{1}{r^3} \right\rangle_\psi . \tag{2.1.4}$$

The above expression can not be used for *s-type* electronic wavefunctions, due to the non-zero probability of finding the electron at the nuclear position r=0. To overcome this limitation. Fermi renormalized the procedure leading to the following expression for the direct contact hyperfine constant:

$$A_s = \frac{8}{3} g \mu_B \mu_0 \gamma_n \hbar |\psi(0)|_s^2 , \tag{2.1.5}$$

where $|\psi(0)|_s^2$ is the normalized probability of finding an s electron at the nucleus. The previous expressions are used to calculate the hyperfine field at the ^{53}Cr nuclear site, being the electronic configuration for the chromium $[Cr^{3+}] = [Ar]3d^3$. The equation 2.1.4 is averaged over all the $3d$ electronic functions, obtaining a non-zero value, while equation 2.1.5 yields zero for the $3d$ functions. The $3s$ wavefunctions of the core electrons are polarized by the $3d$ electrons. This spin polarization effect results in a large hyperfine contact field named "core polarization field" to be added to the smaller contribution from equation 2.1.4. The magnetic $3d$ electrons couple antiferromagnetically to the core $3s$ electrons, while the core polarization at the ^{53}Cr nucleus, due to a single unpaired $3d$ electron, has been theoretically estimated to be: $A_{cp} = -12.5\ T/\mu_B$.
For a general review of the hyperfine interactions in magnetic materials we refer the reader to the seminal paper by Freeman and Watson, in Ref. [55].

Microscopic theory of the nuclear relaxations

The $1/T_1$ is a powerful probe of the electronic relaxation times in molecular nanomagnets, since the fluctuations of the hyperfine dipolar field, due to the thermal fluctuations of the electronic spins, are the cause of the irreversible relaxation of the nuclear spins. The relaxation of a non-interacting ensambles of nuclei in an external static magnetic field, coupled to the perturbative fluctuating field produced by the electronic spins can be described by the Redfield's theory [56], which is related to the treatment of the relaxation discussed by Wangsness and Bloch [57]. Following this theory, the fluctuating field is different for each nuclear site and it

can be written as:

$$H = H_{ext} + H_{hyper}(t) = -\gamma_n \hbar \left(H_{ext} I_z + H_{hyper}(t) \cdot \overline{I} \right),$$

where H_{ext} is the external magnetic field and $H_{hyper}(t)$ is the fluctuating hyperfine field:

$$\mathscr{H}_{hyper}(t) = -\hbar\gamma_e \sum_{i=1}^{N} \frac{1}{r_i^3} \left(\delta\overline{s_i}(t) - 3\overline{r_i} \left(\frac{\delta\overline{s_i}(t) \cdot \overline{r_i}}{r_i^2} \right) \right)$$
$$\delta\overline{s_i}(t) = \overline{s_i}(t) - \langle \overline{s_i} \rangle$$

where N is the number of magnetic ions and r_i their distance from the proton. The Redfield theory yields to exponential time decays of the longitudinal and transverse nuclear magnetization, with characteristic rates respectively given by [58]:

$$\frac{1}{T_1} = \gamma_n^2 \left[k_{xx}(\omega_L) + k_{yy}(\omega_L) \right]$$
$$\frac{1}{T_2} = \frac{1}{2T_1} + \gamma_n^2 k_{zz}(0)$$

where k_{qq} (q= x, y, z) is the Fourier transform of the correlation function of H_{hyper} and can be calculated in terms of the Fourier transform of the cross correlation functions of the electronic spin operators. Known the positions of the magnetic ions and that of nuclei in the molecule, the above mentioned equations become:

$$\frac{1}{T_1} = \sum_{i,j=1,N} \sum_{q,q'=x,y,z} C_{ij}^{qq'} \left[S_{s_i^q s_j^{q'}}(\omega_L) + S_{s_i^q s_j^{q'}}(-\omega_L) \right] \tag{2.1.6}$$

$$\frac{1}{T_2} = \frac{1}{T_1} + \sum_{i,j=1,N} \sum_{q,q'=x,y,z} K_{ij}^{qq'} S_{s_i^q s_j^{q'}}(0) \tag{2.1.7}$$

Where S are the Fourier transforms of the correlation functions related to the different components of the spin operators of each magnetic ions, C and K are the geometrical coefficients of the hyperfine dipolar interaction between the magnetic ions and the nuclei which only depend on their relative poitions [59]. The transverse relaxation rate $1/T_2$ contains also a temperature-independent contribution

originating from the nuclear dipole-dipole interaction among protons. At high temperatures, the electronic contribution to $1/T_2$ in Eq. 2.1.7 is small and only the nuclear dipole-dipole contribution survives. Thus we can take as a measure of the nuclear dipole-dipole contribution the experimental value of $1/T_2$ at high temperatures (above 50 K). The figure 2.1.1 schematically represents what happens during a NMR experiment, where we are measuring the temperature dependence of $1/T_1$. If we consider a system with a thermally activated dynamics and with only one dominating characteristic rate of relaxation τ, a peak in the $1/T_1$ is observed at the same temperature at which the Larmor frequency intersects the rate τ. For this reason the spin-lattice relaxation rate indirectly probes the electronic relaxation dynamic. In fact, by comparing experimental data with the calculated $1/T_1$ curve and by fitting the peak position, it is possible to determine the spin-phonon coupling strength (γ 1.3) , the only free parameter of our theoretical model for the electronic relaxation dynamics, which fixes the frequency-window of the dynamics. It is worth to stress that some molecules may be characterized by a relaxation dynamics with more than one dominating rate of relaxation, even at low temperature [60](more details will be shown in chapter 3.2).

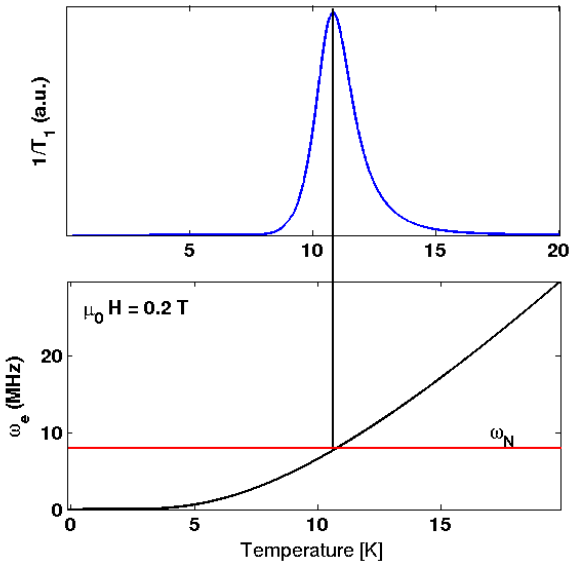

Figure 2.1.1: Thermally activated dynamics: when the Larmor frequency matches the electronic rate of relaxation, a peak in $1/T_1$ is observed.

Experimentally, the $1/T_1$ curves as a function of the temperature was constructed point by point. For each temperature the T_1 was measured by saturation recovery (shown the figure 2.1.5 in section 2.1) and fitted by a multi-exponential function.

Wipeout effect

NMR measurements in magnetic materials are often affected by the partial or total loss of the signal intensity at certain temperatures, usually referred to as wipeout. In general, the signal may be lost either due to the onset of large and inhomogeneous static internal fields at the nuclei, shifting the resonance outside the observed spectral window or broadening it so much that the signal falls below noise level; or to exceedingly fast dynamic spin-spin relaxations. The latter is actually the case of proton NMR in of MNMs, where the large T_2^{-1} relaxation rates reflect slowly fluctuating degrees of freedom in the electronic spin system, to which ^1H nuclei are coupled. The wipeout from dynamic relaxations is related to the dead time of the NMR receiver following the transmission of a rf pulse, which poses a cutoff to the measurable signals. Transverse nuclear magnetization components with T_2 relaxation times much shorter than the dead time decay in fact before their NMR signal can be observed. The dead time of the receiver depends in turn on the Q factor and the resonance frequency ν of the LC circuit in the NMR probehead, which takes a time of the order of several $\tau_{LC} = Q/\nu$ to discharge the high voltage of the rf pulses. Since Q typically increases on cooling, while it exhibits a minor on frequency, the dead time is longer (hence, the T_2 cutoff severer) at low frequency and low temperature. Experimentally, the number of protons $N(T)$ probed by the NMR signal is obtained by the initial transverse nuclear magnetization $M_{xy}(0)$ times the nuclear Boltzmann factor $\chi_n^{-1} \propto T : N(T) = M_{xy}(0)T$. $M_{xy}(0)$ is estimated by the extrapolating at zero time the transverse nuclear magnetization $M_{xy}^H(t)$, proportional to the integrated NMR spectrum, against the best-fit decay curve $M_{xy}(t)$ of the spin-echo amplitude vs. the delay $t/2$ between the two rf pulses in a $\pi/2 - \pi/2$ (or $\pi/2 - \pi$) echo sequence. If the relaxation of $M_{xy}(t)$ is single-exponential and its time constant T_2 is above the cutoff, $N(T)$ is constant with temperature. If on the contrary the spin-spin relaxation is non exponential

and relatively fast, the extrapolated $M_{xy}(0)$ will only account for part of the nuclei (the ones with longer T_2) and a missing fraction will show up in $N(T)$. In this case, $N(T)$ constitutes an indirect measurement of the spin-spin relaxation vs. T which is, however, more informative than the direct measurement of T_2 from the decay of the spin-echo amplitude, since the latter is a residual signal (that of the slower-relaxing fraction of nuclei).
Understanding the mechanism responsible for $T_2^{-1}(T)$ peak behind the wipeout behavior is important for the study of the dynamics of the MNMs. The $1/T_2$ rate reflects the irreversible dephasing of nuclear spins and it is due to two factors:

- the dipolar interaction among the proton nuclei, which is temperature and field independent;
- the dynamic contribution from the hyperfine interactions with the exchange-coupled magnetic ions, which depends on temperature.

In a first approximation, based on the weak collision model and the assumption of a fast electronic spin dynamics, $1/T_2$ can be expressed in terms of the spectral density of the fluctuating hyperfine field at zero frequency [61][62]:

$$\frac{1}{T_2} = \gamma_N^2 < \delta H_z^2 > f(\omega = 0) = \gamma_N^2 \frac{< \delta \mu_e^2 >}{r^6} f(\omega = 0) = \gamma_N^2 \frac{< \delta \mu_e^2 >}{r^6} \tau(H, T).$$

HereδH_z is the local longitudinal fluctuating field originating from a magnetic moment sitting at a distance r apart from the proton spin, and $\tau(T)$ is the correlation time governing the spin dynamics of the exchanged coupled magnetic ions. In the case of a slowdown in the magnetic fluctuations on cooling, or in the vicinity of a Level Crossing (LC), $\tau(T, H)$ becomes longer and longer, and this contribution eventually dominates over the nuclear dipole-dipole contribution. As a result, the relaxation time T_2 gets shorter and eventually crosses the experimental cutoff value below which the signal can not be detected (see above). Such a critical value is gradually reached by all the proton sites, with the ones closer to the magnetic ions being wiped out first, thus producing a a progressive decrease of the NMR signal intensity, which eventually is lost completely. This approach, namely, estimating the spin-spin relaxation from the missing signal, has been adopted in the past to study the relaxation dynamics of many molecular magnets [51, 63].

A more refined theoretical approach to the wipeout of the NMR signal, which mimics more faithfully what actually happens in an experiment, has been developed by the group of P.Santini and S.Carretta and employed in more recent literature papers, starting from a work on Fe_7 [60] . In particular, for each hydrogen site, the $1/T_1$ and $1/T_2$ rates are calculated as a function of temperature by means of equations 2.1.6 and 2.1.7. The effective $1/T_1$ of the residual signal (*i.e.* that of protons which are not affected by the wipeout), is then calculated by averaging over all the protons whose transverse relaxation rate is lower than a threshold value (a tunable parameter of the model, which is however constrained by the estimate of the dead time from the experimental conditions). Such an effective $1/T_1$ is to be compared with the experimental value. This last approach was also used to study the relaxation dynamics of Cr_9.

NMR Experimental setup

NMR experiments were performed in a Maglab $EXA^{®}$ (Oxford Instruments) cold-bore field sweeping superconducting cryomagnet with a variable temperature insert (VTI) as a sample environment, and a HyReSpect home-build NMR spectrometer equipped with an external rf power amplifier. The magnet features a fast (1T/min) fully software-controlled variation of the magnetic field in the 0-9 T range, at the expense of poor field homogeneity as compared to the normal NMR standards. The latter is however of no concern for NMR in magnetic materials, due to the broad resonance lines occurring therein, while sweeping the field is a crucial requirement. The VTI cryostat operates in a He flow taken from the same liquid He bath where the superconducting solenoid is immersed in, and provides stable temperature control from 250 K down to 1.4 K with a hold time of several days, which is another important condition for our experiments. The sample was placed in the coil of a resonant probe circuit, hosted by the VTI, which is detailed in the next section. The HyReSpect spectrometer is a general-purpose spectrometer for solid state NMR covering the 5-800 MHz frequency range entirely developed in our laboratory, particularly optimized for for the study of magnetism. Figure 2.1.2 shows a very sketchy and over-simplified block diagram of our NMR hardware, whose actual layout features a rather complex frequency up- and down-

conversion scheme in order to implement precise 4-quadrant phase modulation and quadrature detection [64]. Rectangular rf pulses of variable length are cut out of a continuous-wave signal source by a fast switch (rise time $<$ 10 ns) gated by a programmable digital pulser, while their level is controlled by a programmable attenuator in steps of 1 dB (not shown). The low-level pulses (peak power $\leq$ 1 mW) are amplified by a power rf pulse amplifier to a level in the order of 10-100 W, and then transmitted to the tuned LC resonator containing the sample coil. The latter serves both to excite the nuclear resonance by the rf magnetic field, and as a pick-up to detect the e.m.f. induced by the precessing nuclei. The NMR signal is then routed to a low-noise fast-recovery broadband preamplifier and to the receiver (RX) stage of the spectrometer. The transmitter (TX) and the RX stages are coupled to the probehead resonator and decoupled from each other by the passive circuit made by a resonant $\lambda/4$ transmission line and two pairs of cross-polarized silicon diodes, referred to altogether as a *duplexer*. The $\lambda/4$ line (*i.e.* a coaxial cable whose electrical length equals a quarter wavelength at the working frequency) acts as an impedance transformer, transforming a shorted end into a high impedance on the opposite side, and vice versa. The diode pairs are open circuits for the NMR signal, in the sub-mV range and hence below the conduction threshold of a silicon junction diode, while their are short-circuits for the high power rf pulses. It can be easily verified that the RX and TX lines are seen as high-impedance loads from the other side during, respectively, pulse transmission and signal reception, so that these two ports are effectively isolated. The diode pair in front of the preamplifier also serves as a protection from overvoltages which could otherwise damage it. The nutation angle $\theta = \gamma H_1 \tau$ of the spins, when the nuclear resonance condition is met, is controlled by the product of the pulse duration τ times the pulse amplitude, proportional to H_1. In principle, it may be optimized for maximum signal (attaining the $\theta = \pi/2$ condition) by adjusting either quantity. However, the large inhomogeneous linewidth typical of solids, in particular magnets, points to the usage of short and intense pulses in order to irradiate the largest frequency band and excite the maximum fraction of nuclei, possibly the entire NMR spectrum. The shortest pulses that we could apply were in the order of a few μs, whence an irradiated band in the order of few hundreds kHz. Spectra broader than such a value had to be recorded point by point at discrete frequencies.

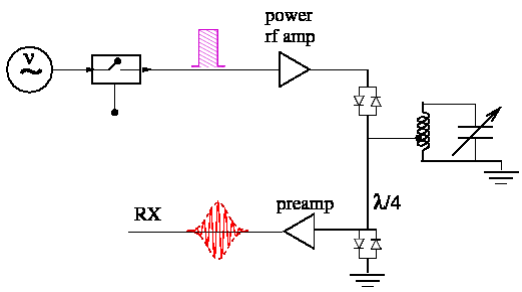

Figure 2.1.2: The diagram of the experimental circuit. On the top, from left to right: the radio frequency generator, the fast switch, the power RF amplifier, the the duplexer circuit (see the text) and the probehead. The duplexer also couples the probehead to the pre-amplifier and then to the spectrometer receiver (bottom).

Setting up an NMR experiment requires the optimization of a number of parameters, which are specific entries of the (*gtknmr*) GUI-based control program for the HyReSpect spectrometer [64]. The optimization of the pulse level controlled by their attenuation (TxAtt), and their duration (P1, P2, ... for the first, second, ... pulse, respectively) have been discussed above. The other most relevant parameters are listed below.

- The delay between the two pulses in a spin echo sequence (D1). Such a parameter is constrained on one hand by the transverse relaxation, which points to keeping the delay D1 much shorter thanT_2; on the other, by the dead time of the receiver, imposing that D1 is at least slightly longer than the dead time.

- The delay by which the signal acquisition is triggered after the last pulse. It is the sum of two events: a receiver inhibition time (Rinh) during which the rf RX stage is left switched off; and a so-called acquisition delay (Acqd) between the RX enabling and the actual triggering of the acquisition. The overall time must not exceed D1, hence it is limited by the dead time like the latter.

- The receiver gain, which actually controlled by a programmable attenuator between two amplifying stages. Its attenuation ratio (RxAtt) must be kept high enough to prevent the receiver saturation.

- The repetition time between two subsequent scans, often referred to as "relaxation delay" (RlxD). By "scan" it is meant a pulse sequence followed by the signal acquisition. A digitized NMR signal is typically obtained by acquiring and averaging several scans in order to obtain a good signal-to-noise ratio. The spin-lattice relaxation time sets a lower limit to RlxD, which must equal at least a few T_1 to allow a full repolarization of the nuclei between two scans. Another practical lower limit to RlxD, more important at lower temperature, is given by the heating of the sample by the rf pulses. On the other hand, an unnecessarily long RlxD leads to time consuming measurements, especially when a large number of scans is needed in order to extract poor signals from noise.

Probehead

The NMR probe is essentially a RLC resonant circuit, where L is the inductance of the coil wound around the sample (for maximum efficiency it filling factor must be as high as possible), R is the parasitic resistance of coil wire, and C is a variable capacitor. Owing to the latter, the circuit is tunable to a resonance frequency $\omega_0 \approx (LC)^{1/2}$ covering a broad frequency range. Obviously, $\omega_0 \approx (LC)^{1/2}$ is made to coincide with the Larmor frequency of the nuclei. The function the resonant circuit is, on one hand, applying a sizable rf magnetic field H_1 to the sample (in the order of several mT) with reasonable rf power, thanks to current gain in the coil by the quality factor $Q = \omega L/R$ of the resonator, typically in the order of hundreds. On the other hand, the emf induced in the coil is coupled to the coaxial cable with a similar voltage gain Q, as compared to the direct termination of the cable onto the coil. A schematic drawing of the probehead circuit is shown in fig. 2.1.3. With respect with to the simple series RLC circuit it is noteworthy, in parallel to it, the presence of a further, properly chosen, inductance L'. Its function is matching the impedance of the series RLC circuit, equal to $R < 1\Omega$ at resonance, to the characteristic $50\,\Omega$ impedance of the transmission lines (in other words, L' serves as an impedance transformer). In principle a high Q factor is desirable since it enhances the detection sensitivity, following the above argument, and it permits the excitation of the nuclei with reduced rf power. However, an excessively high Q factor

may be detrimental in the presence of a short relaxation time T_2, since it increases the dead time of the receiver, as it has already discussed in section 2.1. If the dead time is comparable or larger than T_2, the increased sensitivity produced by a larger Q is over-compensated by a dramatic decrease in the echo amplitude produced by a longer pulse separation D1, which is made necessary by an increased dead time. For this reason, sometimes the Q factor must be intentionally degraded by a resistor $R^{'}$ placed in parallel to the capacitor C.

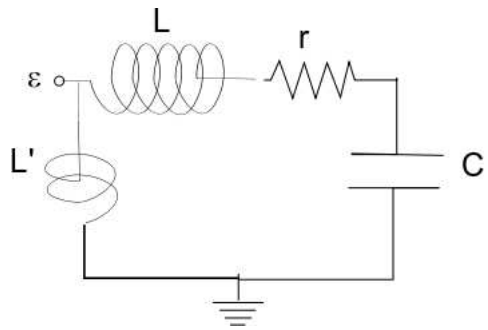

Figure 2.1.3: Tunable probe, necessary to match the characteristic impedance.

Pulse Sequences

We conclude this overview of the NMR technique with a few hints on the pulse sequences the were employed in this work. The NMR signal was always detected by means of a $\pi/2-\pi/2$ echo sequence. The latter was preferred to the textbook $\pi/2-\pi$ Hahn echo sequence, in principle more efficient because of the short T_2 in our systems, so that the longer duration of a $\pi/2-\pi$ sequence may become critical. Moreover, in the presence of broad resonances as in our case, the second π pulse might excite just a fraction of the spectrum rather than the entire line, due to its reduced spectral width, which makes it theoretical benefit questionable in practice.

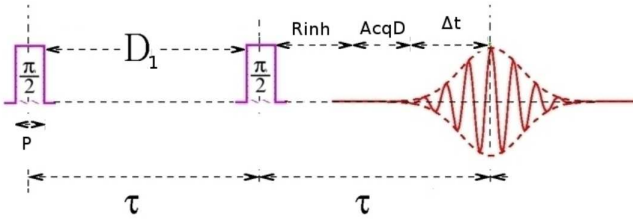

Figure 2.1.4: Spin echo sequence for the measurement of the spin-spin relaxation time T_2

The $\pi/2-\pi/2$ sequence is sketched in figure 2.1.4, showing also the experimental parameters *Rinh* and *AcqD* explained above. The spin-spin relaxation function is determined experimentally by measuring spin echoes at different delays D_1. Over the different spin echo measurements, either *Rinh* or *AcqD* is varied by the same increment as D_1, which ensures that the signal acquisition is triggered at a constant time before the spin echo. The decay of the spin echo amplitude A is then governed by the total delay $2(D_1+P_1)$ between the first pulse and the echo center, and follows follows a $A = A_0 \exp(2(D_1+P_1)/T_2)$ dependence in the case of an exponential relaxation with a single time constant T_2. The spin-lattice relaxation timeT_1 can be measured by the saturation recovery method, shown in figure 2.1.5. An aperiodic $\pi/2$ pulse train, with an average pulse spacing in the order of T_1 and an overall duration in the order of T_1, prepares the spin system in a state with virtually no net polarization (saturation), corresponding to an infinite spin temperature. After the pulse train is switched off, the spins repolarize thanks to spin-spin relaxation process. The spin repolarization is probed by a spin echo detection sequence, producing a spin coherence in the *xy* plane proportional to longitudinal magnetization just before the detection pulses. The saturation recovery sequence is repeated at different evolution times D_1, thus obtaining an experimental saturation recovery curve.

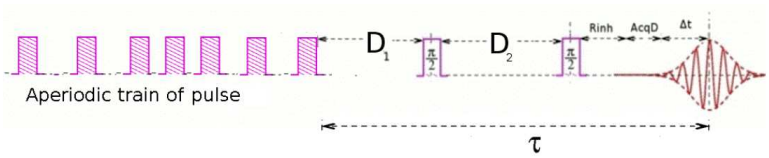

Figure 2.1.5: Sequence for the measurement of the spin-lattice relaxation time (T_1).

2.2 Muon Spin Relaxation (μSR)

In this paragraph the main characteristics of Muon Spin Spectroscopy (historically known as μSR, for Muon Spin Rotation, or Relaxation) are presented. The technique employs the muon as a local probe to study the properties of electrons and molecules in matter[65, 66, 67, 68]. The muon is an unstable elementary particle, originated by protons impinging on a solid target, via the intermediate production of spin S = 0 pions. Muons can be generated with 100% spin polarization, thanks to parity violation in the pion decay, and stopped inside the material under investigation. The mean lifetime of the muon is roughly $2\,\mu s$ (see table 2.1). This sets the time-scale traced by the evolution of the spin of implanted muons, that is related to the local magnetic field at the muon site. On this time-scale the spin direction can be monitored as a function of time over a statistical ensemble of muons, thanks, once more, to parity violation in the weak muon decay into two neutrinos and an electron, since the muon spin direction at the time of the decay is strongly correlated with the direction of emission of the latter. Thus muon spin spectroscopy provides very similar information to NMR, with two specific advantages:

- A gyromagnetic ratio on average at least one order of magnitude larger than that of good nuclear moments (over three times that of hydrogen), giving enhanced sensitivity to low internal fields, and thus access to a distinctly larger frequency window;
- The possibility to implant the probes in any sample (whereas NMR must rely on having a "good nucleus" in the chemical composition of the sample)

The table 2.1 reports also other physical properties of positive muons.

μ^+ properties	value
charge (q_μ)	e = 1.60217733(49)$\cdot 10^{-19}$ C
spin (I_μ)	1/2
mass (m_μ)	105.65839(34) MeV/c^2$\sim$ 0.12 $m_p$$\sim$205 m_e
magnetic momentum (μ_μ)	$4.88 \cdot 10^{-3}\mu_B \sim 8.9\mu_N$
gyromagnetic ratio ($\gamma_\mu/2\pi$)	135.53420(51) MHz/T
mean lifetime (τ_μ)	2.219703(4) µs

Table 2.1: Main properties of positive muons .

High intensity, spin polarized muon beams are produced using proton accelerators. After the collision of two protons or a proton and a neutron, a π^+ is produced. The pion half life-time is just 26 ns and from its decay a positive or negative muon is produced via a two-body decay, as depicted in Figure 2.2.1.

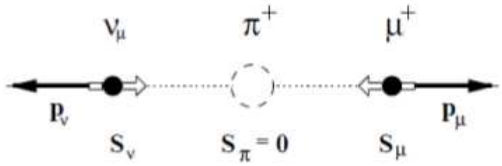

Figure 2.2.1: Scheme of the pion decay.

In its application as a condensed matter spectroscopy, the μSR technique has been mainly developed for the positive particles, since they do not undergo nuclear capture, as negative muons do. Nuclear capture adds its atom-dependent, largely unknown mean lifetime to the total decay time of the probe. The accurate determination of the muon spin evolution relies on the very precise knowledge of the latter (see Tab. 2.1), hence it can be done for the positive muon only. Positive muons in condensed matter behave as light isotopes of hydrogen nuclei. Entering the sample muons quickly lose their excess kinetic energy until thermalization. In molecules and molecular crystals they form a bond in an epithermal reaction similar to protonation. The larger the molecule the more inequivalent additions result from this process, yielding a finite but possibly large number of slightly inequivalent probes, that will be integrally sampled in the ex- periment with amplitudes depending on their formation probability. The implanted muon localizes in a few hundreds picosecond. As mentioned above the muon decays into a positron and two neutrinos:

$$\mu^+ \rightarrow e^+ + \nu_\mu + \overline{\nu}_\mu$$

Parity violation of the weak decay, together with the conservation of energy, linear and angular momentum, implies an asymmetry in the positron emission direction (see figure 2.2.2). The direction of the emitted positron, the only detected particle in a μSR experiment, is correlated with the instantaneous direction of the

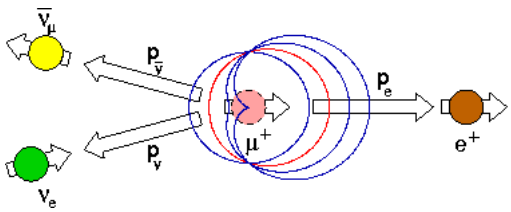

Figure 2.2.2: Asymmetry in the three body decay.

muon spin that at the time of decay. It is easy to see why this happens when the positron is emitted opposite to both neutrinos, at the maximum positron energy $E_{max} \cong 50MeV$. The two neutrinos are a pair of particle and antiparticle, and parity violation imposes that they have opposite helicity, *i.e.* spin parallel or antiparallel to their common linear momentum (specifically, the electron antineutrino along and muon neutrino opposite to momentum). Since the positron for E = E_{max} is highly relativistic, it must also have its spin almost parallel or antiparallel to its momentum. Parity violation, once again, imposes the parallel direction for an antiparticle. Hence in this particular geometry the positron is emitted with full asymmetry, only and almost exactly along the muon spin. However the muon decay is a three body decay with a spectrum of energies and on average the asymmetry is lower than full. The spec- trum of positron energies ranges between zero and E_{max}. The positron emission probability as a function of its energy is given [67] by:

$$P(\theta) = \frac{1}{2\pi} p(E^*)\,(1 + A(E^*)cos(\theta))$$

where

$$E^* = \frac{E}{E_{max}}$$

$$p(E^*) = \frac{2(E^*) - 1}{3 - 2(E^*)}$$

with an energy dependent asymmetry parameter:

$$A(E^*) = (E^*)^2(3 - 2(E^*))$$

Here, θ is the angle between the muon spin and the positron emission direction, $p(E^*)$ and $A(E^*)$ are the relative emission number and the asymmetry function. Notice that A(1) = 1 as anticipated. By averaging P(E) over the all positron energies, which is roughly equivalent to the integral positron detection performed experimentally, we obtain:

$$A_0 = \langle A(E^*) \rangle = \int_0^1 A(E^*) p(E^*) d(E^*) = \frac{1}{3}$$

The non-zero value of the asymmetry parameter implies that, overall, the positrons are still emitted preferentially along the muon spin direction. Let us see how to exploit this asymmetry in simple cases, for instance when the presence of a transverse magnetic field causes the precession of the implanted muon spin or when there is no precession. The positron count rate in a detector as a function of time is given by :

$$N(t) = N_0 \left[e^{-\frac{t}{\tau_\mu}} (1 + A_0 P(t)) + C \right],$$

Here P(t) is the spin polarization function, representing the projection of the muon spin unit vector at time t along the detector axis, that contains information about the sample, C is an unavoidable time-independent count rate of uncorrelated events, and N_0 is the unpolarized initial rate. Let us assume that the muon site is unique. Further assume that the unique local magnetic field B (internal of externally applied) is along $\hat{z}$ and that the axis of the detector lies along $\hat{x}$. In this case, referred to as transverse field (TF), the polarization function is

$$P(t) = G_{xx}(t) cos(\gamma_\mu B t + \theta)$$

Therefore, the positrons are emitted preferentially along the muon spin direction. When the muon is implanted in the sample, the presence of a transverse magnetic field causes the precession of the muon spin. Furthermore, if the projection of the spin along the axis of the detector changes with time, the anisotropy of A varies and the time dependent count of detected positrons can be written as:

$$N_{e^+}^{(i)}(t) = N_{e^+}^{(i)}(0) \left[e^{-\frac{t}{\tau}} (1 + \widetilde{A} P^{(i)}(t)) + B_0^{(i)} \right],$$

where θ is the angle between the initial muon spin direction and x, zero in the present special case. Therefore a coherent spin precession is directly observed as a time oscillation at the Larmor frequency $\gamma_\mu B$ in the positron count rate. The factor G_{xx} is the spin relaxation function describing the decay envelope of the oscillation. It originates from spin interactions analogous to those leading to NMR T_2 relaxation (see Section 2.1). To be more precise, without the use of resonant radio frequency pulses, like those employed in NMR, it is impossible to select the dynamic part of the muon spin relaxation caused by time dependent excitation coupled to the muon spin. Therefore the decay of the TF μSR polarization is normally dominated by T_2^*(see Section 2.1).

In the other simple case, when the local field is either zero (ZF) or along the initial muon spin direction (longitudinal, LF) the polarization corresponds to the longitudinal relaxation $P(t) = G_{zz}(t)$, and it is entirely analogous to the NMR T_1 relaxation of a spin 1, *i.e.* a single exponential decay in simple cases (see Section 2.1).

When muons stop in two or more inequivalent sites the polarization must be substituted by a sum of similar terms, weighted by the probability of occupation, or fraction f_j, of each site j. This is the so called (time-differential) asymmetry function $A(t) = A_0 \sum_j f_j P_j(t)$. In order to easily extract it from positron counts, instruments generally have pairs of nearly equivalent opposite detectors, (i,k) so that the function is obtained as

$$A(t) = \frac{\left(N^i(t) - C^{(i)}\right) - \left(N^k(t) - C^{(k)}\right)}{N_0^{(i)} + N_0^{(k)}}.$$

The ratio of the two detector efficiencies, α, may be used to renormalize one of the two count rate.

Experimental Setup

The μSR experiments reported in this work of thesis were carried out on the GPS spectrometer at the continuous muon source of the SμS facility at the Paul Scherrer Institute (PSI) in Villigen (Switzerland). Figure 2.2.3 shows a sketch of the GPS detectors.

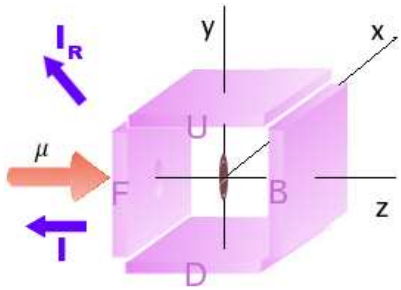

Figure 2.2.3: Sketch of GPS spectrometer. The four detectors are called F (forward), B (Backward), U (up), and D (down).

With this instrument the four detectors may be grouped in two pairs (U-D and F-B), when a transverse field is applied along $\hat{x}$, or in just two groups ((U+F)-(D+B)), in a ZF configuration with the initial muon spin turned nearly 45 degrees from $\hat{z}$ towards $\hat{y}$ by an *ad-hoc* upstream spin rotator. This last setup is the one adopted to look for internal magnetic fields and longitudinal T_1 relaxations. Magnetic fields exceeding 10 mT must be applied along the incoming beam direction to avoid strong deflection of the low momentum (p≈26 MeV/c) charged muons, resulting in their implantation outside the sample. In this case one can measure spin precessions around the applied field in the U-D pair of detectors, with the rotated initial spin. Longitudinal relaxation can be measured in the F-B detectors by leaving the initial muon spin along the beam. Generally, since the relative efficiencies of the four detector depends strongly on the exact position of the sample in the detector setup, a low field TF experiment is carried out at high temperature to calibrate the experiment after each sample mounting. A fit of these calibration data provides the value of the detector dependent constants influencing the count rates, specifically the ratio α of the detector efficiencies. It furthermore provides the reference maximum asymmetry A_0 , in the simple case, or a corresponding effective quantity that takes into account also the sum of observed muon fractions and other experimental effects. In the case of our single molecule magnets the rest of the experiment is carried out either in zero or in longitudinal field, to investigate the field dependence of the longitudinal T_1 relaxation induced by the electron spin dynamics of the single molecule.

Relaxation functions

For the sake of completion we describe below a few other relaxation functions that are relevant for μSR studies in magnetic materials. They are relevant also for single molecule magnets although we have not employed them in the investigations reported in this thesis. In the simplest single crystal experiment on a ferromagnet, an antiferromagnet of a ferrimagnet, muons stop at a unique site, characterized by a single value of the local magnetic field **B**. The field however may form any angle θ with the initial muon spin direction, depending on the single crystal orientation. In this case the muon spin will precess around the magnetic field **B** along a cone of aperture θ . Assuming the initial spin direction along the axis of a detector pair the measured polarization is given by:

$$P(t) = cos^2\theta + sin^2\theta cos(\gamma_\mu |\mathbf{B}| t)$$

The squared cosine term is the so called longitudinal component, due to the projection of the muon spin along the field direction. This component does not change during the precession and it may be relaxed by fluctuating transverse fields. It is therefore multiplied by a relaxation function of the type $G_{zz}(t)$, a T_1relaxation function. The squared sine term is the precessing, or transverse component and it decays according to $G_{xx}(t)$, a T_2-like relaxation. In a polycrystal the direction of the local magnetic field varies randomly among domains. The polycrystal average in this case yields:

$$P(t) = \frac{1}{3} + \frac{2}{3} cos(\gamma_\mu |\mathbf{B}| t)$$

where $\frac{1}{3}$ constant may be viewed as the average longitudinal component and the $\frac{2}{3}$ amplitude of the precession corresponds to the average transverse components. They are therefore relaxed according to the functions described before

$$P(t) = \frac{1}{3} G_{zz}(t) + \frac{2}{3} G_{xx}(t) cos(\gamma_\mu |\mathbf{B}| t)$$

Another case of interest is when the components of the local field at the muon (unique) site are randomly distributed. The observed polarization function is the so-called static Kubo-Toyabe (KT) function, [69], with two significant examples

(shown in Fig. 2.2.4). In particular, the Gaussian form of this function

$$G_G(t) = \frac{1}{3}\left[1 + 2(1 - (\Delta t)^2)e^{-\frac{(\Delta t)^2}{2}}\right]$$

is appropriate to describe the case of a muon surrounded by the randomly oriented nuclear magnetic moments, or a similar distribution of electronic moments. On the other hand, the Lorentzian KT function

$$G_L(t) = \frac{1}{3}\left[1 + 2(1 - (\Delta t)e^{-\Delta t}\right]$$

better describes the same systems in the diluted regimes (*e.g.* when nuclei with zero spin are much more abundant than nuclei with a spin).

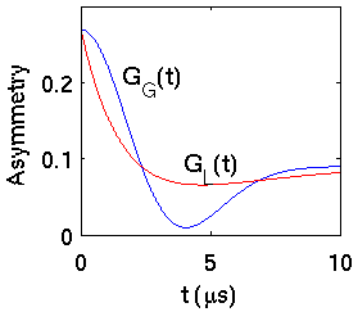

Figure 2.2.4: Examples of Kubo-Toyabe relaxation functions. Blu line: Gaussian distribution of fields. Red line: Lorentzian distribution fields. Both functions recover one third of the initial asymmetry at long times, corresponding to the average longitudinal component of the local fields over the distribution.

2.3 SQuID-magnetometry

The DC and AC magnetometric measurements were performed on a MPMS XL-5 SQuID (Superconducting Quantum Interference Device) magnetometer. With this instrument it is possible to perform measurements as a function of the applied magnetic field (variable between -5 and 5 T; *i.e.* hysteresis loops), of temperature (variable in the range 2-400 K), and frequency (1 Hz to 10 kHz; *i.e.* AC susceptometry). The instrument is equipped with a helium flow cryostat. We illustrate here its working principle in the dc operating mode, the ac susceptometer being a

variant of this scheme. The instrument is based on the superconducting quantum interference phenomenon occurring in a sensor consisting of two Josephson junctions connected in parallel (superconductor-insulator- superconductor). The phase of the superconducting order parameter is modulated by the presence of magnetic flux in the area of the junction, that changes by 2π whenever the magnetic flux changes by the flux quantum $\phi_0 = 2.07 \times 10^{-15} Wb$. The device is not directly coupled to the field from the sample. To further enhance sensitivity the SQUiD is inductively coupled to a closed circuit of four identical, oppositely wound, superconducting coaxial coils, providing a second order gradiometer. A magnetic field gradient from a point sample couples to the gradiometer, generating a net flux through the four coils that is maximum when the sample is balanced between the two central coils and minimum when displaced either to the left or to the right (see figure 2.3.1). The flux can be measured by reading indirectly the compensating voltage that must be inductively fed to the circuit to keep the SQuID at zero phase, *i.e.* in the condition that maximizes its superconducting amplitude. The magnetic moment of the sample is normally generated by a uniform magnetic field provided by a superconducting solenoid. The second order gradiometer guarantees insensitivity to this main field.

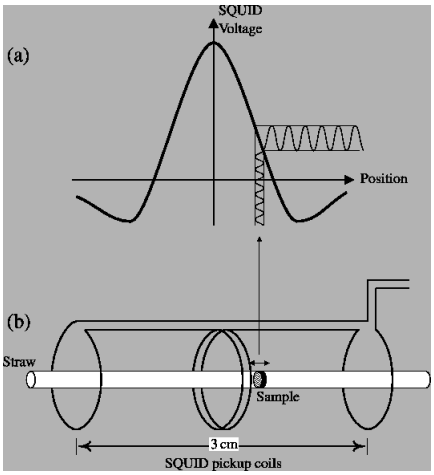

Figure 2.3.1: Centering of the sample in a second order gradiometer (bottom figure) and the detected voltage signal (top figure). The detection coils are constituted by a single superconducting wire wrapped in a set of four coils in the configuration of the second order gradiometer, in order to cut the inhomogeneity of the magnetic field.

The signal shown at the top of figure 2.3.1 is generated by lifting or lowering the sample coaxially with the gradiometer in the region of maximum field homogeneity. The signal is fitted to a standard shape function, whose amplitude is proportional to the magnetic moment of the sample. In the dc measurement the variation of the external magnetic field takes place in steps, and the measurements are performed after each steps. The ratio of the measured magnetic moment m to the field intensity is proportional to the dc susceptibility, in the small field limit. In the ac measurements an additional small amplitude uniform field is superimposed to the static one. The gradiometer is again insensitive to the flux due to this field, thanks to its uniformity, and measures instead the instantaneous induced response to the alternating gradient of the sample. The ac susceptibility, the derivative of the measured magnetic moment per unit volume M with respect to applied field H, is thus recorded. In this case SQUID circuits including the double gradiometer and the feedback system are read by a lock-in amplifier according to the scheme of figure 2.3.2.

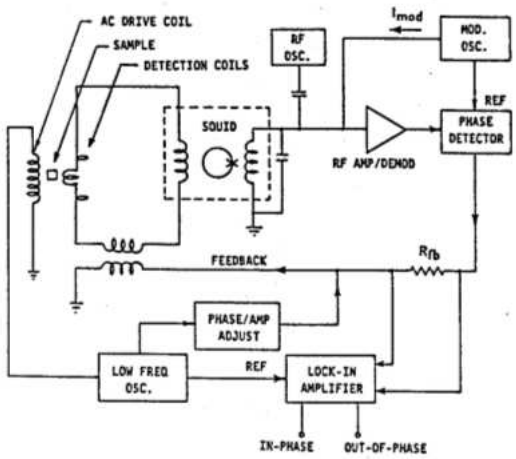

Figure 2.3.2: The measuring circuit of the ac RF-SQUiD susceptometer. The lockin amplifier records the in-phase and out-of-phase response signal to the low frequency excitation.

In the literature it is common to report the χT as a function of temperature to highlight deviations from the paramagnetic behaviour of non interacting spins

(where χT assumes a constant value), as predicted by the Curie law:

$$\chi T = \frac{Ng^2\mu_B^2}{3k_B}S(S+1).$$

Curie-Weiss behavior consists in a similar linear higher temperature regime above $|\Theta|$,

$$\chi(T-\Theta) = \frac{Ng^2\mu_B^2}{3k_B}S(S+1)$$

and in a different functional form for $T < |\Theta|$. An estimate of the magnetic moment is readily extracted from a fit to the above formulas, while magnetic couplings can be extracted from the critical temperature, approximated either as the intercept$|\Theta|$between the temperature axis and the linear fit of the Curie regime or from the low temperature behavior. Positive intercept is indicative of a ferromagnetic coupling and negative intercept is indicative of an antiferromagnetic coupling, although more complex cases may occur. The temperature dependent magnetization and susceptibility are generally measured distinguishing between Zero Field Cooling (ZFC) or Field Cooling (FC) measurements. In the former case, the sample is cooled at the base temperature in zero field and then measured by rising the temperature under an applied magnetic field. In a FC measurement, the sample is cooled in an applied magnetic field and measured both during cooling and during the subsequent heating. The differences between FC and ZFC are important in those systems that show non reversible processes, such as superparamagnets, spin glasses, and superconductors.

AC measurements

AC susceptibility[70, 71, 72] is a sensitive technique especially useful for the investigation of phase transitions and magnetic relaxations [73]. An alternating current flows through the coil, generating a small oscillating magnetic field (H_1) that usually does not exceeds 10 Oe. The measurement can be done also in a static field (H_0), parallel to the oscillating field, so that the effective applied magnetic field becomes:

$$H = H_0 + H_1 cos(\omega t),$$

where ω is the angular frequency of the AC-current.

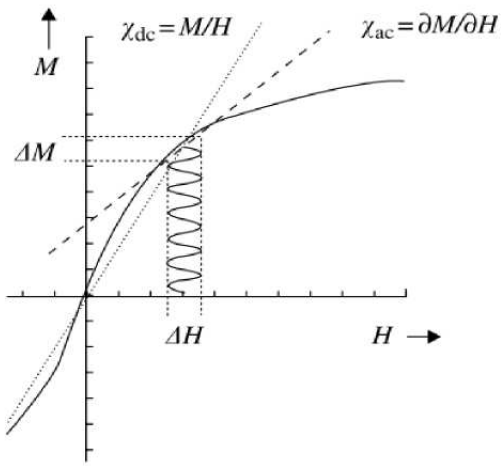

Figure 2.3.3: A schematic magnetization curve explaining the differences between χ_{DC} and χ_{AC}[1].

The magnetization response of the sample can be a non-linear function of the field (H), as shown in figure 2.3.3. Anyway, for small field oscillations the response is in general linear and $\Delta M/\Delta H$ corresponds to the susceptibility. The major advantage of this technique resides on the fact that the dynamics of the magnetization can be easily investigated by varying the frequency (ω). The AC susceptibility is a complex value and can be written as

$$\chi_{AC} = \chi' - \chi'',$$

where the real part (χ') is related to the reversible magnetization process, in-phase with the oscillating field, while the imaginary component (χ'') is related to losses due to irreversible magnetization processes. The thermodynamic model for the relaxation of a magnetic system in the oscillating field was derived by Casmir and du Pré [74], in terms of the adiabatic $\chi_S = \left(\frac{\partial M}{\partial H}\right)_S$ and isothermal $\chi_T = \left(\frac{\partial M}{\partial H}\right)_T$ susceptibilities:

$$\chi(\omega) = \chi_s + \frac{\chi_T - \chi_s}{1 + (i\omega\tau)}.$$

The complex $\chi(\omega)$ has real and immaginary components:

$$\chi' = \frac{\chi_T - \chi_s}{1+\omega^2\tau^2} + \chi_s$$

$$\chi'' = \frac{(\chi_T - \chi_s)\omega\tau}{1+\omega^2\tau^2},$$

where χ_T is the isothermal susceptibility in the low frequency limit ($\omega\tau \ll 1$) and is related to spin-lattice relaxation. χ_S is the adiabatic susceptibility, in the high frequency limit ($\omega\tau \gg 1$). The latter case is related to spin-spin relaxation processes, when the system has no time to exchange energy with the external world. The parameter τ is the time required to reach the thermal equilibrium. When the dynamics of the relaxation process is described by a well behaved, symmetric distribution of relaxation times, rather than a single time τ, a simple empirical law may be considered:

$$\chi(\omega) = \chi_s + \frac{\chi_T - \chi_s}{1+(i\omega\tau)^{1-\alpha}}.$$

Here τ is the average value over the distribution, i.e the central value. The parameter $\alpha > 0$ is related to the width of the distribution, since $\alpha = 0$ reproduces the case of a single relaxation time. In molecular magnets the measurements of the ac susceptibility is usually car- ried out by varying the temperature at a relatively small number of frequencies. If τ changes with temperature, as in mechanisms involving energy exchange with the phonon bath, the condition $\omega\tau(T) = 1$ corresponds to a maximum in the imaginary part of the susceptibility (χ''), as it can be seen *e.g* by inspection in the previous equation.

Probing electron spin dynamics

Cc-susceptibility NMR, and μSR relaxations give access to low frequency electron dynamics. They involve the transition between electronic spin states, either directly, as in the case of the magnetic susceptibility, or indirectly, through the nuclear or muon coupling to the electron susceptibility. In the case of susceptibility, energy conservation requires that an additional excitation is involved, and the most common is a phonon mode, *i.e.* a quantized collective motion of atoms

in the molecule or in the lattice. Since the electron gyromagnetic ratio is much larger than those of the spin probes, either the muon or the nucleus, the spin flip of an electron typically does not match in energy the spin flip of muons or nuclei. This implies that energy cannot be conserved in a process involving only the spin probes and the electrons. Also in this case the consequence is that phonons must be involved. A more detailed description of the possible relaxation processes can be found in the literature [42, 75]. Here, a brief account of phonon driven relaxation mecha- nisms is reported. In the case of molecular magnets, we distinguish three different phonon processes:

- The *direct process* takes place when the energy of the spin transition matches exactly the phonon energy, so that a direct transfer may take place between the spin system and the lattice phonon bath (case *a* in figure 2.3.4)

- A *Raman process* is a two-phonon process, involving the absorption of a phonon of energy $h\nu_1$ from an excited electron state and its relaxation to the ground state with the subsequent emission of another phonon of energy $h\nu_2$.The energy of the spin transition must be equal to the difference of the two phonon energies, $h(\nu_1 - \nu_2)$(case *b* in figure 2.3.4).

- An *Orbach process* is a two-phonon process in which one of them, $h\nu_1$ is absorbed by an excited state 2, inducing its transition to a higher excited state, 3. The relaxation of 3 to the ground state, 1 , is accompanied by the emission of a larger energy, $h\nu_2$phonon. Energy conservation imposes that $E_2 - E_1 = h(\nu_2 - \nu_1)$ (case *c* in figure 2.3.4).

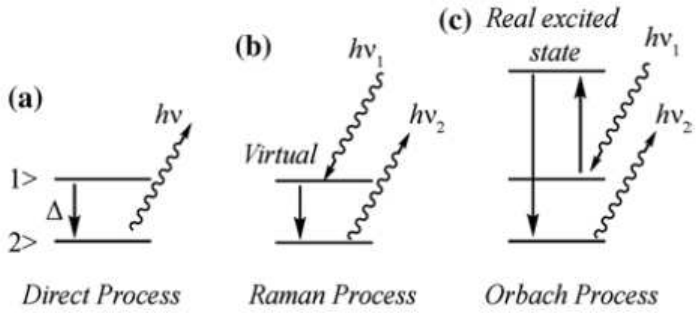

Figure 2.3.4: Phonon-assisted relaxation. (a) Direct relaxation into the ground state under the emission of a phonon, (b) The two-phonon Raman process, (c) The two-phonon Orbach process[75].

Since the flip of the spin probe has a non-vanishing energy cost, the energy conserving direct process, where a phonon is directly absorbed or emitted to cause an electron spin transition, cannot contribute to NMR and μSR relaxations. Therefore they are dominated by Raman and Orbach processes.

Chapter 3

Regular closed ring: The case of Cr_9

One of the most studied AF rings is Cr_8[76, 77, 48, 78, 79], which is formed by eight AF-coupled Cr^{3+} ions (s = 3/2)[15, 80]. Heterometallic rings with a magnetic ground state can be obtained from homonuclear ring by chemical substitution of one or two magnetic centers. In particular, Cr_7M rings (M = Zn, Cd, Mn, Ni) are derived from Cr_8 by substitution of one divalent cation M for a trivalent Cr ion [81]. The attention is now focusing on the last missing members of the AF rings family: closed rings characterized by an odd number of magnetic ions. This kind of molecules is very important because they can be considered as model systems for the study of frustration-induced properties. Indeed, if these rings have a regular geometry and half-integer local spins, they obey the definition of degenerate frustration given by O. Kahn [82], displaying a degenerate pair of S = 1/2 doublets as ground states. However, sizeable structural distortions in the geometry of these molecular polygons lead to the removal of frustration and thus of the degeneracy in the ground state, even if there are still competing AF interactions [82]. The first example of AF ring with $N = 9$ is Cr_8Ni [83, 84], which however is not frustrated since the Ni^{2+} ion breaks the nonagonal symmetry. The first examples of Cr_9 rings have been synthesized and studied [85], but none of them displays the characteristics of a degenerate-frustrated ring. Indeed, they all have at least one significant bond defect, leading to a sizeable removal of the degeneracy in the S = 1/2 ground state or even to a ground state with S > 1/2. In this paragraph, we investigate the magnetic properties and the phonon-induced relaxation

dynamics of the the first regular $Cr_9F_9\{O_2CC(CH_3)_2\}_{18}$ molecule, in short Cr_9, which represents a prototype of a practically degenerate-frustrated homometallic ring [52]. In this compound all the Cr-Cr edges are bridged in the same way, by one fluoride and two pivalate ligands (see Figure 3.0.1) and susceptibility and low temperature magnetization measurements are very well reproduced by assuming a single exchange constant.

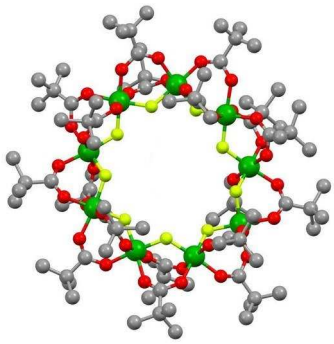

Figure 3.0.1: Molecular structure of $Cr_9F_9\{O_2CC(CH_3)_2\}_{18}$, in short Cr_9. In Green, Cr; red, O; grey, C; yellow, F (hydrogen atoms are omitted for clarity).

While magnetic relaxation in even-membered AF rings like Fe6 and Cr8 has already been theoretically and experimentally investigated, no equivalent experimental or theoretical studies exist on frustrated AF rings. The molecule contains nine AF-coupled Cr^{3+} ions (s_i = 3/2) and it can be described by the following spin Hamiltonian:

$$\mathscr{H} = J\sum_{i=1}^{9}\mathbf{s}_i\cdot\mathbf{s}_{i+1} + g\mu_B\mathbf{B}\cdot\sum_{i=1}^{9}\mathbf{s}_i, \tag{3.0.1}$$

where the first term represents the isotropic Heisenberg exchange interaction, with the same exchange parameter J for all the Cr-Cr bonds, while the last one is the Zeeman coupling to an external magnetic field. Previously studied Cr_9 molecules have had one significant bond defect, with only one pivalate and one fluoride on one Cr-Cr edge [86], leading to a significantly weaker exchange interaction between those two Cr^{3+} ions. The Cr_9 variant studied in this thesis, has identical bridging on each edge, with one fluoride and two pivalates present on each edge. Therefore, this is the first case of a Cr_9 ring in which the C_9 symmetry axis is preserved and not removed by local distortions. This can prove to be interesting since

frustration in molecular nanomagnets yields energy spectra with degenerate levels and novel physical properties, which affect their relaxation dynamics [87, 60]. The exchange parameter was determined by susceptibility and low-temperature magnetization measurements (Fig.3.0.2). DC SQUID magnetometry has been performed on a powdered sample of Cr_9 on a MPMS XL-5 SQUID magnetometer, in the temperature range of 2-300 K and field range of 0-5 T.

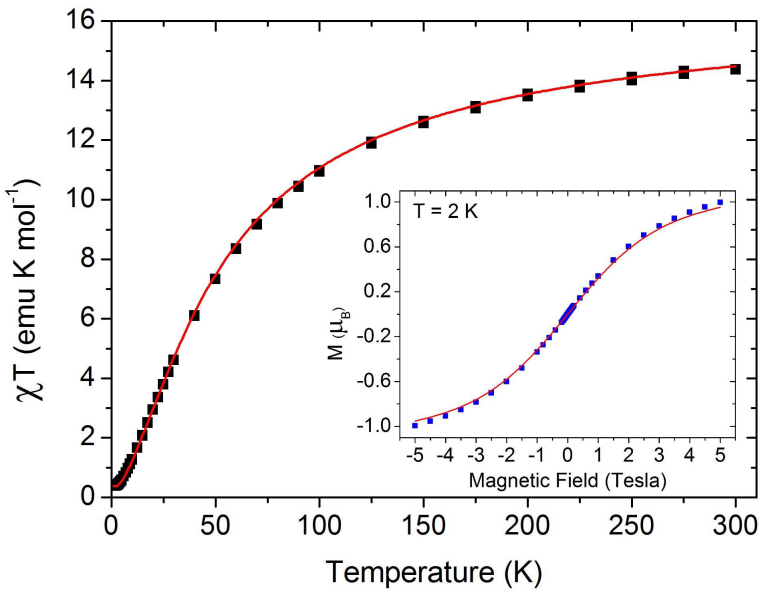

Figure 3.0.2: The temperature dependence of the χT of Cr_9 (black squares) is compared with the theoretical model (solid line). Inset: Experimental (blue squares) and calculated (solid line) magnetization per molecule at T = 2 K as a function of the applied magnetic field. All the calculations were made with the Hamiltonian 3.0.1 J = 1.35 meV and g = 1.98.

The monotonic decrease of the χT highlights the presence of dominant AF interactions within the molecule, leading to a low-spin ground state. Moreover, the low-temperature magnetization curve saturates to $1\mu_B$, suggesting an S = 1/2 ground state (see figure 3.0.2. The measurements are well reproduced by the model Hamiltonian of Eq. 3.0.1 with a single AF exchange parameter J = 1.35 meV. Within this model, the Cr_9 molecule has a perfect C_9 symmetry and, therefore, geometrical frustration. Figure 3.0.3 shows the spectrum of the energy levels as a function of the total spin of the molecule.

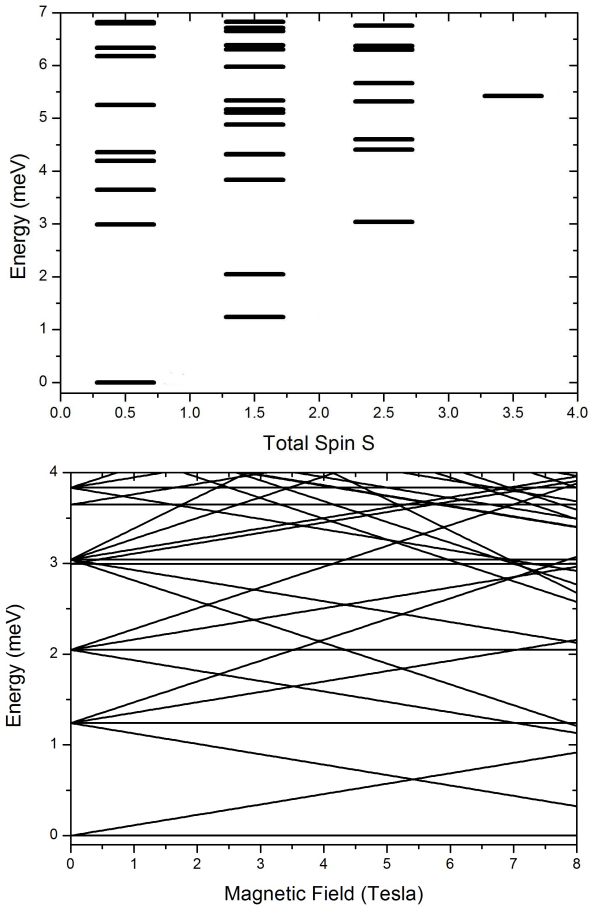

Figure 3.0.3: Top: Spectrum of the energy levels calculated with Hamiltonian in Eq.3.0.1 with J=1.35 meV and B = 0. Energy levels are arranged into multiplets of given total pin S with degeneracy (2S + 1). Due to frustration, the lowest total-spin multiplets are two-fold. Bottom: the lowest total-spin multiplets are shown as a function of the external magnetic fields.The ground state energy is set to zero for each value of B.

The lowest-energy multiplets in this spectrum are twofold degenerate, as expected from the model.

3.1 NMR as a probe of relaxation dynamics

In order to study the relaxation dynamics, ^1H pulsed NMR experiments have been performed on powdered samples of Cr_9 by means of a HyReSpect NMR-

spectrometer [64] as a function of the temperature for different applied magnetic fields. The interpretation of these data has allowed us to estimate the spin-phonon coupling strength and to study the decay of the molecular magnetization (see paragraph 1.3). The $1/T_1$ relaxation rate has been determined by monitoring the recovery of the longitudinal nuclear magnetization after the full irradiation of the nuclear absorption line, by using a comb of radiofrequency pulses followed by a $\pi/2-\pi/2$ solid-echo sequence. The results of these measurements are reported in figure 3.1.1. The temperature-dependence of the spin-lattice relaxation rate $1/T_1$ is shown in figure 3.1.1, normalized to χT, which is proportional to the size of equilibrium fluctuations. $(1/T_1)/(\chi T)$ displays a peak at 10 K when B = 0.55 T, and its maximum shifts to higher temperature as far as the external field is increased.

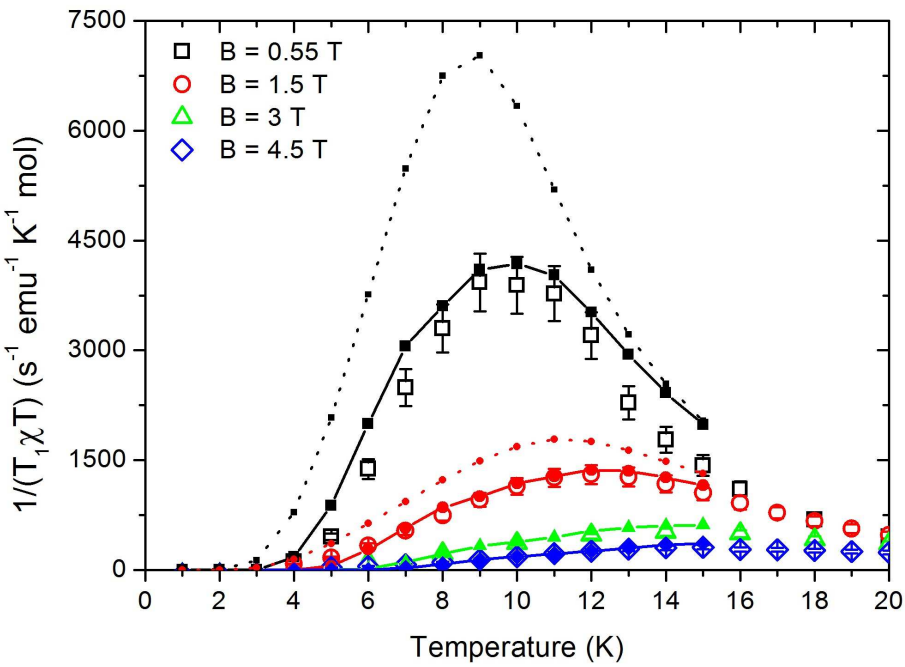

Figure 3.1.1: $\frac{1}{T_1\chi T}$ experimental (open symbols) and calculated (filled marks) data as a function of the temperature for different applied magnetic fields. Calculations are made exploiting equation 2.1.6 and taking into account the wipeout effect.

As one can evince from Figure 3.1.2, the maximum of $\frac{1}{T_1\chi T}$ deviates from the Bloembergen-Purcell-Pound (BPP) behavior , *i.e.* the height of the peaks does not

scale exactly as 1/B, differently from what observed in the even-numbered homometallic ring Cr_8, where the spin dynamics is characterized by a single dominating relaxation rate λ_0 and the BPP model perfectly describes the data. [48].

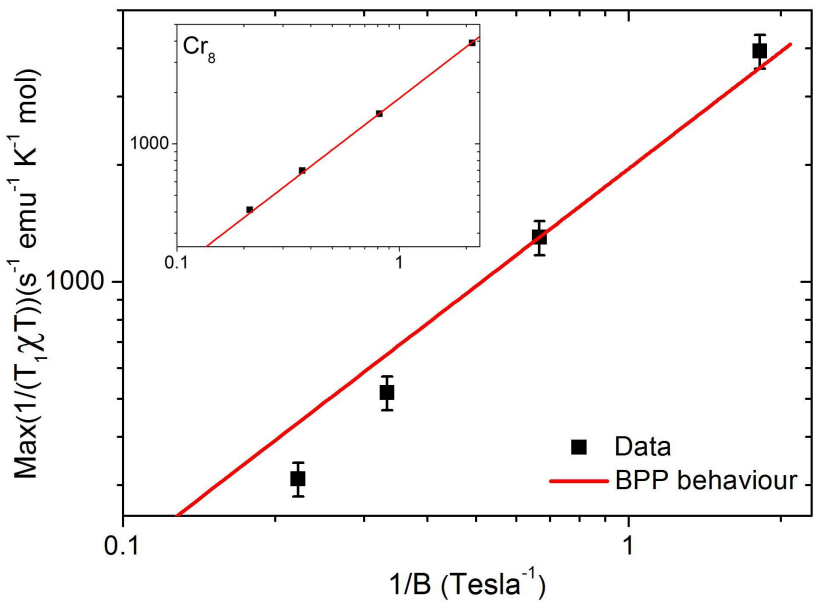

Figure 3.1.2: Maximum of the $\frac{1}{T_1\chi T}$ peaks compared with the BPP behaviour (here calculated for B=1.55 T) in log-log scale, A deviation from the BPP model is evident for Cr_9. The inset figure shows the BPP behaviour of Cr_8.

This deviation from the BPP model suggests that the Cr_9 has more than one relevant relaxation frequency in the temperature range where $\frac{1}{T_1\chi T}$ displays a peak, even if it's homometallic. In order to analyze the experimental data, the Redfield theory of relaxation process has been applied [58][56]. The origin of the peak in the temperature-dependence of $(1/T_1)/(\chi T)$ can be understood by using equation 1.3.3 to rewrite the Fourier transforms of the correlation functions at the Larmor frequency $S_{s_i^q s_j^{q'}}(\pm\omega_L)$ of equation 2.1.6. In the case of homometallic AF rings, only a single lorentzian dominates the sum in equation 1.3.3 [46, 88] and $(1/T_1)/(\chi T)$ displays a peak at the temperature at which the relaxation rate of this lorentzian matches ω_L. Indeed, for each eigenstate $|t\rangle$, $\langle t|s_i^p|t\rangle = \langle t|s_j^p|t\rangle = \frac{1}{N}\langle t|S_p|t\rangle$, where $S_P = \sum_i s_i^p$ is the p component of the total spin operator. If the relaxation dynamics is not mono-lorentzian but the different relevant rates are close to one another when they approach ω_L, we have again a

single-peak in the $(1/T_1)/(\chi T)$ [89, 60]. Cr_9 NMR data point to this second case. dExperimental data are interpreted within the theoretical framework illustrated in paragraph 1.3 and 2.1. By fitting the position of the peak in temperature, it is possible to determine the spin-phonon coupling strength γ and the value obtained for B=0.55 T is $\gamma = 4 \times 10^{-4}\, THz^{-1}$. This value well reproduces also the height and the position of the $1/(T_1\chi T)$ peaks for other values of magnetic fields. Thus, we obtain a good overall quantitative agreement between data and calculations. Furthermore, the value of found for Cr_9 is similar to that of other related AF ring like Cr_7Ni and Cr_8 ($\gamma = 2.8 \times 10^{-4}\, THz^{-1}$ [89]).

As previously discussed in paragraph 2.1, the NMR signal measurements are affected by wipeout effect, *i.e.* the signal loss due to the enhancement of the protons' transverse relaxation rate $(1/T_2)$ over the limit imposed by the experimental setup, corresponding to $10-15\,\mu s$. Thus, to calculate the spin-lattice relaxation rate of Cr_9 we take into account also the wipeout effect. For each hydrogen we calculate $1/T_1$ and $1/T_2$ as a function of the temperature, the orientation and the modulus of the applied magnetic field with 2.1.6 and 2.1.7. Then we retain only the hydrogen nuclei whose transverse relaxation rate is lower than the above-mentioned thresold. In order to obtain the $(1/T_1)/(\chi T)$ curves of Cr_9in fig. 3.1.1, we set $1/T_2^{thresh}$ = 81.7 ms^{-1} , corresponding to T_2^{thresh} = 12.2 μs (Note that the experimental threshold is $10-15\,\mu s$). Furthermore, the comparison between experimental data and calculations of $(1/T_1)/(\chi T)$ performed retaining all the protons in the molecule (dashed line&scatter in Fig.3.1.1) shows the extent of the signal loss due to the wipeout effect, which is, as expected stronger at low fields. Thus, we can conclude that the wipeout effect is a crucial ingredient in the interpretation of $^1H-$NMR experimental data. Experimentally, the measurement of the transverse nuclear magnetization ($M_{xy}^H(t)$) has been carried out by using a $\pi/2-\pi/2$ solid-echo sequence and the absolute value of the NMR signal has been extrapolated by the echo amplitude of the decay curve at zero time. The $M_{xy}^H(0)T$ is proportional to the number of protons resonating at the irradiation frequency. Transverse nuclear magnetization measurements as a function of temperature have been performed at B = 0.55 T since wipeout is generally stronger at small fields. The latter is displayed in figure 3.1.3 and compared with the theoretical model of equation 3.0.1 by taking into account equation 2.1.7. As expected, the number of detected

protons clearly decreases by decreasing the temperature [63]. Furthermore, calculations well reproduce the wipeout effect, thus confirming the reliability of the model.

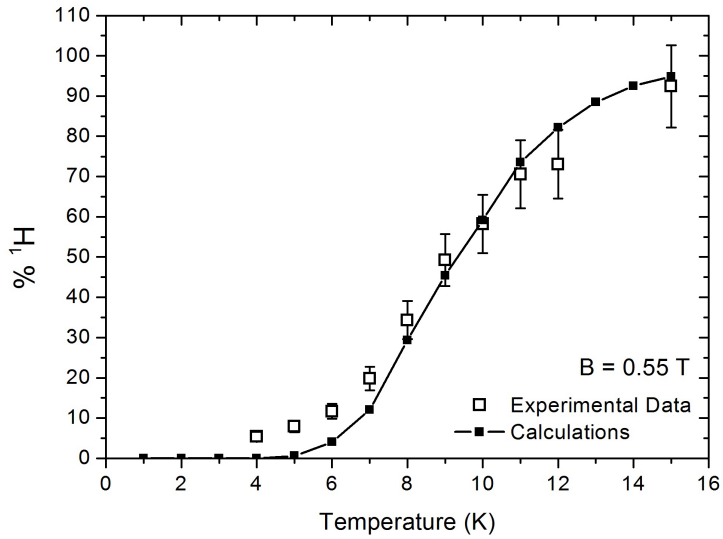

Figure 3.1.3: The fraction of protons probed by NMR (open squares), obtained as described in the text, is compared with the theoretical prediction (filled squares and line).

Altough the wipeout effect is commonly observed as a function of the temperature, a field dependent measurements would allow to detect the position of the level crossing. In fact, at the levels crossings of both $1/T_1$ and $1/T_2$ rates increase, due to the inelastic contributions to the relaxations dynamics, leading to a strong wipeout effect. This effect in the proximity of the level crossing was observed for the first time in the Cr_8Zn molecular nanomagnet [50]. We have therefore measured $M^H_{xy}(0)T$ as a function of the applied magnetic field at T = 8 K, in order to populate the lowest excited levels involved in the crossing.

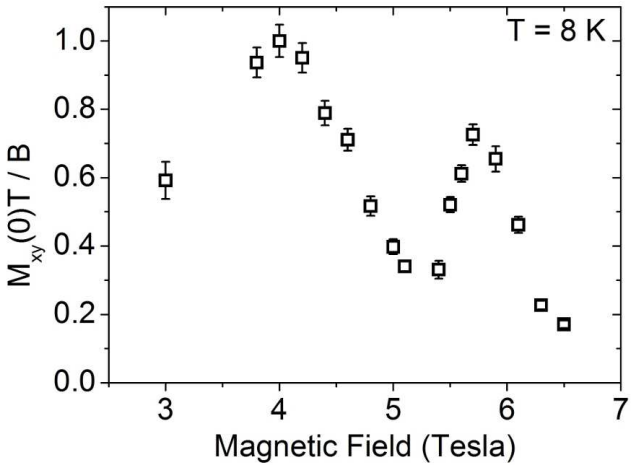

Figure 3.1.4: Renormalized transverse nuclear magnetization $\left(\frac{M^H_{xy}(0)T}{B}\right)$ of Cr_9 as a function of the applied magnetic field B at T = 8 K. Data have been also renormalized so that the maximum value of the magnetization in the explored magnetic fields range is set to 1.

The experimental sequence for the measurements is the same described for the wipeout as a function of the temperature, with the exception that, in the present case, one has to ensure that the line is fully irradiated. The analysis of the data is different. The $M^H_{xy}(0)$ is divided by the applied magnetic field in order to eliminate the effect of the Boltzmann population of the nuclear Zeeman levels. The energy levels scheme as a function of the magnetic field is reported in the fig.3.0.3, showing a level crossing between the first and the second excited levels at 5.4 T. The transverse nuclear magnetization, shown in figure 3.1.4, displays a minimum between 5 and 5.5 T, indicating a strong wipeout effect and confirming the position of the level crossing field.

3.2 Study of the relaxation dynamics of Cr_9 ring

The unique free parameter of the microscopic model describing the relaxation dynamic of MNMs is the spin-phonon coupling strength (γ), see 1.3.2, and it has been determined from the analysis of NMR data. This parameter allows to study the relaxation dynamics of the cluster by analyzing the spectrum of fluctuations

of the cluster magnetization given by [90]:

$$S_{M,M}(\omega,T,B) = \sum_{i=1,n} A(\lambda_i,T,B)\frac{\lambda_i(T,B)}{\lambda_i^2(T,B)+\omega^2} \tag{3.2.1}$$

The calculated weights A(T,B;λ_i) relative to the characteristic relaxation rates (λ_i) of the autocorrelation of the magnetization (eq 3.2.1) are shown in figure 3.2.1 as a function of the inverse temperature for three values of the applied magnetic.

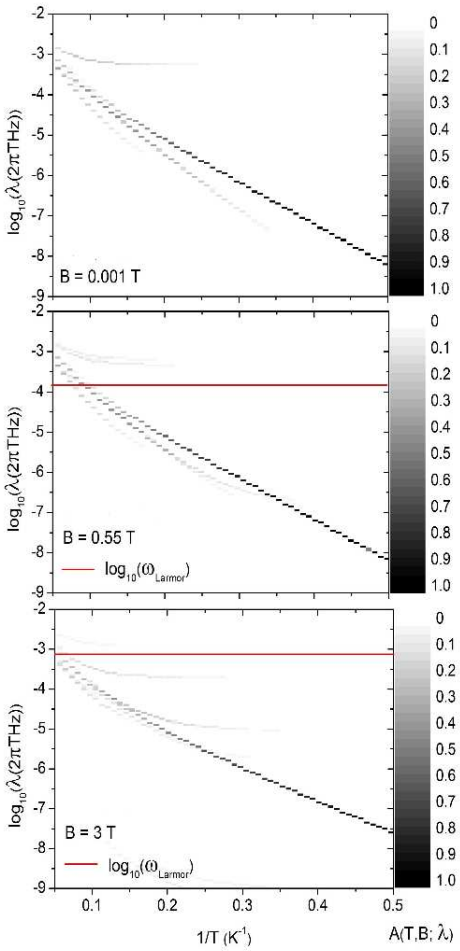

Figure 3.2.1: Intensity plots maps showing the calculated weights A(T,B;λ_i) of the magnetization autocorrelation versus 1/T for B=0.001, 0.55 and 3 T respectively. The red line represents the proton Larmor frequency (ω_L). The weigths ($A(T,B;\lambda_i)$) have been normalized by χT, for each value of temperature in the spectra, which is proportional to the size of the equilibrium fluctuations.

When the relaxation rates λ_i intersect the Larmor frequency ω_L (red line), $1/T_1$ displays a peak. It is worth to stress that γ merely fixes the relaxation timescale (a variation of γ produces a rigid vertical shifts in figure 3.2.1). In the temperature range of $10K \lesssim T \lesssim 15K$, where the peak of $1/T_1$ is observed, the dynamics is described by several rates with an appreciable weights but very close in frequency to one another. This fact explains why a single peak in the $(1/T1)/(\chi T)(T)$ is observed in spite of a multi-time relaxation dynamics. Only below $T \simeq 3K$ there is a single relaxation process, whose T-dependence follows the Arrhenius law. The analysis of the eigenvectors and of the matrix elements of the rate matrix **W** allow to understand the dominant relaxation processes. For T< 3 K and at low field the levels involved in the process are the two degenerate $S = 1/2$ ground doublets and the second excited $S = 3/2$ multiplets with E = 23.7 K (blue arrows in figure 3.2.2).This corresponds to an Orbach's process following the Arrhenius law with an energy barrier around $\Delta/k_B \backsimeq 24K$ [2.3.4], which is the dominant one up to $T \cong 7K$.

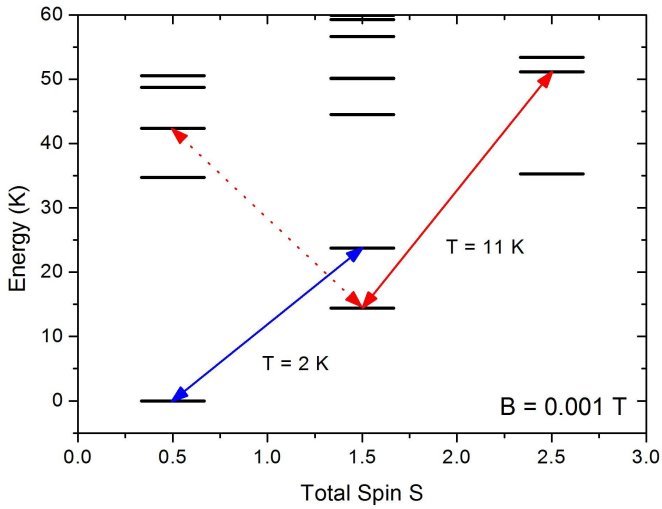

Figure 3.2.2: Relaxation paths corresponding to the dominant relaxation rates λ_i of Cr_9 for $B \to 0$ in the low-temperature regime (T= 2 K, blue arrows) and at T = 11 K (red arrows).

At about $T = 3K$, a second rate becomes relevant in the relaxation dynamics, corresponding to a process from the two degenerate first excited multiplets with S = 3/2 and E = 14.4 K towards higher excited levels with S = 1/2 and S = 5/2. At

temperatures close to the $1/T_1$ peak, these processes become the dominant ones (red arrows in figure 3.2.2). The presence of an applied magnetic field leads to a faster relaxation, especially at low T. The dynamics still have a multiple-times character above 3 K and the relevant relaxation paths always involve the same total-spin multiplets, even if split by the Zeeman interaction.

By comparing the relaxation dynamics of Cr_9 and with that of the even-membered parent compund Cr_8 [48], is found that both clusters are characterized by one single dominating Arrhenius process at low temperature, although in Cr_9 other relaxation processes emerge at significantly lower temperatures . In addition, the present model is characterized by the twofold degeneracy of the relevant relaxation rates $\lambda_i(T)$ in Cr_9, which reflects the symmetry of Eqs. 3.0.1, 1.3.2. These degeneracies are in fact a peculiar characteristic of highly symmetrical frustrated MNMs [87, 60]. These degeneracies are in fact a peculiar characteristic of highly symmetrical frustrated MNMs and can be lifted by reducing the symmetry of the molecule. For instance, by assuming that single Cr-Cr bond is different from the others and thus introducing a different exchange coupling $J' = 1.1J$ for this bond, the cluster is still characterized by competing AF interactions, although the degeneracy of the energy levels is removed.

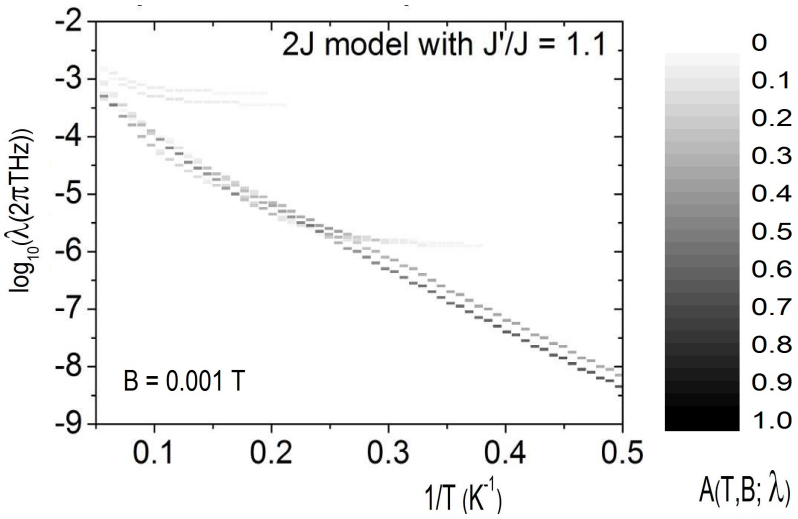

Figure 3.2.3: Intensity plot maps showing the calculated weights A(T,B;λ_i) of the magnetization autocorrelation versus 1/T for B=0.001 T. The plot maps ($A(T,B;\lambda_i)$), have been normalized by χT, for each value of temperature in the spectra, which is proportional to the size of the equilibrium fluctuations.

In this case the relaxation dynamics is dominated by two distinct rates even at low temperature (see figure 3.2.3) showing the typical behavior of a cluster with competing AF interactions. A lifting of these degeneracies can be obtained also by assuming a less-symmetric form of the magneto-elastic coupling. Such a coupling can also lead to sizeable transition-probabilities between the ground manifold and the lowest-energy S = 3/2 multiplets, leading to a faster relaxation at very low temperatures. The degeneracy between the two S = 1/2 ground multiplets and the corresponding perfect frustration is expected to be slightly broken at low temperature due to the Jahn-Teller theorem.
A very interesting experiment would be to exploit high-resolution four-dimensional inelastic neutron scattering to study the low-energy peak corresponding to the transition between the two nearly degenerate S = 1/2 multiplets [91]. The dependence of the intensity of this peak over the momentum transfer vector would yield direct information on how the frustration is removed and on the associated low-frequency quantum dynamics.

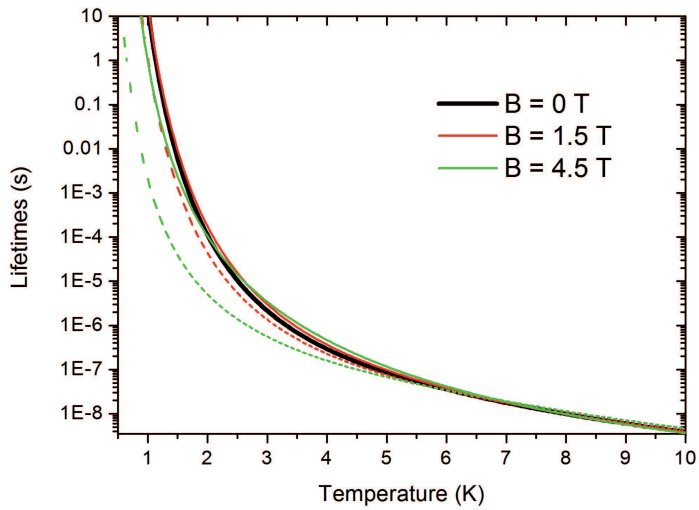

Figure 3.2.4: Calculated temperature-dependence of the lifetime of the levels of the two S = 1/2 ground doublets for several values of the applied magnetic field. Continuous and dashed lines correspond to $|S = 1/2, M = -1/2>$ and $|S = 1/2, M = 1/2>$, respectively.

The spin dynamics associated to this low-energy peak will be damped on a time-scale depending on the average of the lifetimes of the involved levels. The

here-determined model of the magnetic relaxation of Cr_9 are used to calculate the effect of spin-phonon interaction on the lifetimes of the lowest-energy levels. The calculated temperature-dependence of the lifetime of the ground S = 1/2 manifold for several values of the magnetic field are shown in figure 3.2.4. At low temperature the lifetime is very long and can be also controlled by applying an external magnetic fields, making the previously mentioned experiment very promising if large high-quality crystals become available. It is worth to add that direct transitions between the two S = 1/2 doublets should not strongly limit the lifetimes, because of the small phonon density associated with a very small energy gap.

3.3 Spin dynamics in AF even open/closed rings

As representative of molecules belonging to the family of even rings, the open Cr_8Zn is compared with the closed Cr_8 ring[51]. In figure 3.3.1 the relaxation rates ($\frac{1}{T_1\chi T}$) of the open Cr_8Zn and closed ring Cr_8 are reported as a function of the temperature for two different external magnetic fields. Two peaks have been observed in the $\frac{1}{T_1\chi T}$ in both systems: one at $10K \lesssim T \lesssim 15K$ and the second below 4 K. In particular, the latter is well resolved only for Cr_8Zn, while the the main peak is well defined and could be fitted by a single relaxation rate. The low-T peak is attributed to another correlation frequency of the magnetization, thus the $\frac{1}{T_1\chi T}$ curves can be fitted by:

$$\frac{1}{T_1\chi T} = A\left[\frac{\lambda_1(T,B)}{\lambda_1^2(T,B)+\omega_L^2} + \frac{\lambda_2(T,B)}{\lambda_2^2(T,B)+\omega_L^2}\right] \tag{3.3.1}$$

where A is proportional to the average square of the dipolar interaction between the protons and the magnetic ions, $\lambda_{1,2}$ are the two correlation frequencies in the spectrum of fluctuations of the cluster magnetization, and ω_L is the proton Larmor frequency.

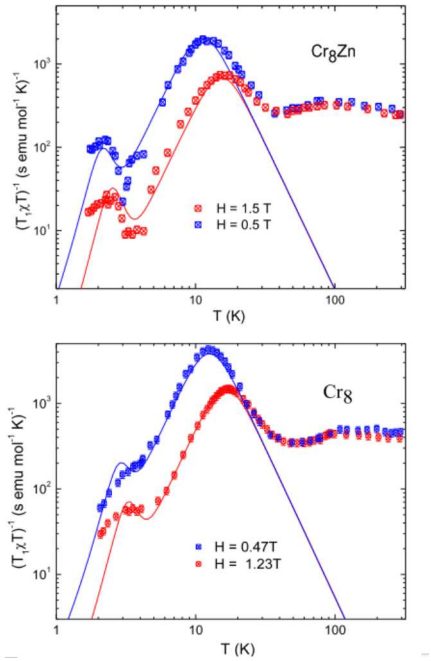

Figure 3.3.1: Cr_8Zn and Cr_8 $\frac{1}{T_1\chi T}$ are reported as a function of the temperature in log-scale (in order to highlight the low temperature peaks), for different applied fields. [51]

The data have been fitted according to equation 3.3.1. The correlation frequency is is assumed to have a power law dependence, $\omega_c(T) = CT^{\alpha}$ as found in most molecular rings and clusters [66].

	$C_1\,(rad\,s^{-1})$	α_1	$C_2(rad\,s^{-1})$	α_2
Cr_8Zn	2.8×10^4	3.5	60×10^4	7
Cr_8	1.8×10^4	3.5	8×10^4	7

Table 3.1: The values of the parameters obtained from the best fit for $1/T_1\chi T$ data for the Cr_8Zn 'open' and Cr_8 'closed' rings

The much larger value of the temperature exponent ($\alpha_2 = 7$) for the secondary correlation frequency indicates a different relaxation mechanism of the magnetization possibly related to Raman spin-phonon processes [92]. The difference could be related to the much smaller gap, from the non-magnetic ground states and the first excited magnetic states observed in Cr_8Zn with respect to Cr_8.

Chapter 4

Breaking of the ring: The case of Cr_8Cd

The magnetically-open AF rings like Cr_8Cd [53] are model systems for the study of the microscopic magnetic behaviour of finite AF Heisenberg chains [93]. In this type of systems the magnetic behaviour depends length and on the parity of the chain (odd or even)[94, 95]. Traditionally the experimental study of finite chain effects has involved a top–down approach [96], where an ideal infinite chain of magnetic atoms was "cut" by introducing diamagnetic impurities. This produces an ensemble of chains with different lengths and different parities. However, the advances in building short chains of atoms using the capabilities of scanning tunnelling microscope tips to perform atom-by-atom manipulations has opened the possibility of creating more controlled short chain systems [97, 98]. An alternative and promising option is provided by AF rings, thanks to high degree of control which has been achieved in the chemistry of magnetic molecules. In addition heterometallic rings have been proposed as possible candidates for the implementation of qubits for quantum computation. Thus, it is very important to know the local spin configuration, in order to be able to control and manipulate the magnetic state.[6, 27, 28]. The Cr_8Cd open ring has already been studied by polarized neutron diffraction [17]. It was found that the arrangment of the magnetic moments is non collinear (NC), *i.e.* if we consider a classical spin configuration, the z-component of the magnetic moment (μ_i) for the sites closer to the edges of the

chain is much larger than in the middle of the chain. The competition between the Zeeman and the exchange interactions originates the NC spin structure, as depicted in Figure 4.0.1 within a classical spin model:

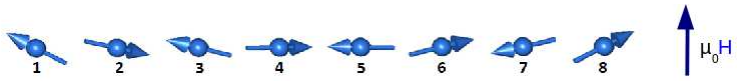

Figure 4.0.1: The Cr_8Cd chain in an external magnetic field shows a non collinear spin structure in the classical spin ground state configuration. In order to obtain this configuration, a classical spin Hamiltonian have been considered, with only first-neighbours exchange interactions. [99][17]

The same type of information can be extracted by means of local probes, for instance, by performing NMR experiments on ^{53}Cr nuclei, as already demonstrated in previous works. [29, 100]. Thus, we have measured ^{53}Cr-NMR spectra on Cr_8Cd, in order to study local spin densities on the Cr sites in an open-even ring. The molecule, reported in top-figure 4.0.2, is indeed a parent compound of Cr_8, where the introduction of the Cd^{2+} non-magnetic impurity breaks the cyclic symmetry with an open boundary condition, leading to an effective model system for an open-even chain. Each molecule can be described by the following Hamiltonian:

$$H_e = \mathrm{J}\sum_{\mathrm{i}=1}^{7} \mathrm{s_i}\cdot\mathrm{s_{i+1}} + \sum_{\mathrm{i}=1}^{8} \mathrm{d_i s_{i,z}^2} + \mu_\mathrm{B}\mathrm{g}\sum_{\mathrm{i}=1}^{8} \mathrm{s_i}\cdot\mathrm{H}, \tag{4.0.1}$$

where the first term is the nearest-neighbours isotropic Heisenberg exchange interaction, s_i is the spin operator for the i-th ion in the molecule. The second term describes a small uniaxial single-ion anisotropy. The last term represents the Zeeman coupling to an external magnetic field. INS measurements on the parent Cr_8Zn compound and magnetization measurements on Cr_8Cd yield J =1.32 meV, d = -0.036 meV and g=1.98 [16, 18, 17]. The crystals of Cr_8Cd are characterized by two molecules per unit cell (bottom figure 4.0.2). For this reason the external magnetic field has been applied with an angle of $\theta = 27°$ with respect to the c-axis of molecules , *i.e.* the axis perpendicular to the plane of the ring, and parallel to the b-axis of the unit cell. This experimental configuration has been choosen in order to induce equal components of the magnetic field along the c-axis of both molecules in the unit cell.

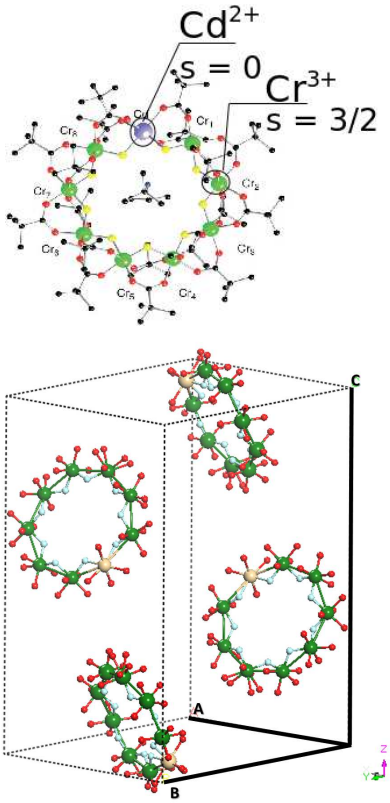

Figure 4.0.2: Top: The Cr_8Cd molecule, Cr atoms are represented in green, Cd in purple, O in red, F in yellow and C in black. Hydrogen ions are omitted for clarity. Bottom: two inequivalent molecules are clearly distinguable within the unit cell.

Figure 4.0.3 shows the calculated energy level scheme of the Hamiltonian 4.0.1 as a function of the external magnetic field for $\theta = 27°$. This value guarantees the same orientation of the two inequivalent molecules of the crystalline structure in the field. A level-crossing (LC) is found at 2.6 T and an anti-LC at 4.8 T between excited states.

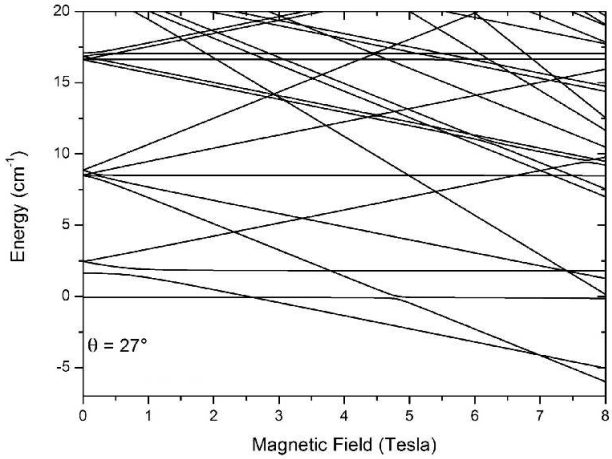

Figure 4.0.3: Energy level scheme of Cr_8Cd as a function of the external magnetic field calculated for θ=27°.

The major difficulty of ^{53}Cr-NMR measurements is due to the low natural abundance and the low sensitivity of the probe, as one can evince from the table 4.1.

	nat. ab.	I	γ/2π (MHz/T)	Receptivity (rel. to ^{1}H=1)
^{53}Cr	0.095	3/2	2.606	0.0000863

Table 4.1: NMR Properties of ^{53}Cr.

A Hahn-echo ($\pi/2-\pi$) sequence was employed. Intensity was collected point by point as a function of both field and frequency was collected by integrating the whole spin echo over time. The NMR spectra of Cr_8Cd were collected by two complementary methods: by varying the frequency at a fixed external magnetic field, or by measuring the intensity at field in small steps at fixed frequency. A complex pattern of resonance frequencies in the 15-30 MHz range was observed. The results of these measurements are shown in figure 4.0.4.

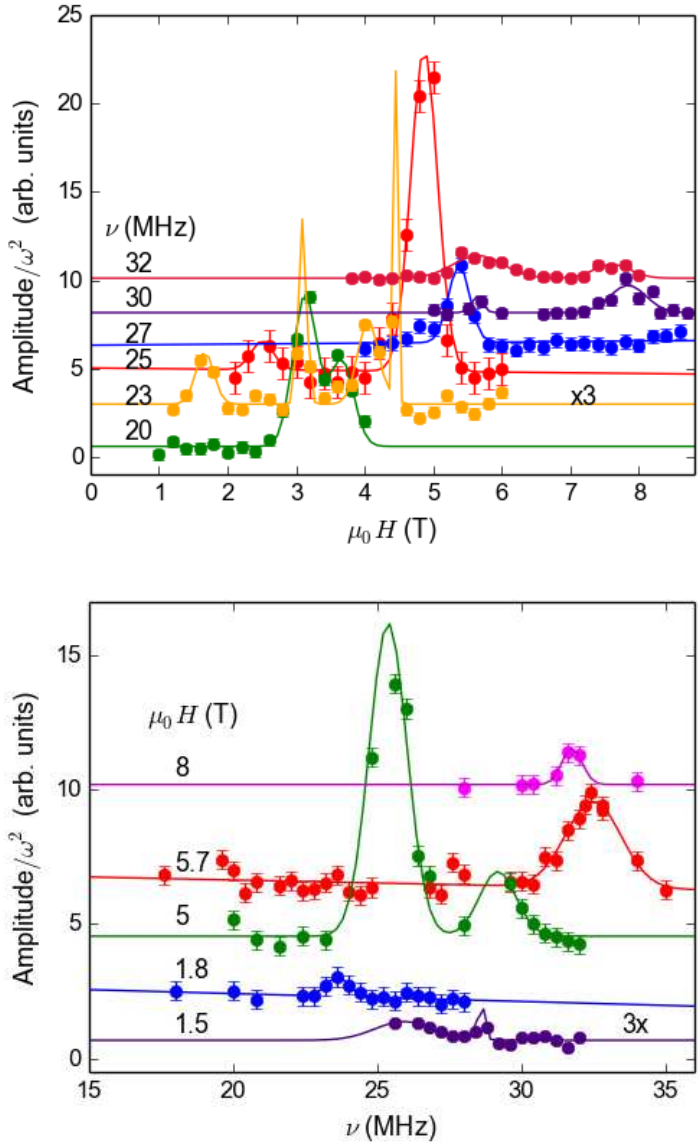

Figure 4.0.4: ^{53}Cr-NMR spectra of Cr_8Cd at T =1.4 K obtained by sweeping the magnetic field at a constant frequency (upper figure) and by sweeping the frequency at a constant magnetic field (lower figure). Data have been fit according to a gaussian profile.

The spectra have been fit with one or two gaussians component and the extracted frequencies vs fields are compared with the theoretical calculation. The results are shown in the figure 4.0.7.

The ^{53}Cr-NMR frequency can be calculated as the vector sum of the external magnetic field H and the internal field due to the hyperfine interaction:

$$\nu_{i,j} = \frac{\gamma_{Cr}}{2\pi} - gA[(\langle j|s_{i,z}|j\rangle cos\theta + H_z)\hat{z} + (\langle j|s_{i,x}|j\rangle sin\theta + H_x)\hat{x}] \qquad (4.0.2)$$

where γ_{Cr} is the ^{53}Cr nuclear gyromagnetic ratio, g is the Cr^{3+} Landè factor, $< s_i >$ is the local expectation value of the Cr^{3+} electronic moment, j is the populated magnetic level and A isotropic core polarization hyperfine contact term. All the theoretical calculations take into account a small error in the positioning of the sample of $\Delta\theta = 2°$, so the theoretical spin moment and the frequencies were calculated for $\theta = (27 \pm 2)°$ because of the presence of the two non-equivalently oriented molecules

The difference between the configurations is very small, but the introduction of this small error has helped to improve the fit of NMR spectra. All the theoretical results are thus averaged over these two orientations. Due to Cr_8Cd symmetry properties, it is possible to indentify four pair of equivalent Cr^{3+} sites, as reported in figure 4.0.5.

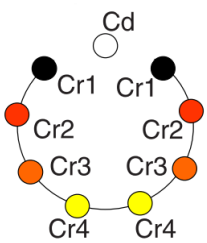

Figure 4.0.5: Four pair of chromium can be identified in the ring (i=1,...,4).

The calculated local spin moments for the four pair of Cr^{3+} are reported in figure 4.0.6. At the extremities of the chain, $Cr_1 - Cr_8$ spins are more energetically favoured to align along the magnetic field as they have to compete only with one exchange interaction. The AF interaction with the nearest neighbours imply that the $Cr_2 - Cr_7$ spins are aligned in the opposite direction. In the middle of the chain for the $Cr_4 - Cr_5$ spins, the 'spin-up'- 'spin-down' condition can no longer be satisfied as these two spins cannot simultaneously satisfy the AF condition between them and with their nearest neighbours. This causes frustration and as a

result the more energetically favourable ground state is a NC spin configuration (see figure 4.0.1[17]).

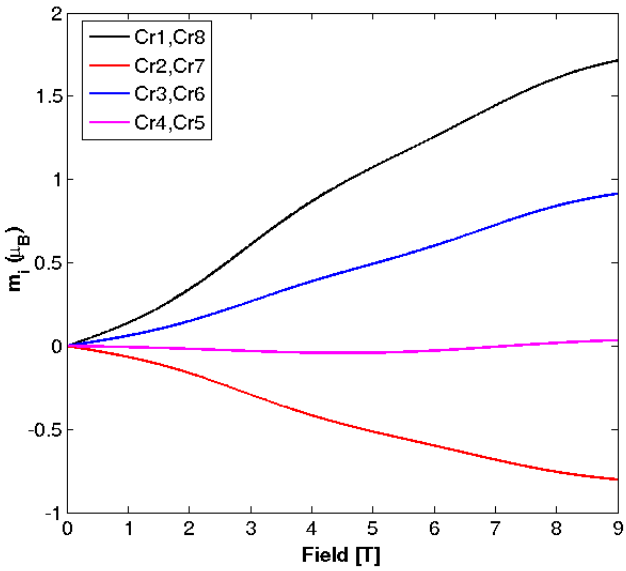

Figure 4.0.6: Calculated local spin moments as a function of the applied magnetic field for the Cr_8Cd molecular ring.

By comparing the experimental results with the calculated ^{53}Cr-NMR frequencies it is possible to determine the only free parameter of the model, the contact term A (see eq.2.1). The quadrupolar effects in ^{53}Cr-NMR (I(Cr)=3/2) can be neglected, since only the central line transitions were measured and their shifts are due only to second order effects. Since the core polarization constant A depends on core electrons, we can assume the same value of A_{cp} for all the Cr sites. The intensity plot reported in the figure 4.0.7 show the calculated NMR frequencies as a function of the external magnetic field, for every populated level at 1.4K and for each of the non-equivalented Cr_i (i=1,...4). For each frequency a 1MHz wide Lorentzian function has been built up, whose amplitude depends on the thermal population of the level. The experimentally extracted ^{53}Cr-NMR frequencies are found to be in good agreement with the ones, yielding A = -12.7 $Tesla/\mu_B$.

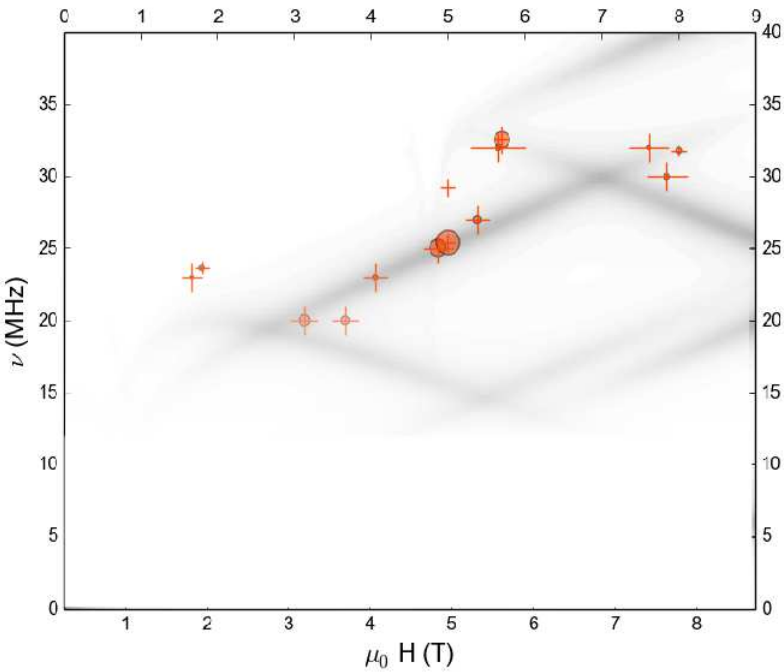

Figure 4.0.7: Intensity plot as a function of the external magnetic field vs the experimental data. The construction of the intensity plot is described in the text. Calculated frequencies are not reported because it is a range of frequencies not experimentally accesible.

The result, A found is comparable with the results found for other rings [100, 29].

	A (T/μ_B)
Cr_8Cd	-12.7
Cr_7Cd	-12.38 [29]
Cr_7Ni	-11 [100]

Table 4.2: Comparison of core polarization constant for three different rings.

The next step was to attribute the signal to the corresponding pair of ^{53}Cr nuclei in the ring. Figure 4.0.8 shows the calculated frequencies for the $Cr_1 - Cr_8$ and $Cr_2 - Cr_7$ pairs, compared with the experimental data. It is evident that the signal observed can be totally ascribed to these two pairs of Cr sites.

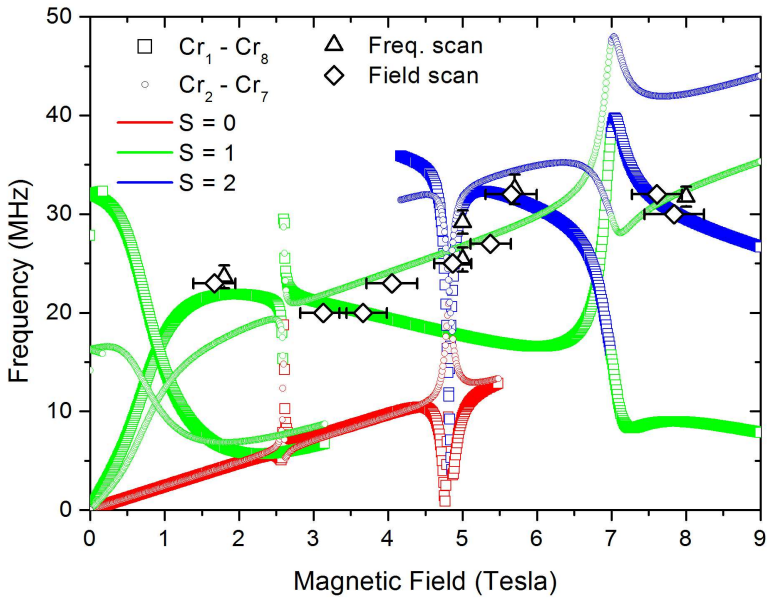

Figure 4.0.8: Calculated frequency and experimental data as a function of the external field. Only the frequency of $Cr_1 - Cr_8$ and $Cr_2 - Cr_7$ pair are reported. the different colors identify the total-spin S value of the populated levels involved in the calculations.

Due to their higher magnetic moment values, the periferics Cr ions $Cr_1 - Cr_8$ and $Cr_2 - Cr_7$ (as reported in figure 4.0.6), are the only ^{53}Cr nuclei that can be detected. In fact, the pairs of Cr ions localized in the middle of the chain $Cr_4 - Cr_5$ and $Cr_3 - Cr_6$, were not observed in the spectra due to the small value of their magnetic moments and thus to the small values of the corresponding frequencies, below the experimental limit of 15 MHz. Figure 4.0.9 shows the comparison between the experimental data and the theoretical calculation for the $Cr_4 - Cr_5$ and $Cr_3 - Cr_6$ pairs.

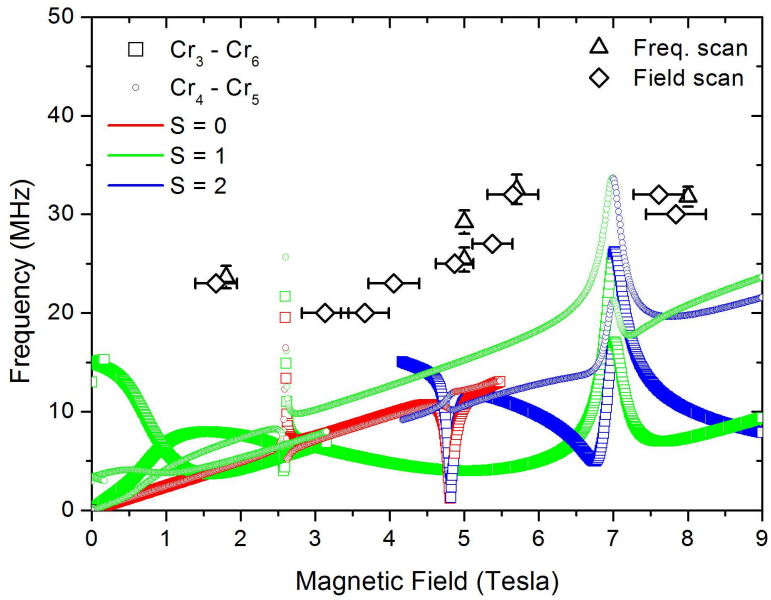

Figure 4.0.9: Calculated frequency and experimental data as a function of the external field. Only the frequency of $Cr_3 - Cr_6$ and $Cr_4 - Cr_5$ pair are reported, the different colors identify the total-spin S value of the populated levels involved in the calculations.

NMR investigations on the Cr_7Cd molecular ring showed that Cr^{3+} magnetic moments at the different sites are found to be staggered but have a nearly uniform and large value across the ring [29]. This is indicative of the fact that for an odd chain of magnetic ions (see figure 4.0.10) the spin arrangement is collinear in the ground state as opposed to the NC one for the even-numbered Cr_8Cd chain. This is also consistent with the fact that, for an odd number of ions subject to the effect of an external magnetic field, it is possible to simultaneously satisfy all the AF spin up-down arrangements, thus removing the frustration, unlike the case of the Cr_8Cd molecule.

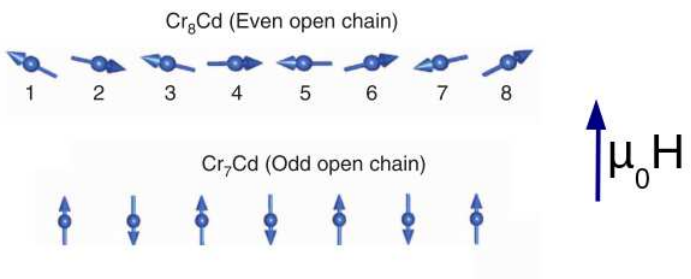

Figure 4.0.10: Comparison between the classical spin ground state configuration for Cr_8Cd and Cr_7Cd. [17]

In conclusion the quantitative experimental result confirm the theoretical predictions for the non-collinear spin arrangement in finite AF-coupled magnetic ions chains and the comparison between Cr_8Cd and Cr_7Cd shown how the parity of the chain and the boundary condition have an effect on the spin structure.

Chapter 5

Study of a six-membered *Dy* ring

$[Dy(H_{tea})(NO_3)]_6 \cdot 8MeOH$, in short Dy_6, is the first rare-earth based ring that has been ever synthesized [54]. A staggered magnetization was observed in low field at 1.3 K. Indeed, if the applied magnetic field is lower than 0.4 T, this molecule behaves as a non-magnetic system. The study of the static magnetic properties of Dy_6 has been performed by means of proton Nuclear Magnetic Resonance (^{1}H-NMR) and DC/AC-SQuID magnetometry.

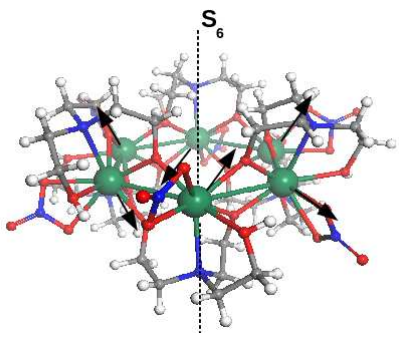

Figure 5.0.1: Molecular structure of Dy_6. green: Dy, red: O, blue:N, white:H, dotted line: S_6simmetry axis, black arrows: local magnetic moments in the ground doublet state.

5.1 Investigation of the static magnetism

The system can be described by a non-collinear Ising model [20]:

$$\hat{H} = \sum_{i=1}^{6} J^{exch} \tilde{s}_{i,z} \tilde{s}_{(i+1),z} + \sum_{i=1}^{6} \sum_{j>i}^{6} J^{dipolar} \tilde{s}_{i,z} \tilde{s}_{j,z} + \mu_B g \sum_{i=1}^{6} B \cdot \tilde{s}_{i,z} \tag{5.1.1}$$

where the operators $\tilde{s}_{j,z}$ are the projection of a pseudo-spin ½ along the local Ising axis [101], characterizing the ground Kramers doublet of each Dy ion. J^{exch} is the exchange coupling between the nearest Dy sites and $J^{dipolar}$ is the dipolar magnetic exchange between the centers i and j. The dipolar coefficients $J^{dipolar}$ have been evaluated within the point-dipole approximation, taking as input ions coordinates, in agreement with the *ab-initio* calculation by Ungur *et al.*[20].

nearest neighbor	next-nearest neighbor	opposite
4.343 cm^{-1}	0.028 cm^{-1}	0.403cm^{-1}

Table 5.1: Calculated Constants of the Dipolar Interaction between the Ground Kramers Doublets of Different Magnetic Centers in Dy_6.

The system is shown in the Figure 5.0.1 and has S_6 symmetry. Toroidal arrangement of local magnetic moments has been found recently in lanthanide-based systems and it was first discovered in Dy_3 triangles[102, 103]. Ungur *et al.* have studied the electronic and magnetic structure of Dy_6 through *ab-initio* calculation [20], they found a toroidal magnetic moment in absence of a net magnetic state in zero field, due to the high symmetry of the dipolar interactions of Dy magnetic moments in the molecule.

The DC magnetic susceptibility of Dy_6 was measured in temperature in order to extract the exchange parameter J^{ex} of Equation 5.1.1 and α, the angle between the symmetry axis of the molecule S_6 and the local Ising axis. We found $J^{exch} = -0.2\,cm^{-1}$ and $\alpha = 43\,°$, confirming the value already found by Ungur at al. by ab-initio calculations [20]. DC measurements results are reported as χT in the top figure 5.1.1 with an applied field of 1kOe. χT grows by increasing the temperature, reaching a constant value above 15 K and it tends to zero by lowering the temperature, the presence of a non-magnetic ground state.

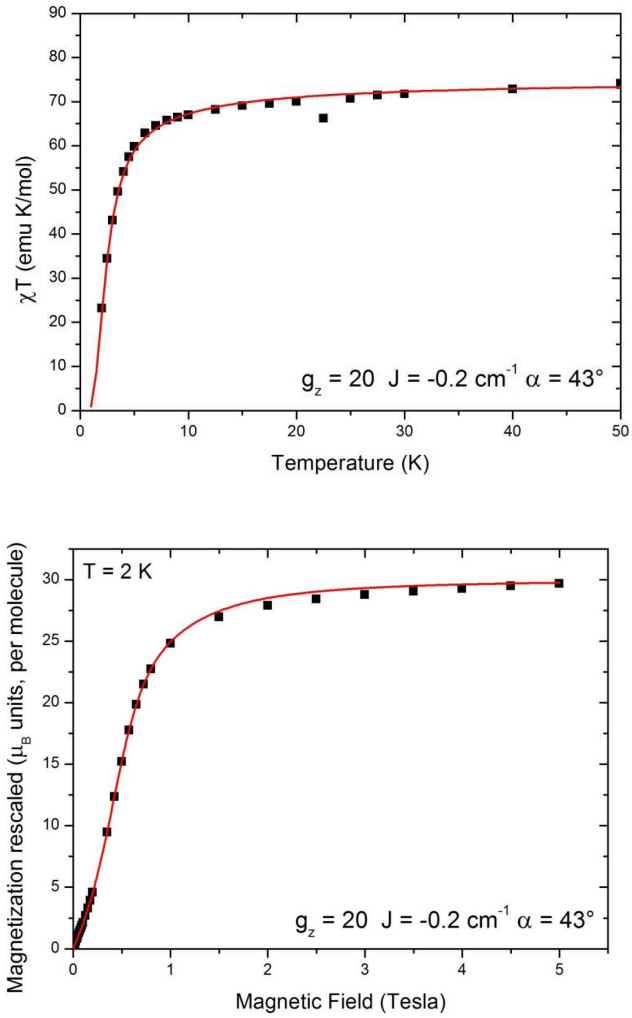

Figure 5.1.1: The temperature dependence of χT (black squares in the bottom figure) and $M(H)$ (black squares in the top figure) of Dy_6compared to the theoretical model (red line) as reported in the text with J^{ex} = -0.2cm^{-1} and $\alpha = 43°$.

The magnetization curve at T = 2 K, shown in the bottom-panel of Figure 5.1.1 saturates to a value of $30\mu_B$, in agreement with the presence of a six Ising-type Dy's ions. The energy levels diagram as a function of the applied magnetic field with $\theta = 90°$, is shown in figure 5.1.2. A LC between the ground state and the first excited levels of Dy_6 occurs at B = 0.4 T. Experimentally, the derivative of magnetization curve as a function of the applied magnetic field shows a peak at the LC field [1]. It is worth to stress that since all the measurements have been per-

formed on powdered samples, the peak in the magnetization curve derivative gives us the "spherically averaged" position of the LC. In order to reproduce the magnetization curve with our theoretical model we have performed an average over all the possible direction of the applied magnetic field, with respect to the S_6-axis of the molecule. Here we compare the magnetization derivative with the energy level diagram with the applied magnetic field in the plane of the ring ($\theta = 90°$, Figure 5.1.1), since these directions give the main contributions to the spherical average. The position of the peak of the magnetization curve derivative, and thus the LC field, is the main feature that has allowed us to refine the parameters of our theoretical model.

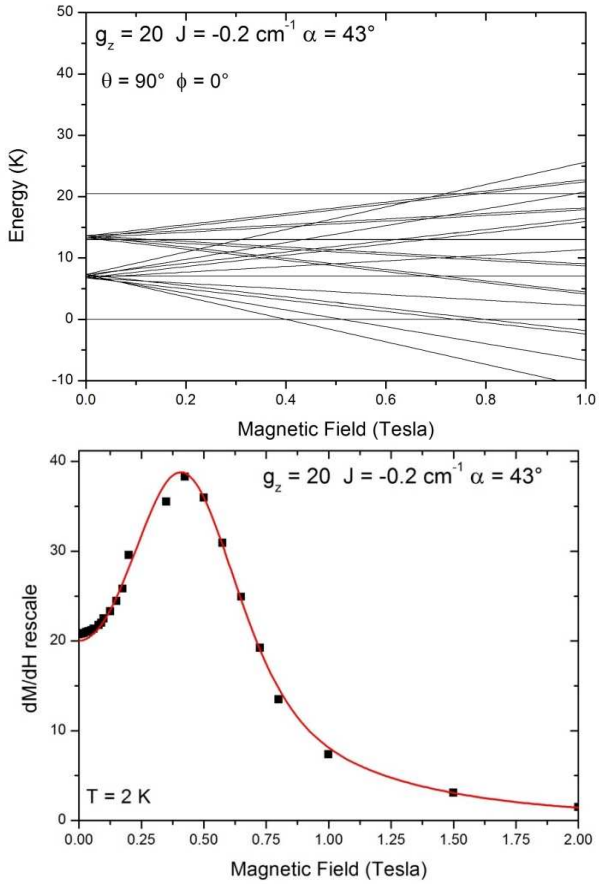

Figure 5.1.2: Top panel: Calculated energy levels scheme of Dy_6 as a function of the magnetic field applied in the plane of the ring, obtained from the Hamiltonian in Eq.5.1.1. Bottom panel: derivative of M(H) at 2 K as a function of the external magnetic field (scatter), compared with the theoretical calculations (red line).

As already demonstrated for the case of Cr_9[90] and Cr_8Zn [50] the LC fields can be obtained by measuring the transverse nuclear magnetization with a ^1H-NMR experiment. In fact a mesurement of the quantity $M_{xy}(0)T$ as a function of the applied magnetic field allows us to quantify the wipeout effect, that is particularly strong at the LC fields. Figure 5.1.3 shows the transverse nuclear magnetization as a function of the magnetic field for the Dy_6, measured at T = 1.35 K. As explained previously, the experimental sequence for the measurements is the same described for the wipe-out as a function of the temperature (see 2.1), with the exception that the analysis of the data is different. The transverse magnetization the $M^H_{xy}(0)$ is divided by the applied magnetic field in order to eliminate the effect of the Boltzmann population of the nuclear Zeeman levels.

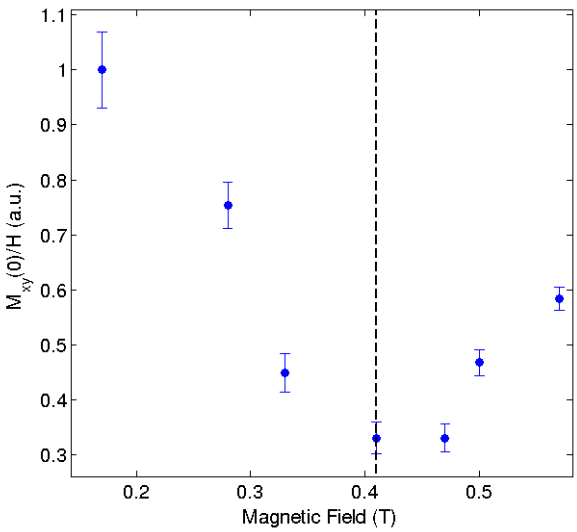

Figure 5.1.3: Renormalized transverse nuclear magnetization $\left(\frac{M^H_{xy}(0)T}{B}\right)$ of Dy_6 as a function of the applied magnetic field B at T = 1.35 K. Data have been also renormalized so that the maximum value of the magnetization in the explored magnetic fields range is set to 1.

The transverse nuclear magnetization, shown in figure 5.1.3, displays a minimum between 0.4 and 0.5 T, indicating a strong wipeout effect and confirming the position of the level crossing field around B = 0.4 T. (see top-panel infigure 5.1.2).

5.2 Study of spin dynamics

The dynamics of Dy_6 has been investigated by AC-susceptibility measurements as a function of temperature and frequency, in zero and applied field. AC SQUID magnetometry has been performed on a powdered sample of Dy_6 on a MPMS XL-5 SQUID magnetometer, in the temperature range of 2-20 K and field range of 0-1 T. For further details on the measurement see paragraph 2.3.
In figures 5.2.1 and 5.2.2 show the immaginary part of susceptibility of Dy_6 as a function of the temperature and frequency at zero-field and at B = 1, 3, 5 10 KOe.

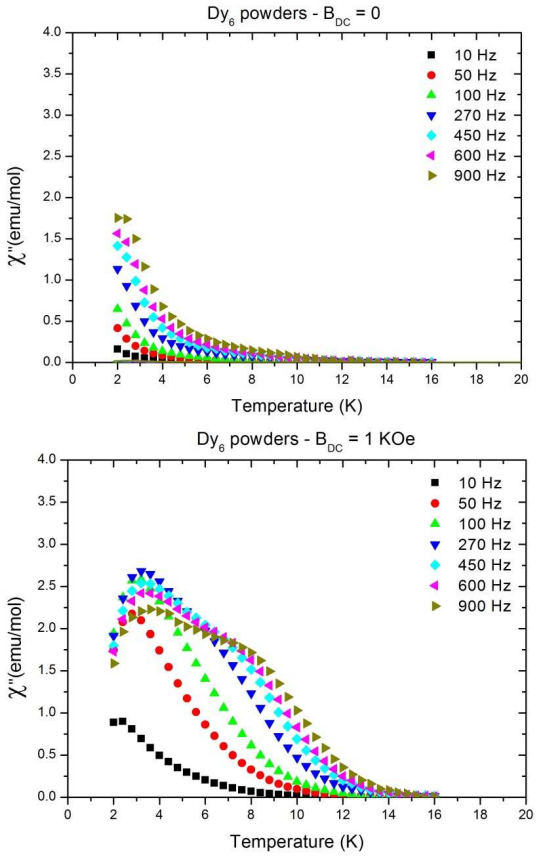

Figure 5.2.1: Immaginary part of susceptibility of Dy_6 as a function of the temperature and frequency at zero-field and B = 1 KOe.

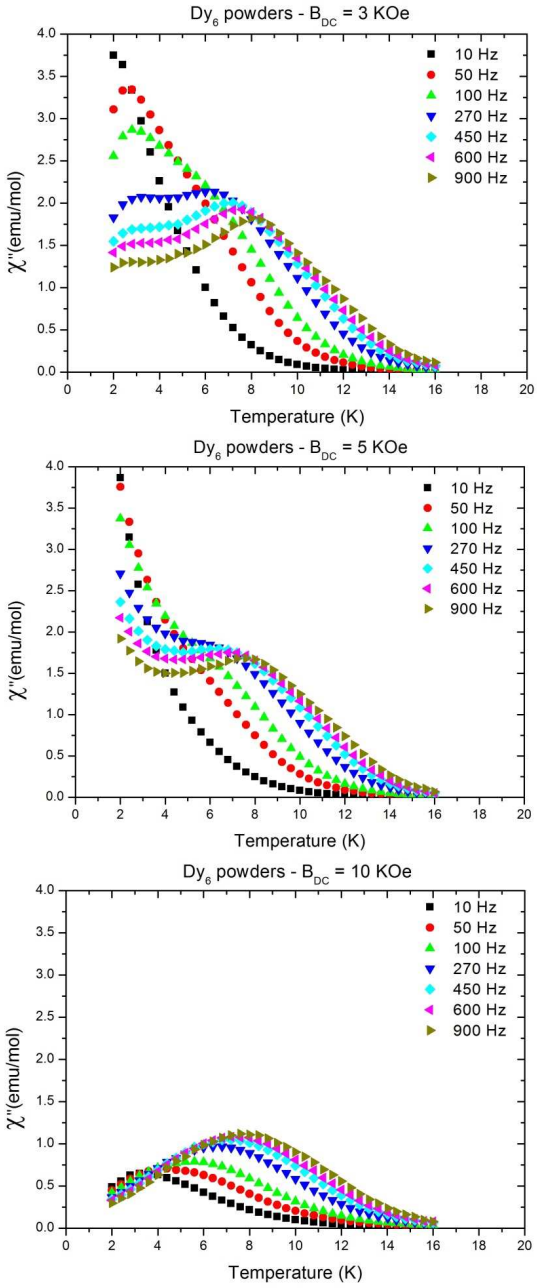

Figure 5.2.2: Immaginary part of susceptibility of Dy_6 as a function of the temperature and frequency at B = 3, 5 and 10 KOe.

The dynamics is characterized by more than one characteristic correlation time, whose values depend strongly on the applied field. From AC susceptibility data the position of the peaks at each frequency have been extract, in order to

obtain the temperature dependence of the spin-lattice relaxation rates ($1/\tau$). The experimental data have been fit with one or two lorentzian component and we extract the temperatures at which the AC-susceptibilty displays one or two peaks . The behaviour of AC susceptibility data of Dy_6 has been interpreted with the simplest conceivable model. We assume the presence of two different relaxation processes in the phonon-induced relaxation dynamics of the molecule:

- Direct process: It depends on the applied field and dominates at low temperatures causing one spin flip in the spin Ising configuration. It can be caused by phonon-induced modulations of dipolar interactions between Dy ions or by hyperfine interactions between electronic and nuclear spins (especially at zero field). Both phenomena can induce direct relaxation processes only if the molecule can not be modelled as an exact Ising system. Ab initio calculations [20] show that the g_x and g_y components of the spectroscopic splitting vector are not precisely zero, thus Dy_6 slightly deviates from the Ising behaviour. We have checked that DC magnetometry data are not sensible to this small deviations, thus confirming the Ising model interpretation. The Ising model is also the starting point for our relaxation dynamics model.

- Raman process: it is field indipendent and dominates at high temperature. It is a single-ion process, thus it is responsible for the flip of one single spin. The temperature dependence of a Raman process yields a power law:

$$\frac{1}{\tau} = AT^n$$

  From the comparison of our calculations with χ'' experimental data we have found: $A = 6 \cdot 10^{-6}$ Hz and n = 9.

The top-figure 5.2.3 show the calculated weights $A(\lambda_i, T, B)$ of the magnetization autocorrelation as a function of the inverse temperature. The y-axis is $log_{10}(\lambda_i)$, the color map shows the weights $A(\lambda_i, T, B)/\chi T$. When AC frequencies intersect the rates λ_i with significant weight, χ_{AC} displays a peak. The black and red scatter have been extract from AC-susceptibility data (see Figure 5.2.1 and Figure 5.2.2). The bottom-figure 5.2.3 shows the calculated immaginary part of susceptibility as a function of the temperature and frequency at B = 10 KOe, obtained by taking

into account the direct and Raman processes as described above. The position of the experimental peak and the temperature/field dependence in the χ'' are well reproduced.

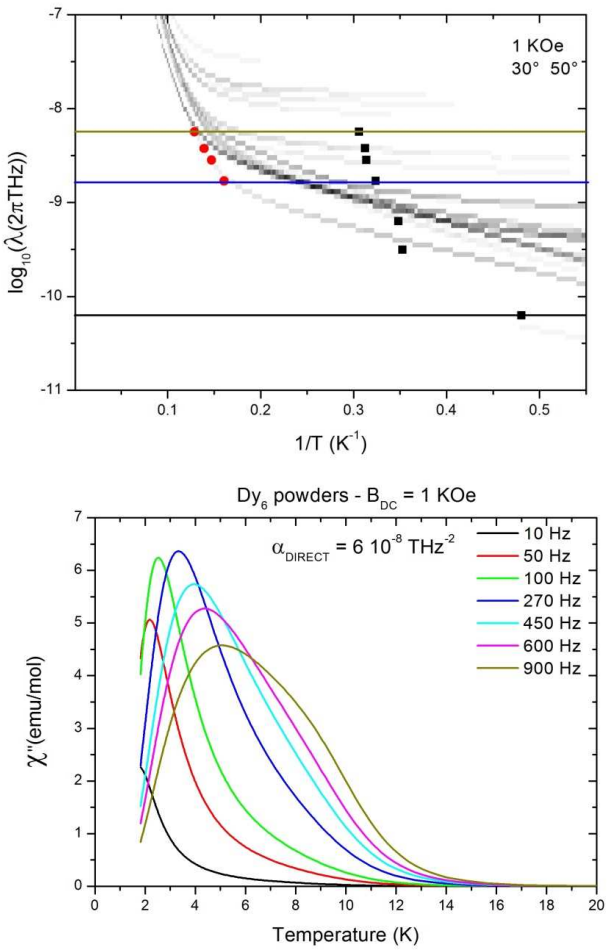

Figure 5.2.3: Top: Calculated weights of the magnetization autocorrelation for B=1 kOe. We have superimposed the temperatures at which the experimental AC-susceptibilty displays the broad peaks, one or two, whose centers are represented by the red and black symbols. Dark yellow, blue and black lines correspond to 900 Hz, 270Hz and 10 Hz respectively. Bottom: Calculated immaginary part of the susceptibility.

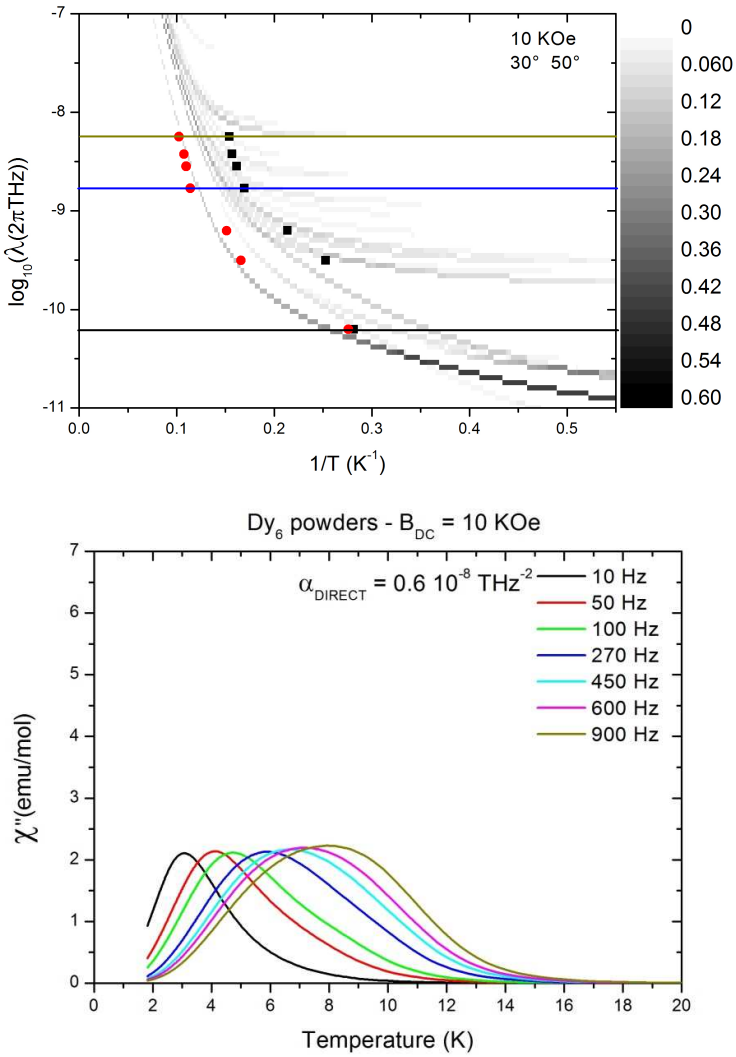

Figure 5.2.4: Top: Calculated weights of the magnetization autocorrelation for B=10 kOe. We have superimposed the temperatures at which the experimental AC-susceptibilty displays the broad peaks, one or two, whose centers are represented by the red and black symbols. Dark yellow, blue and black lines correspond to 900 Hz, 270Hz and 10 Hz respectively. Bottom: Calculated immaginary part of the susceptibility.

In order to study the dynamics of Dy_6 in a different time window a μSR LF-experiments as a function of the temperature have been carried out on the GPS spectrometer at the continuous muon source of the SμS facility of the Paul Scher-

rer Institute (PSI). The figure 5.2.5 show the time-dependent muon asymmetry as a function of the temperature.

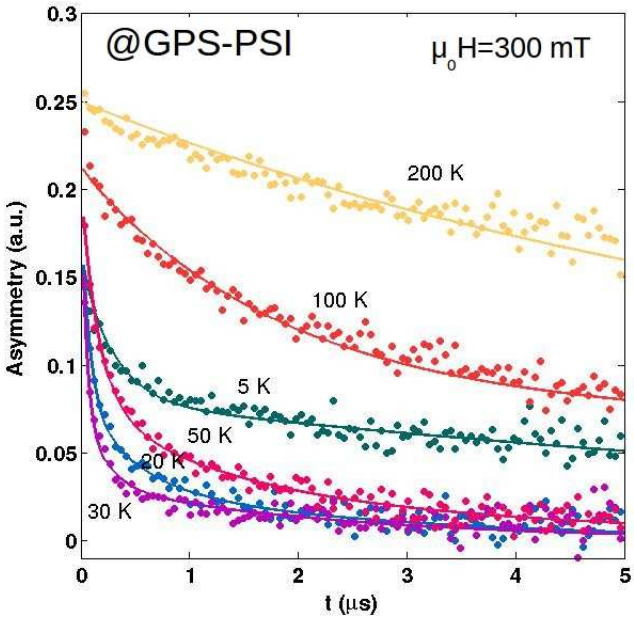

Figure 5.2.5: Time-dependent muon asymmetry as a function of the temperature for B=300 mT.

This behavior is typical of that previously observed in other MNM and it is due to the complex dynamic distribution of local fields within the sample[104, 105, 106].
The muon asymmetry is fitted by:

$$A(t) = a_s e^{-\lambda_s t} + a_I e^{-\lambda_I t} + G_{KL}(\lambda_f, t), \tag{5.2.1}$$

where $a_{s,I}$ is the slow and intermediate relaxing amplitude, $\lambda_{s,I}$ is the slow and intermediate relaxation rate λ and $G_{KL}$is the lorentzian Kubo-Toyabe function, due to a random array of static moments with a Lorentzian field distribution [107]. The slow component corresponds to muons away from the magnetic moment of molecule. The λ_{GK} is too fast and it was not possible to analyze it well. For this reason only the intermediate relaxation rate are reported as a function of the temperature for three different longitudinal field (see figure 5.2.6).

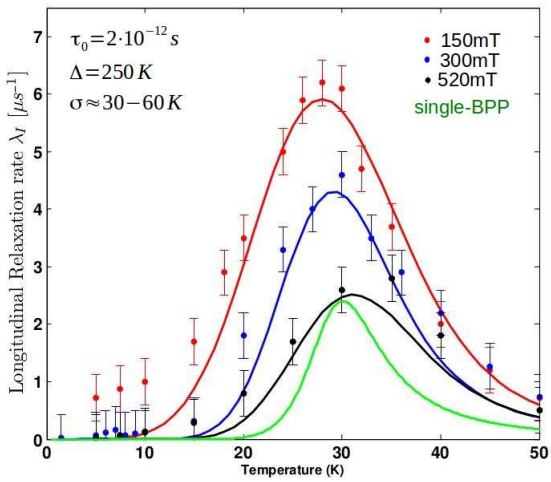

Figure 5.2.6: Longitudinal relaxation rate as a function of the temperature for three different magnetic fields. The data are fitted as described in the text. The green line represents the BPP-behaviour.

The data can not be fitted by a BPP model (green curve in figure 5.2.6), but they require a distribution of energy barriers. Thus λ_I can be fitted by:

$$\lambda_I = \frac{1}{T_1} = C \int_0^\infty \left(\frac{D(E)\tau(E)}{1+\omega_L^2\tau^2(E)} dE \right)$$

with a thermally activated correlation time given by:

$$\tau(E) = \tau_0 e^{\frac{E}{k_B T}}.$$

By assuming a a gaussian distribution of energy barriers we have:

$$D(E) = \frac{1}{\sqrt{2\pi}\sigma} e^{-\frac{(E-\Delta)^2}{2\sigma^2}}.$$

The results of the fit yield an average activation energy barrier around 250 K. It is worth to note that, according to the calculations reported in [20], this energy corresponds to the gap between the ground and an excited doublet of each Dy ion. This could suggest an Orbach process involving these high-energy states. However, the temperature of the peak in $\lambda(T)$ is in reasonable agreement with the model exploited for interpreting dynamical susceptibility data (see Fig 5.2.7),

which does not include these high-energy processes.

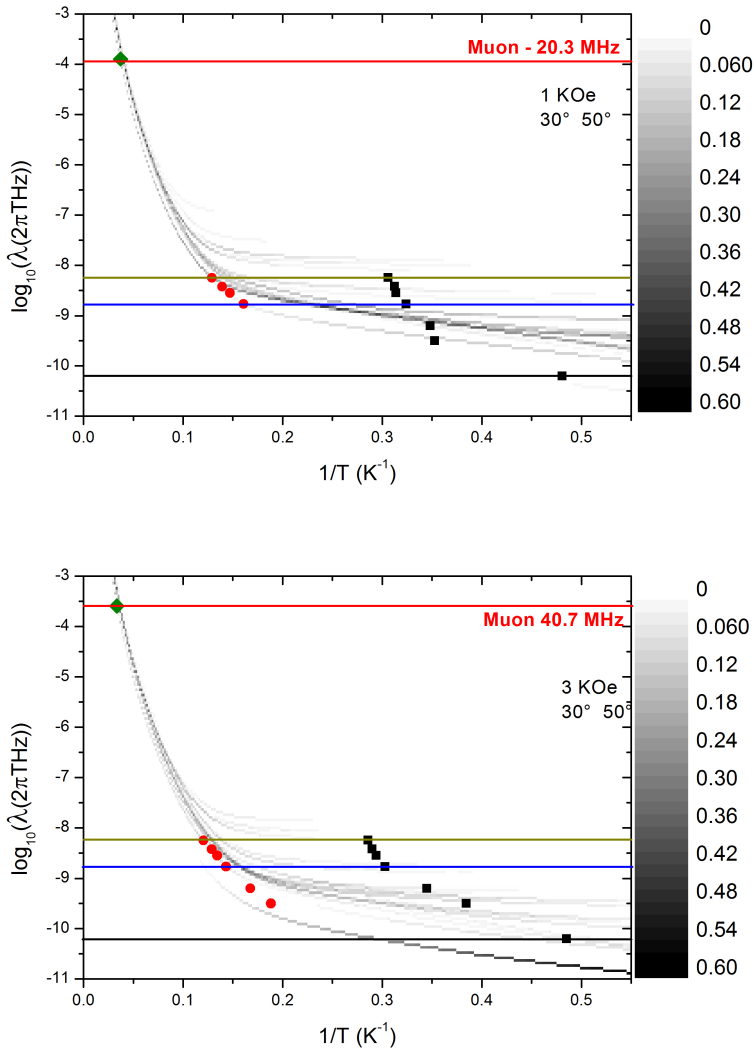

Figure 5.2.7: Calculated weights of the magnetization autocorrelation for B=1, 10 kOe. We have superimposed the temperatures at which the experimental AC-susceptibilty displays the broad peaks, one or two, whose centers are represented by the red and black symbols. Dark yellow, blue and black lines correspond to 900 Hz, 270Hz and 10 Hz respectively. The red line represents the frequency of the muon. When the frequency of muon (red line) intersect the rates λ_I with significant weight, λ_I displays a peak.

Figure 5.2.7 shows the calculated weights of the magnetization autocorrela-

tion as a function of the inverse temperature for B=100 and 300 mT. When the frequency of the muons (red line) intersect the rates λ_i with significant weight, the longitudinal relaxation rate displays a peak. In the temperature range where the peak of λ_I is observed, the dynamics is characterized by several rates characterized by appreciable weights and close in frequency. This fact explains why a broad single peak in the λ_I is observed in spite of the multi-time relaxation dynamics.

Future Prospects

The ^{1}H – NMR spectra were collected on powdered samples of Dy_6 at T= 1.35 K. Since the NMR line was very broad and shifted, the spectrum was constructed point by point by varying the frequency at a fixed external magnetic field. The spectra are reported in Figure 5.2.8 and are down shifted with respect the Larmor frequency.

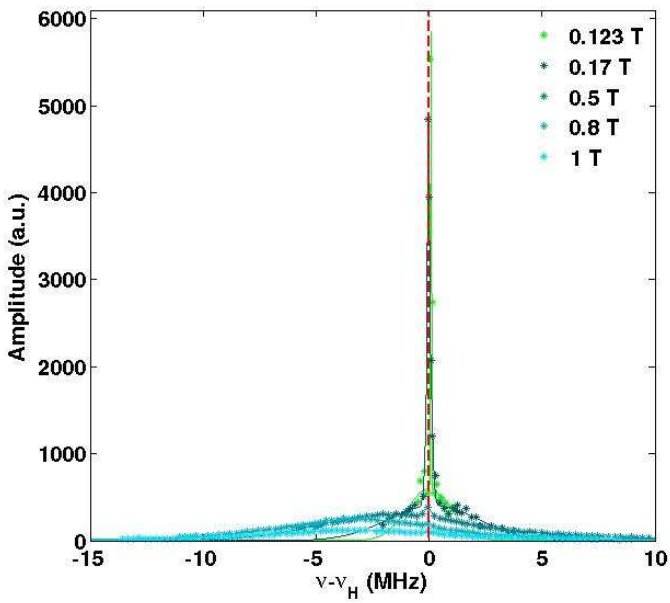

Figure 5.2.8: ^1H-NMR spectra at 1.35K shifted with respect the Larmor frequency, for different applied magnetic field.

The spectra can be interpreted taking into account two gaussian components: the first one is broader and shifted at high magnetic field while the second one

is narrower and centered at the Larmor frequency. The area under the spectrum represents the number of protons probed. The results of the fit of the spectra of Figure 5.2.8 are reported in Figure 5.2.9 for the first (broader) component. A strong shift of the absorption lines with respect to the Larmor Frequency of the proton is found at low fields where the system is non-magnetic (see blue circles in the top-panel of Figure 5.2.9). This suggests the presence of a staggered magnetization reflecting the effect of a toroidal moment. If it is true that the spectrum becomes very narrow preserving the area (and hence all protons feel a field equal to zero due to electron spins), the data may indicate the presence of tunneling of toroidal moment.

The red circles in the top-panel of Figure 5.2.9 show the FHWM of the NMR-line as a function of the external magnetic field, which decreases by lowering the magnetic field.

At low magnetic field, the amplitude of the second component increases (see figure 5.2.9).

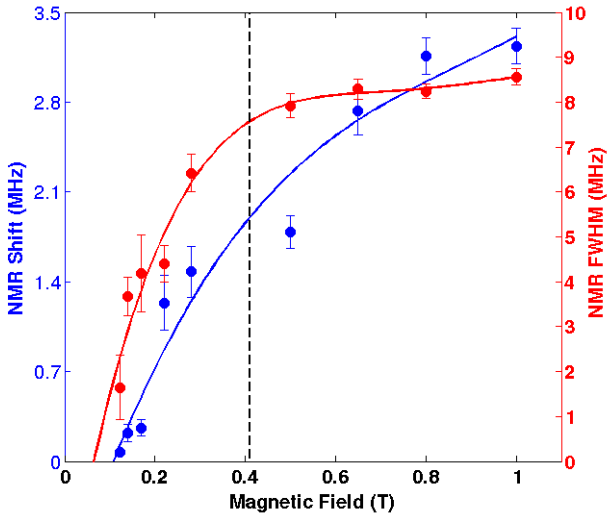

Figure 5.2.9: Shift of NMR line as a function of the external magnetic field (blue circles). The absolute value of the shift increases at high magnetic field reflecting the appareance of a magnetic ground state for $H > H_{LC}$. FHWM as a function of the external magnetic field (red circles). The blue and red line are a guide to the eye.

A shift of the Larmor frequency and an increasing of the line width due to a distribution of a static internal fields were detected above 0.5 T, indicative of a magnetic state of the Dy_6 induced by the external field.
Further theoretical investigation for the interpretation of the experimental data are still in progress.

Chapter 6

Conclusions

In this thesis the magnetic properties and relaxation dynamics of selected AF molecular nanomagnets have been investigated. The experimental study has been carried out by different techniques: NMR, μSR, AC and DC SQuID magnetometry. Through these techniques, the static and dynamic properties of these systems have been studied. Indeed, the nuclear spin-lattice relaxation rate ($1/T_1$) and the muon longitudinal field relaxation are sensitive to the fluctuations of the dipolar and hyperfine fields from the molecular spins. From the comparison of theoretical calculations with experimental data it is possible to extract the parameters of the Spin Hamiltonian and information on the relaxation dynamics.

In particular, we have studied the magnetic properties and relaxation dynamics of the first regular Cr_9 AF ring, which represents a prototype of practically degenerate-frustrated homometallic ring of half-integer spins. The energy spectrum of this kind of systems is characterized by a two-fold degeneracy of the low-energy total-spin multiplets. The relaxation of Cr_9 has been investigated by measuring the temperature and magnetic field dependence of the spin-lattice relaxation rate$1/T_1$ of ^1H nuclei. The experimental results have been interpreted by a microscopic model including magnetoelastic couplings and taking into account the wipeout effect. This model has allowed us to reproduce satisfactorily the experimental results and to study the phonon-induced decay of molecular magnetization. While magnetic relaxation of bipartite rings is well known, this is the first investigation of an odd-membered AF ring. We have found that in Cr_9 the

relaxation dynamics is characterized by a single Arrhenius time only at very low temperatures, whereas above 3 K several relevant relaxation rates emerge.
The magnetically-open AF rings, Cr_8Cd and Cr_8Zn, are model systems for the study of the microscopic magnetic behaviour of finite AF Heisenberg chains. In this type of systems the magnetic behaviour depends length and on the parity of the chain (odd or even). It is very important to know the local spin configuration, in order to be able to control and manipulate the magnetic state. By means of challenging ^{53}Cr-NMR spectroscopic measurements, we have found that the arrangment of the magnetic moments is non collinear (NC), in agreeement with recent polarized neutron diffraction results. FThe difficulty of ^{53}Cr-NMR measurements is due to the low natural abundance and the low sensitivity of the probe. By comparing the experimental results with the calculated ^{53}Cr-NMR frequencies it is possible to determine the only free parameter of the model, the contact term A. The result found agrees with what found in other rings. Due to Cr_8Cd symmetry properties, it is possible to indentify four pair of equivalent Cr^{3+} sites. It was also possible to attribute the signal to the corresponding pair of ^{53}Cr nuclei in the ring and we find that the signal observed can be totally ascribed to the two pairs of Cr at the edge of the chain. The quantitative experimental result confirms the theoretical predictions for the non-collinear spin arrangement in finite AF-coupled magnetic ions chains and the comparison between Cr_8Cd and Cr_7Cd shown how the parity of the chain and the boundary condition have an effect on the spin structure.
Finally, the study of the static and dynamic magnetic properties of Dy_6 has been performed by means of ^{1}H-NMR (further theoretical investigation for the interpretation of the experimental data are still in progress) and DC/AC magnetometry. The Dy_6 is a first rare-earth based ring that has been investigated and can be described by a non-collinear Ising model. The investigation of spin dynamics has been performed by AC-SQuID and μSR measurements. We found that the dynamics is characterized by more than one characteristic correlation time, whose values depend strongly on the applied field. The behaviour of AC susceptibility data of Dy_6 has been interpreted by considering two different relaxation processes in the phonon-induced relaxation dynamics of the molecule. The temperature dependent Longitudinal relaxation rate (λ) from μSR experiment displays a field-dependent

peak around 30 K, in reasonable agreement with the model for the relaxation dynamics used to interpret AC susceptibility results.

List of Publications

- T. Lancaster, S. R. Giblin, G. Allodi, S. Bordignon, M. Mazzani, R. De Renzi, P. G. Freeman, P. J. Baker, F. L. Pratt, P. Babkevich, S. J. Blundell, A. T. Boothroyd, J. S.Moller, and D. Prabhakaran "Stripe disorder and dynamics in the hole-doped antiferromagnetic insulator $La_{5/3}Sr_{1/3}CoO_4$" PHYSICAL REVIEW B 89, 020405(R) (2014)

- E. Garlatti, S. Bordignon, S. Carretta, G. Allodi, G. Amoretti, R. De Renzi, A. Lascialfari, Y. Furukawa, G. A. Timco, R. Woolfson, R. E. P. Winpenny, and P. Santini "Relaxation Dynamics in the frustrated Cr_9 antiferromagnetic ring probed by NMR" *In press* PRB

- Fatemeh Adelnia, Lorenzo Bordonali, Manuel Mariani, Sara Bordignon, Grigore Timco, Richard Winpenny, Ferdinando Borsa and Alessandro Lascialfari "Comparison of spin dynamics and magnetic properties in antiferromagnetic closed and open molecular Cr-based rings" J. Phys.: Condens. Matter 27 (2015) 506001

- Fatemeh Adelnia, Alessandro Chiesa, Sara Bordignon, Stefano Carretta, Alberto Ghirri, Andrea Candini, Christian Cervetti, Marco Evangelisti, Marco Affronte, Ilya Sheikin, Richard Winpenny, Grigore Timco, Ferdinando Borsa, Alessandro Lascialfari "Low temperature magnetic properties and spin dynamics in single crystals of Cr8Zn antiferromagnetic molecular rings" The Journal of Chemical Physics 143, 244321 (2015)

Publications under review

- R. C. Williams, F. Xiao,T. Lancaster, R. De Renzi,G. Allodi,S. Bordignon,P. G. Freeman,F. L. Pratt,S. R. Giblin,J. S. Moller,S. J. Blundell,A. T. Boothroyd, and D. Prabhakaran "Magnetic phase diagram of $La_{2-x}Sr_xCoO_4$ revised using muon-spin relaxation. " submitted to PRL

Publications in preparation

- Dy6 (2)
- Cr8Cd
- $SmFe_{1-x}Mn_xAs_{0.88}F_{0.12}$

Acknowledgments

Un ringraziamento particolare al prof. Allodi per avermi aiutato e per aver rimediato ai miei danni in laboratorio, concludo questi tre anni sapendo che avrei potuto imparare molto di più da lui. Ringrazio il prof. De Renzi che è sempre riuscito a rimettermi sulla strada giusta quando mi perdevo. Ringrazio il prof. Carretta che mi ha permesso di lavorare all'interno del progetto, per la sua pazienza nel spiegarmi le cose, la passione che ha per il suo lavoro e per come riesce a trasmetterla. Ringrazio infinitamente la dott.sa Garlatti per tutto l'aiuto che mi ha dato (decisamente non trascurabile). Ringrazio il prof. Amoretti, il prof. Santini e il prof.Lascialfari. Ringrazio i colleghi di Pavia F.Adelnia e il dott. Bordonali.
Ringrazio il dott. Lamura, ottimo insegnante e buon amico, conserverò fra i ricordi belli le notti insonni a PSI (e so che mi mancheranno) insieme a lui, al dott. Shiroka e dott. Sanna. Ringrazio i colleghi e compagni di sventura Giacomo M., Daniele M., Daniela D., Giovanna E., Serena L., Silvia B., Pietro B. Ringrazio Alessandro C. abbiamo iniziato insieme 8 anni fa e concluderemo questo ciclo di studi insieme.
Ringrazio F.Hajduk il mio insegnante di violino e compagno di squadra a calcetto.
Ringrazio la mia famiglia senza di loro tutto questo non ci sarebbe stato, in particolar modo mia madre e mio padre, le mie due fantastiche sorelle, i miei due fratelli e il mio fratello acquisito Nicola.
Ringrazio Mattia che mi ha sempre sopportato (soprattutto negli ultimi mesi) e sostenuto.
Vorrei infine ringraziare tutti quelli che hanno reso nel bene e nel male questi tre anni indimenticabili.

Bibliography

[1] Sessoli Villain Gatteschi D. *Molecular Nanomagnets*. 2004. 3, 4, 39, 71

[2] Stephen J. Blundell. Molecular magnets. *Contemp. Phys.*, 48(5):275–290, sep 2007. 3

[3] Jonathan R Friedman, M P Sarachik, and R Ziolo. Macroscopic Measurement of Resonant Magnetization Tunneling in High-Spin Molecules. *Phys. Rev. Lett.*, 76(20):3830–3833, 1996. 3

[4] Michael N Leuenberger and Daniel Loss. Quantum computing in molecular magnets. *Lett. to Nat.*, 410(April):789–793, 2001. 3, 6, 8

[5] M Affronte, F Troiani, a Ghirri, a Candini, M Evangelisti, V Corradini, S Carretta, P Santini, G Amoretti, F Tuna, G Timco, and R E P Winpenny. Single molecule magnets for quantum computation. *J. Phys. D. Appl. Phys.*, 40(10):2999–3004, 2007. 3

[6] F Troiani, a. Ghirri, M Affronte, S Carretta, P Santini, G Amoretti, S Piligkos, G Timco, and R Winpenny. Molecular Engineering of Antiferromagnetic Rings for Quantum Computation. *Phys. Rev. Lett.*, 94(20):207208, 2005. 3, 58

[7] Alberto Ghirri, Filippo Troiani and Marco Affronte. Quantum Computation with Molecular Nanomagnets: Achievements, Challenges, and New Trends. *Springer-Verlag Berlin Heidelb. 2014*, 119(2014):193–223, 2006. 3

[8] C. Sangregorio, T. Ohm, C. Paulsen, R. Sessoli, and D. Gatteschi. Quantum Tunneling of the Magnetization in an Iron Cluster Nanomagnet. *Phys. Rev. Lett.*, 78(24):4645–4648, 1997. 4, 6

[9] S. Takahashi, J. Van Tol, C. C. Beedle, D. N. Hendrickson, L. C. Brunel, and M. S. Sherwin. Coherent manipulation and decoherence of S=10 single-molecule magnets. *Phys. Rev. Lett.*, 102(8):1–4, 2009. 4

[10] Ian J Hewitt, Jinkui Tang, N T Madhu, Christopher E Anson, Yanhua Lan, Javier Luzon, Mael Etienne, Roberta Sessoli, and Annie K Powell. Coupling Dy3 triangles enhances their slow magnetic relaxation. *Angew. Chemie - Int. Ed.*, 49(36):6352–6356, 2010. 4

[11] O. Waldmann, S. Carretta, P. Santini, R. Koch, A. G. M. Jansen, G. Amoretti, R. Caciuffo, L. Zhao, and L. K. Thompson. Quantum Magneto-Oscillations in a Supramolecular Mn(II)-[3x3] Grid. *Phys. Rev. Lett.*, 92(9):096403, 2004. 4

[12] J Schnack and Marshall Luban. Rotational modes in molecular magnets with antiferromagnetic Heisenberg exchange. *Phys. Rev. B*, 63(1):14418, 2000. 4, 5

[13] O. Waldmann, T. C. Stamatatos, G. Christou, H. U. Güdel, I. Sheikin, and H. Mutka. Quantum phase interference and Néel-vector tunneling in antiferromagnetic molecular wheels. *Phys. Rev. Lett.*, 102(15):1–4, 2009. 5

[14] J Ummethum, J Nehrkorn, S Mukherjee, N B Ivanov, S Stuiber, Th Strässle, P L W Tregenna-Piggott, H Mutka, G Christou, O Waldmann, and J Schnack. Discrete antiferromagnetic spin-wave excitations in the giant ferric wheel Fe18. *Phys Rev B*, 86(10):104403, 2012. 5

[15] O Waldmann, T Guidi, S Carretta, C Mondelli, and A L Dearden. Elementary excitations in the cyclic molecular nanomagnet Cr8. *Phys. Rev. Lett.*, 91(23):237202, 2003. 5, 43

[16] Yuji Furukawa, Kazuki Kiuchi, Ken-ichi Kumagai, Yoshitami Ajiro, Yasuo Narumi, Masahiro Iwaki, Koichi Kindo, Alberto Bianchi, Stefano Carretta, Grigore Timco, and Richard Winpenny. Topological effects on the magnetic properties of closed and open ring-shaped Cr-based antiferromagnetic nanomagnets. *Phys. Rev. B*, 78(9):092402, sep 2008. 6, 9, 59

[17] T. Guidi, B. Gillon, S. a. Mason, E. Garlatti, S. Carretta, P. Santini, a. Stunault, R. Caciuffo, J. van Slageren, B. Klemke, a. Cousson, G. a. Timco, and R. E. P. Winpenny. Direct observation of finite size effects in chains of antiferromagnetically coupled spins. *Nat. Commun.*, 6(May):7061, 2015. 6, 58, 59, 64, 68

[18] L. Bordonali, E. Garlatti, C. M. Casadei, Y. Furukawa, A. Lascialfari, S. Carretta, F. Troiani, G. Timco, R. E. P. Winpenny, and F. Borsa. Magnetic properties and hyperfine interactions in Cr8, Cr7Cd, and Cr7Ni molecular rings from 19F-NMR. *J. Chem. Phys.*, 140(14):144306, 2014. 6, 59

[19] Hans Schmid. Some symmetry aspects of ferroics and single phase multiferroics. *J. Phys. Condens. Matter*, 20(43):434201, 2008. 6

[20] Liviu Ungur, Stuart K Langley, Thomas N Hooper, Boujemaa Moubaraki, Euan K Brechin, Keith S Murray, and Liviu F Chibotaru. Net Toroidal Magnetic Moment in the Ground State of a Dy6 Ring. pages 8–11, 2012. 6, 10, 70, 76, 80

[21] C. Schlegel, J. Van Slageren, M. Manoli, E. K. Brechin, and M. Dressel. Direct observation of quantum coherence in single-molecule magnets. *Phys. Rev. Lett.*, 101(OCTOBER):1–4, 2008. 6, 7

[22] Arzhang Ardavan, Olivier Rival, John J. L. Morton, Stephen J. Blundell, Alexei M. Tyryshkin, Grigore A. Timco, and Richard E. P. Winpenny. Will Spin-Relaxation Times in Molecular Magnets Permit Quantum Information Processing? *Phys. Rev. Lett.*, 98(5):057201, 2007. 6

[23] L. Thomas, F. Lionti, R. Ballou, D. Gatteschi, R. Sessoli, and B. Barbara. Macroscopic quantum tunnelling of magnetization in a single crystal of nanomagnets, 1996. 6

[24] L. Sorace, W. Wernsdorfer, C. Thirion, A.-L. Barra, M. Pacchioni, D. Mailly, and B. Barbara. Photon-assisted tunneling in a Fe8 single-molecule magnet. *Phys. Rev. B*, 68(22):220407, 2003. 6

[25] P. Santini, S. Carretta, G. Amoretti, T. Guidi, R. Caciuffo, A. Caneschi, D. Rovai, Y. Qiu, and J. R D Copley. Spin dynamics and tunneling of the Neel vector in the Fe10 magnetic wheel. *Phys. Rev. B - Condens. Matter Mater. Phys.*, 71:1–7, 2005. 6

[26] Filippo Troiani, Marco Affronte, Stefano Carretta, Paolo Santini, and Giuseppe Amoretti. Proposal for quantum gates in permanently coupled antiferromagnetic spin rings without need of local fields. *Phys. Rev. Lett.*, 94(May):1–4, 2005. 6, 7

[27] Grigore A Timco, Stefano Carretta, Filippo Troiani, Floriana Tuna, Robin J Pritchard, Christopher A Muryn, Eric J L McInnes, Alberto Ghirri, Andrea Candini, Paolo Santini, Giuseppe Amoretti, Marco Affronte, and Richard E P Winpenny. Engineering the coupling between molecular spin qubits by coordination chemistry. *Nat. Nanotechnol.*, 4(3):173–178, 2009. 7, 58

[28] Alessandro Chiesa, George F. S. Whitehead, Stefano Carretta, Laura Carthy, Grigore a. Timco, Simon J. Teat, Giuseppe Amoretti, Eva Pavarini, Richard E. P. Winpenny, and Paolo Santini. Molecular nanomagnets with switchable coupling for quantum simulation. *Sci. Rep.*, 4:7423, 2014. 7, 58

[29] E Micotti, Y Furukawa, K Kumagai, S Carretta, a. Lascialfari, F Borsa, G Timco, and R Winpenny. Local Spin Moment Distribution in Antiferromagnetic Molecular Rings Probed by NMR. *Phys. Rev. Lett.*, 97(26):267204, 2006. 7, 59, 65, 67

[30] C. Schlegel, J. van Slageren, G. Timco, R. Winpenny, and M. Dressel. Origin of superhyperfine interactions in the antiferromagnetic ring Cr7Ni. *Phys. Rev. B*, 83(13):5–7, 2011. 7

[31] Alberto Ghirri, Alessandro Chiesa, Stefano Carretta, Filippo Troiani, Johan van Tol, Stephen Hill, Inigo Vitorica-Yrezabal, Grigore A. Timco, Richard E. P. Winpenny, and Marco Affronte. Coherent Spin Dynamics in Molecular Cr8Zn Wheels. *J. Phys. Chem. Lett.*, 6(24):5062–5066, 2015. 7

[32] S. Carretta, a. Chiesa, F. Troiani, D. Gerace, G. Amoretti, and P. Santini. Quantum information processing with hybrid spin-photon qubit encoding. *Phys. Rev. Lett.*, 111(11):1–5, 2013. 7

[33] Svetlana Kyatskaya, J. R G Mascarós, Lapo Bogani, Frank Hennrich, Manfred Kappes, Wolfgang Wernsdorfer, and Mario Ruben. Anchoring of rare-earth-based single-molecule magnets on single-walled carbon nanotubes. *J. Am. Chem. Soc.*, 131(42):15143–15151, 2009. 7

[34] Lapo Bogani and Wolfgang Wernsdorfer. Molecular spintronics using single-molecule magnets. *Nat. Mater.*, 7(3):179–186, 2008. 7

[35] K. A. Van Hoogdalem and D. Loss. Ultrafast magnon transistor at room temperature. *Phys. Rev. B - Condens. Matter Mater. Phys.*, 88(2):024420(1–8), 2013. 7

[36] Institut Néel, Université Joseph Fourier, and Grenoble Cedex. Molecular nanomagnets : towards molecular spintronics Wolfgang Wernsdorfer. 7(x):497–522, 2010. 7

[37] E Garlatti, S Carretta, M Affronte, E C Sañudo, G Amoretti, and P Santini. Magnetic properties and relaxation dynamics of a frustrated Ni7 molecular nanomagnet. *J. Phys. Condens. Matter*, 24(10):104006, mar 2012. 7

[38] E. Garlatti, S. Carretta, J. Schnack, G. Amoretti, and P. Santini. Theoretical design of molecular nanomagnets for magnetic refrigeration. *Appl. Phys. Lett.*, 103(20):202410, 2013. 7

[39] R. Sessoli, D. Gatteschi, a. Caneschi, and M. a. Novak. Magnetic bistability in a metal-ion cluster. *Nature*, 365(6442):141–143, 1993. 7

[40] M Affronte, a. Ghirri, S Carretta, G Amoretti, S Piligkos, G a. Timco, and R E P Winpenny. Engineering molecular rings for magnetocaloric effect. *Appl. Phys. Lett.*, 84(18):3468, 2004. 7

[41] Amoretti G. *Formulazione Microscopica delle Interazioni Fondamentali nel Magnetismo*. 1990. 7

[42] B.Bleaney A.Abragam. *Electron Paramagnetic Resonance of Transition Ions*, volume 1. 1970. 7, 41

[43] A. Chiesa, S. Carretta, P. Santini, G. Amoretti, and E. Pavarini. Many-Body Models for Molecular Nanomagnets. *Phys. Rev. Lett.*, 110(15):157204, 2013. 8

[44] F Troiani, V Bellini, and M Affronte. Decoherence induced by hyperfine interactions with nuclear spins in antiferromagnetic molecular rings. *Phys. Rev. B*, 77(5):54428, feb 2008. 8

[45] Leonardo Spanu and Alberto Parola. Lattice effects on the spin dynamics in antiferromagnetic molecular rings. *Phys. Rev. B*, 72(21):212402, 2005. 8

[46] P. Santini, S. Carretta, E. Liviotti, G. Amoretti, P. Carretta, M. Filibian, a. Lascialfari, and E. Micotti. NMR as a Probe of the Relaxation of the Magnetization in Magnetic Molecules. *Phys. Rev. Lett.*, 94(7):077203, feb 2005. 8, 9, 48

[47] H. Amiri, a. Lascialfari, Y. Furukawa, F. Borsa, G. a. Timco, and R. E. P. Winpenny. Comparison of the magnetic properties and the spin dynamics in heterometallic antiferromagnetic molecular rings. *Phys. Rev. B*, 82(14):144421, oct 2010. 9

[48] E Micotti, a. Lascialfari, F Borsa, M Julien, C Berthier, M Horvatić, J van Slageren, and D Gatteschi. Spin dynamics at the level crossing in the molecular antiferromagnetic ring [Cr8F8Piv16] from proton NMR. *Phys. Rev. B*, 72(2):20405, 2005. 9, 43, 48, 54

[49] a. Bianchi, S. Carretta, P. Santini, G. Amoretti, T. Guidi, Y. Qiu, J. R D Copley, G. Timco, C. Muryn, and R. E P Winpenny. Rotational bands in open antiferromagnetic rings: A neutron spectroscopy study of Cr8 Zn. *Phys. Rev. B - Condens. Matter Mater. Phys.*, 79(14):1–6, 2009. 9

[50] Fatemeh Adelnia, Alessandro Chiesa, Sara Bordignon, Stefano Carretta, Alberto Ghirri, Christian Cervetti, Marco Evangelisti, Marco Affronte, Ilya Sheikin, Grigore Timco, Ferdinando Borsa, and Alessandro Lascialfari. Low temperature magnetic properties and spin dynamics in single crystals of Cr 8 Zn antiferromagnetic molecular rings. *Prog.*, pages 1–19. 9, 50, 73

[51] Fatemeh Adelnia, Lorenzo Bordonali, Manuel Mariani, Sara Bordignon, Grigore Timco, Richard Winpenny, Ferdinando Borsa, and Alessandro Lascialfari. Comparison of spin dynamics and magnetic properties in antiferromagnetic closed and open molecular Cr-based rings. *J. Phys. Condens. Matter*, 27(50):506001, 2015. 9, 21, 56, 57

[52] I J Vitorica R. J. Woolfson, G. A. Timco, A. Chiesa, Yrezabal, F. Tuna, T. Guidi, P. Santini, S. Carretta, and Manuscript submitted Angew. Chem. and R. E. Winpenny. Cr9. 9, 44

[53] Grigore A Timco, Andrei S Batsanov, Finn K Larsen, Christopher A Muryn, Jacob Overgaard, Simon J Teat, and Richard E P Winpenny. Influencing the nuclearity and constitution of heterometallic rings via templates. *Chem. Commun. (Camb).*, (29):3649–51, 2005. 10, 58

[54] Stuart K Langley, Boujemaa Moubaraki, Craig M Forsyth, Ian a Gass, and Keith S Murray. Structure and magnetism of new lanthanide 6-wheel compounds utilizing triethanolamine as a stabilizing ligand. *Dalt. Trans.*, 39(7):1705–1708, 2010. 10, 69

[55] Freeman. Hyperfine Interactions in Magnetic Materials Magnetism, 1967. 17

[56] AG Redfield. On the theory of relaxation processes. *IBM J. Res. Dev.*, (January), 1957. 17, 48

[57] R Wangsness and F Bloch. The Dynamical Theory of Nuclear Induction. *Phys. Rev.*, 89(4):728–739, 1953. 17

[58] Slichter. *Principles_of_magnetic_resonance*. 1989. 18, 48

[59] Tôru Moriya. Nuclear Magnetic Relaxation near the Curie Temperature. *Prog. Theor. Phys.*, 28(2):371–400, 1962. 18

[60] E Garlatti, S Carretta, P Santini, G Amoretti, M Mariani, A. Lascialfari, S Sanna, K Mason, J Chang, P Tasker, and E K Brechin. Relaxation dynamics in a Fe7 nanomagnet. *Phys. Rev. B*, 87(5):54409, feb 2013. 19, 22, 45, 49, 54

[61] M. Belesi, a. Lascialfari, D. Procissi, Z. Jang, and F. Borsa. Proton NMR wipeout effect due to slow fluctuations of the magnetization in single molecule magnets. *Phys. Rev. B*, 72(1):014440, jul 2005. 21

[62] A.Abragam. The principles of nuclear magnetism. 21

[63] M. Belesi, a. Lascialfari, D. Procissi, Z. Jang, and F. Borsa. Proton NMR wipeout effect due to slow fluctuations of the magnetization in single molecule magnets. *Phys. Rev. B*, 72(1):014440, jul 2005. 21, 50

[64] G Allodi, a. Banderini, R De Renzi, and C Vignali. HyReSpect: A broadband fast-averaging spectrometer for nuclear magnetic resonance of magnetic materials. *Rev. Sci. Instrum.*, 76(8):1–7, 2005. 23, 24, 47

[65] S. J. Blundell. Spin-polarized muons in condensed matter physics. *Contemp. Phys.*, 40(3):175–192, 1999. 28

[66] Pietro Carretta and Alessandro Lascialfari. *NMR-MRI, muSR and mossbauer spectroscopies in molecular magnets*. 2007. 28, 57

[67] A Schenck. Muon spin rotation spectroscopy: principles and applications in solid state physics, 1985. 28, 30

[68] Pierre Dalmas de Reotier Alain Yaouanc. Muon Spin Rotation,Relaxation and Resonance, 2011. 28

[69] R Kubo. A stochastic theory of spin relaxation. *Hyperfine Interact.*, 8:731–738, 1981. 34

[70] Jun-liang Liu, Kang Yuan, J.-D. Leng, Liviu Ungur, Wolfgang Wernsdorfer, Fu-sheng Guo, Liviu F Chibotaru, and M-L Tong. A Six-Coordinate Ytterbium Complex Exhibiting Easy-Plane Anisotropy and Field-Induced Single-Ion Magnet Behavior. *Inorg. Chem.*, page 120716102957002, 2012. 38

[71] Katie R. Meihaus, Jeffrey D. Rinehart and Jeffrey R. Long. "Dilution-Induced Slow Magnetic Relaxation and Anomalous Hysteresis in Trigonal Prismatic Dysprosium(III) and Uranium(III) Complexes". *Inorg. Chem.*, 50:8484–8489, 2011. 38

[72] A.Urtizberea Silvia Gomez Coca. Origin of slow magnetic relaxation in Kramers ions with non-uniaxial anisotropy. *Nat. Commun.*, 2014. 38

[73] M Balanda. AC susceptibility studies of phase transitions and magnetic relaxation: Conventional, molecular and low-dimensional magnets. *Acta Phys. Pol. A*, 124(6):964–976, 2013. 38

[74] H. B. G. Casimir and F. K. Du Pre. Note on the thermodynamic interpretation of paramagnetic relaxation phenomena. *Physica*, 5(6):507–511, 1938. 39

[75] Jinkui Tang and Peng Zhang. *Lanthanide Single Molecule Magnets*. Springer, 2015. 41, 42

[76] S Carretta, J van Slageren, T Guidi, E Liviotti, C Mondelli, D Rovai, a. Cornia, a. Dearden, F Carsughi, M Affronte, C Frost, R Winpenny, D Gatteschi, G Amoretti, and R Caciuffo. Microscopic spin Hamiltonian of a Cr8 antiferromagnetic ring from inelastic neutron scattering. *Phys. Rev. B*, 67(9):2–9, 2003. 43

[77] Stephen Hill, Saiti Datta, Junjie Liu, Ross Inglis, Constantinos J. Milios, Patrick L. Feng, John J. Henderson, Enrique del Barco, Euan K. Brechin, and David N. Hendrickson. Magnetic quantum tunneling: insights from simple molecule-based magnets. *Dalt. Trans.*, 39(20):4693, 2010. 43

[78] Joris van Slageren Stergios Piligkos Neese and Frank. Magnetic circular dichroism spectroscopy on the Cr8 antiferromagnetic ring. *Dalt. Trans.*, 39(20):4999–5004, 2010. 43

[79] Joris Van Slageren, Roberta Sessoli, Dante Gatteschi, Andrew A Smith, Madeleine Helliwell, Richard E P Winpenny, Andrea Cornia, Anne-laure Barra, Aloysius G M Jansen, Eva Rentschler, and Grigore A Timco. Magnetic Anisotropy of the Antiferromagnetic Ring [Cr8 F8 Piv16]. *Chem.Eur.J*, pages 277–285, 2002. 43

[80] M Affronte, T Guidi, R Caciuffo, S Carretta, G Amoretti, J Hinderer, I Sheikin, a. Jansen, a. Smith, R Winpenny, J van Slageren, and D Gatteschi. Mixing of magnetic states in a Cr8 molecular ring. *Phys. Rev. B*, 68(10):104403, 2003. 43

[81] Finn K Larsen, Eric J L McInnes, Hassane El Mkami, Jacob Overgaard, Stergios Piligkos, Gopalan Rajaraman, Eva Rentschler, Andrew a. Smith, Graham M Smith, Val Boote, Martin Jennings, Grigore A Timco, and Richard E P Winpenny. Synthesis and characterization of heterometallic {Cr7M} wheels. *Angew. Chemie - Int. Ed.*, 42(1):101–105, 2003. 43

[82] Olivier Kahn. Competing spin interactions and degenerate frustration for discrete molecular species. *Chem. Phys. Lett.*, 265, 1997. 43

[83] Yuji Furukawa, Kazuki Kiuchi, Ken-ichi Kumagai, Yoshitami Ajiro, Yasuo Narumi, Masahiro Iwaki, Koichi Kindo, Alberto Bianchi, Stefano Carretta, Paolo Santini, Ferdinando Borsa, Grigore Timco, and Richard Winpenny. Evidence of spin singlet ground state in the frustrated antiferromagnetic ring Cr8Ni. *Phys. Rev. B*, 79(13):134416, apr 2009. 43

[84] Olivier Cador, Dante Gatteschi, Roberta Sessoli, Finn K. Larsen, Jacob Overgaard, Anne-Laure Barra, Simon J. Teat, Grigore a. Timco, and Richard E. P. Winpenny. The Magnetic Möbius Strip: Synthesis, Structure, and Magnetic Studies of Odd-Numbered Antiferromagnetically Coupled Wheels. *Angew. Chem.*, 116(39):5308–5312, 2004. 43

[85] Grzegorz Kamieniarz, Wojciech Florek and Michal Antkowiak. Universal sequence of ground states validating the classification of frustration in antiferromagnetic rings with a single bond defect. *Phys. Rev. B 92, 140411(R)*, 2015. 43

[86] Antkowiak Kozlowski. Detection of ground states in frustrated molecular rings by in-field local magnetization profiles. *Phys. Rev. B*, 87(18):184430, 2013. 44

[87] E Garlatti, S Carretta, M Affronte, E C Sanudo, G Amoretti, and P Santini. Magnetic properties and relaxation dynamics of a frustrated Ni7 molecular nanomagnet. *J. Phys. Condens. Matter*, 24(10):104006/1—-104006/9, 2012. 45, 54

[88] S Baek, M Luban, a. Lascialfari, E Micotti, Y Furukawa, F Borsa, J van Slageren, and a. Cornia. Scaling behavior of the proton spin-lattice relaxation rate in antiferromagnetic molecular rings. *Phys. Rev. B*, 70(13):134434, 2004. 48

[89] a. Bianchi, S. Carretta, P. Santini, G. Amoretti, J. Lago, M. Corti, A. Lascialfari, P. Arosio, G. Timco, and R. E. P. Winpenny. Phonon-induced relaxation in the Cr7Ni magnetic molecule probed by NMR. *Phys. Rev. B*, 82(13):134403, oct 2010. 49

[90] E Garlatti, S Bordignon, S Carretta, G Allodi, G Amoretti, R De Renzi, Y Furukawa, G A Timco, R Woolfson, R E P Winpenny, and P Santini. Relaxation Dynamics in the frustrated Cr 9 antiferromagnetic ring probed by NMR. *Manuscr. Prog.*, 2015. 52, 73

[91] Michael L Baker, Tatiana Guidi, Stefano Carretta, Jacques Ollivier, Hannu Mutka, Hans U Güdel, Grigore a. Timco, Eric J L McInnes, Giuseppe Amoretti, Richard E P Winpenny, and Paolo Santini. Spin dynamics of molecular nanomagnets unravelled at atomic scale by four-dimensional inelastic neutron scattering. *Nat. Phys.*, 8(12):906–911, 2012. 55

[92] Ioannis Rousochatzakis, Andreas Läuchli, Ferdinando Borsa, and Marshall Luban. Theory of severe slowdown in the relaxation of rings and clusters with antiferromagnetic interactions. *Phys. Rev. B*, 79(6):2–6, 2009. 57

[93] a. Ghirri, a. Candini, M Evangelisti, M Affronte, S Carretta, P Santini, G Amoretti, R Davies, G Timco, and R Winpenny. Elementary excitations in antiferromagnetic Heisenberg spin segments. *Phys. Rev. B*, 76(21):214405, 2007. 58

[94] a. Franchini, V Bortolani, and R Wallis. Interaction of an external impurity with the surface intrinsic mode in a Heisenberg chain. *Phys. Rev. B*, 73(5):54412, 2006. 58

[95] a. Machens, N Konstantinidis, O Waldmann, I Schneider, and S Eggert. Even-odd effect in short antiferromagnetic Heisenberg chains. *Phys. Rev. B*, 87(14):144409, 2013. 58

[96] L Bogani, a. Caneschi, M Fedi, D Gatteschi, M Massi, M a. Novak, M G Pini, a. Rettori, R Sessoli, and a. Vindigni. Finite-size effects in single chain magnets: An experimental and theoretical study. *Phys. Rev. Lett.*, 92(20):1–4, 2004. 58

[97] C F Hirjibehedin, C P Lutz, and A J Heinrich. Spin Coupling in Engineered Atomic Structures. *Science (80-.).*, 312(5776):1021–1024, 2006. 58

[98] Khajetoorians. Current-Driven Spin Dynamics of Artificially Constructed Quantum Magnets. *Science (80-.).*, 339(January):55, 2013. 58

[99] Samir Lounis, Peter H. Dederichs, and Stefan Blügel. Magnetism of nanowires driven by novel even-odd effects. *Phys. Rev. Lett.*, 101(10):1–4, 2008. 59

[100] C M Casadei, L Bordonali, Y Furukawa, F Borsa, E Garlatti, a Lascialfari, S Carretta, S Sanna, G Timco, and R Winpenny. Local spin density in the Cr7Ni antiferromagnetic molecular ring and 53Cr-NMR. *J. Phys. Condens. Matter*, 24(40):406002, oct 2012. 59, 65

[101] Alessandro Soncini and Liviu F. Chibotaru. Toroidal magnetic states in molecular wheels: Interplay between isotropic exchange interactions and local magnetic anisotropy. *Phys. Rev. B - Condens. Matter Mater. Phys.*, 77(22):1–4, 2008. 70

[102] Javier Luzon, Kevin Bernot, Ian Hewitt, Christopher Anson, Annie Powell, and Roberta Sessoli. Spin Chirality in a Molecular Dysprosium Triangle: The Archetype of the Non-collinear Ising Model. *Phys. Rev. Lett.*, 100(24):247205, jun 2008. 70

[103] Liviu F. Chibotaru, Liviu Ungur, and Alessandro Soncini. The Origin of Nonmagnetic Kramers Doublets in the Ground State of Dysprosium Triangles Evidence for a Toroidal Magnetic Moment. *Angew. Chemie Int. Ed.*, 47(22):4126–4129, 2008. 70

[104] Zaher Salman, Amit Keren, Philippe Mendels, Valerie Marvaud, Ariane Scuiller, Michel Verdaguer, James S. Lord, and Chris Baines. Dynamics at T-0 in half-integer isotropic high-spin molecules. *Phys. Rev. B*, 65(13):132403, 2002. 79

[105] Amit Keren, Oren Shafir, Efrat Shimshoni, V Marvaud, Anne Bachschmidt, and J Long. Experimental estimates of dephasing time in molecular magnets. *Phys Rev Lett*, 98(25):257204, 2007. 79

[106] S J Blundell, F L Pratt, I M Marshall, C A Steer, and W Hayes. Muon study of molecular magnets , spin crossover and magnetic nanodiscs. 134:1–6, 2001. 79

[107] R. S. Hayano, Y. J. Uemura, J. Imazato, N. Nishida, T. Yamazaki, and R. Kubo. Zero-and low-field spin relaxation studied by positive muons. *Phys. Rev. B*, 20(3):850–859, 1979. 79